THERMAL CONTROL OF NANOPHOTONIC STRUCTURES: TOWARDS LOW POWER OPTICAL INTERCONNECTS AND ENERGY APPLICATIONS

A Dissertation

Presented to the Faculty of the Graduate School

of Cornell University

in Partial Fulfillment of the Requirements for the Degree of

Doctor of Philosophy

by

Biswajeet Guha

August 2014

© 2014 Biswajeet Guha
ALL RIGHTS RESERVED

THERMAL CONTROL OF NANOPHOTONIC STRUCTURES: TOWARDS LOW POWER OPTICAL INTERCONNECTS AND ENERGY APPLICATIONS

Biswajeet Guha, Ph.D.

Cornell University 2014

This thesis explores the interplay between temperature and nanophotonics. In the beginning of the thesis, we address the problem of thermal stabilization of silicon photonic devices, which is a major obstacle in low power integration of on-chip optical interconnects. We demonstrate different schemes, at architecture and device levels, to mitigate thermal sensitivity in optical devices. Using one of the schemes, we demonstrate a ring resonator based electro–optic modulator working over 40 degrees. All the athermal schemes are passive and CMOS–compatible, making them more attractive over active feedback based power–hungry techniques.

The latter part of the thesis explores photon–based radiative heat transfer processes. Conventional blackbody radiation is much weaker than solid–state phonon based heat transfer, but its spectrum can be tailored easily as opposed to broadband nature of phonons. Near–field thermal radiation provides a way to overcome the traditional blackbody limit by increasing radiative density of states. We use this phenomenon to demonstrate strong near-field cooling of a thermally isolated membrane through evanescent coupling with a tip. Finally we demonstrate thermal rectification by using temperature dependent spectral properties in a radiative channel.

BIOGRAPHICAL SKETCH

Biswajeet Guha was born in Calcutta, India in 1985. He did most of his schooling in Calcutta, before moving to neighboring town of Kharagpur for undergraduate studies. He received B.Tech in Electronics & Electrical Communication Engineering from Indian Institute of Technology, Kharagpur in 2008. He spent the summer of 2007 working at Fraunhofer IISB in Erlangen, Germany and later backpacking across Europe. In 2008, he moved to Ithaca, N.Y. for doctoral studies at Cornell University. In December 2008, he joined Prof. Michal Lipson's group and fell in love with everything "nano". He briefly interned at Silicon Photonics group at Intel, Santa Clara from March to August 2012 and was a recipient of the Intel Ph.D Fellowship award for 2013–2014. He hopes to continue exploring the nano world in future.

To Linda, for making my stay in Ithaca unforgettable

To my parents, for always encouraging me

To Michal, for showing me how to dream & explore

ACKNOWLEDGEMENTS

When I arrived at Cornell in 2008, I had never worked in optics before except some occasional projects in undergraduate classes. My expertise in nanofabrication was limited to a semiconductor process technology class I took in my final year at IIT. When I applied for grad school in USA, it was a tough choice between Cornell and few other schools. After 6 years with Michal, countless nights at CNF and a lifetime with Linda, I can truly say it couldn't have been better.

My advisor Michal Lipson deserves the biggest credit for my development as a researcher. I cannot overstate how much she has influenced me through her constant support, encouragement, letting us dream and showing us how to achieve them. She is always willing to tackle difficult problems, with patience to deal with the failures that come along the way. She has worked incredibly hard over the years to build this nanophotonics group from scratch. I never needed to worry about buying something for my project, or having to repeat an e-beam step in the cleanroom. Looking around in the department and other schools, I feel fortunate that my PhD was a smooth ride where I could focus on my work, without worrying about funding or infrastructure. She has managed to create this atmosphere, not just for me but for every student in the group, through her amazing work ethic and tireless traveling. I never really enjoyed giving presentations when I started my PhD. And I've come a long way since then. The "Michal style" of presentation – talking about the big picture and emphasizing the main points at the beginning, will stick with me for the rest of my career. Michal always told us to dream big but never work on something that you don't believe in. That is probably the biggest thing I've learned in grad school, something that is outside the purview of this thesis but something I will

strive for the rest of my life. Thank you Michal, it's been an honor.

I would also like to thank my minor committee members Prof. Alex Gaeta and Prof. Sunil Bhave. Their breadth of knowledge and pleasant disposition made them a pleasure to work with. They often pointed me towards right direction during our interactions. The classes I took with Prof. Farhan Rana were extremely beneficial in my understanding of light–matter interaction. I would like to thank Prof. Shanhui Fan and his student, Clayton and Linxiao at Stanford University. His scientific knowledge and ability to generate new ideas is astounding, something for me to aspire to.

One of the remarkable things about Michal is her ability to inspire and fill the group with a wonderful bunch of people. Over the years, I've has the pleasure to work alongside several talented grad students and postdocs. Gustavo Wiederhecker taught me the ropes of COMSOL simulations and the importance of good graphics. Sasi Manipatruni always amazed me with his breadth of knowledge and ability to explore new areas. Sasha Gondarenko introduced me to the world of CNF and made my first chips on the old VB6 e–beam. Kyle Preston, Lucas Gabrielli and Hugo Lira were fun co–workers to have around. Nick Sherwood was the de–facto social chair of the group, esp. with his year end Puerto Rican Thanksgiving parties. Jaime Cardenas' knowledge of nanofabrication is immense, and he can always keep the crowd going. Bernardo Kyotoku was a very good friend, who could also program the hell out of everything. I still remember he managed to automate his entire setup and could move fibers and take data from the office (I later did the same during my internship). I'm sure he tried to make an app out of it. Of late, I've really enjoyed my friendship and collaboration with Raphael St–Gelais. I'm confident he will take the work on near–field heat transfer to new heights ... or smaller gaps. Carl Poitras has been

the bedrock of nanophotonics group, helping us all in many different ways. I cannot imaging the group with you Carl. To the newer kids in the group, I wish you all the best and look forward to your next brilliant works – Kevin Luke, Austin Griffith, Mian Zhang, Shreyas Shah, Avik Dutt, Danny Lee, Aseema Mohanty, Lawrence Tzuang, Moshe Zadka, Chris Phare and Romy Fain. Outside our group, Rajeev Dokania and Shriram Shivaraman have been great people to go to for advice. Finally big thanks to Kim Cotton for keeping the group's affairs in order.

I've been fortunate to have a good group of friends in Ithaca, which made life outside the lab that much more pleasurable. I shared many a cups of coffee and beer with Leifur, Mathav and Sarabjeet. Ithaca will always remain a special place since I met my fiancee, Linda here. She makes sure there is never a dull moment in our lives. I would like to thank Gimme for making the best coffee in town and providing an awesome workspace, where bulk of this thesis was written. Finally I would like to thank my parents for always encouraging me to go and do what I want.

Last but not the least I would like to thank the staff at CNF and CCMR for maintaining the best equipments and making my life easy. This work made use of the Cornell Center for Materials Research Shared Facilities which are supported through the NSF MRSEC program (DMR-1120296). This work was performed in part at the Cornell NanoScale Facility, a member of the National Nanotechnology Infrastructure Network, which is supported by the National Science Foundation (Grant ECCS-0335765). The work Athermal resonators was partly supported by NSF Grant 1002060 on "Temperature Insensitive Silicon Photonics" and NSF Grant 1143893 on "EAGER: Overcoming Thermal Sensitivity of CMOS-Compatible Nanophotonic Devices in Future Microprocessor

Designs". Part of the work on thermal radiation is sponsored by DARPA award FA8650-14-1-7406 on "Thermal Diodes" and U.S.Air Force (AFOSR) program FA9550-09-1-0704 on Robust and Complex on-chip Nanophotonics. I would like to thank my mentors at Intel Photonics Lab – Juthika Basak, Jung Park and Ling Liao – for their support during my internship. Final year of my PhD was sponsored by Intel PhD Fellowship.

TABLE OF CONTENTS

LIST OF FIGURES

CHAPTER 1

TEMPERATURE SENSITIVITY OF SILICON PHOTONIC DEVICES

1.1 Si photonics for next generation optical interconnects

Transistors and lasers were undoubtedly the two most important inventions of the 20^{th} century, which heralded breakthroughs in computing, medicine and several other aspects of our life. The computing industry has seen tremendous progress over the last few decades, as transistor dimensions have shrunk at an exponential rate from few hundred microns in the 1970s to few nanometers in 2014. The semiconductor industry has traditionally been driven by Moore's Law which incentivizes making computing elements smaller, faster and cheaper. This downscaling of feature size also results in tighter packing of wires that connect different elements on a processor. As a result, the parasitic resistance and capacitance of these wires, which were largely ignored in the early days of scaling, are becoming more severe now. The delay in transmitting information is now comparable to the computation delay itself a problem referred to as the interconnection bottleneck. Expansion of internet, wireless communication and online social networking has lead to generation of huge amounts of data that needs to be transported. Modern day datacenters need to support this by scaling their data transfer bandwidth at every level – server to server, rack–to–rack and board–to–board.

Optics offers a potential solution to overcome the bandwidth problem since photons are fundamentally better for transmitting information. Unlike electrons, photons do not interact with each other, so there are no parasitic effects. Optics has traditionally been used for long distance communication. Fiber op-

tics forms the backbone of modern day Internet, connecting together different cities and continents. The primary reason is that glass fibers can carry optical signals over hundreds of kilometers with relatively low loss, eliminating the need for frequent repeaters and equalizers. Optical links are now slowly being used at smaller distance scales. Fiber-to-home technology is becoming more popular. Optical interconnects also forms the backbone in datacenters and cloud computing, connecting various racks together. Metal based interconnects have traditionally been used at smaller distance scales like, board-to-board, chip-to-chip and within-chip communication. But optics interconnects are steadily scaling down as data rates are increasing. There is increasing interest in the computing industry to shift from copper to photonic interconnects for information transfer [1, 2].

The biggest impediment in scaling optical communication down to distances has been the cost of implementation. Optical elements have traditionally been made from exotic materials like GaAs, InP, $LiNbO_3$ etc., which needs expensive processing and complex packaging. As optics is scaled down, production volume needs to be increased tremendously. Also requirements on losses and signal integrity are less stringent for shorter reach communication. To reduce the cost of optical components, there needs to be a paradigm shift in doing optics from III-V based materials to cheaper, more readily available materials.

Silicon photonics offers a unique platform for cost effective, monolithic integration and mass production of optical and electronic elements on the same chip. Modern day Complementary metal oxide semiconductor (CMOS) technology is so advanced that cost/transistor has gone down from $1 in 1970s to less than $0.0000001 today. Si photonics promises to leverage this infras-

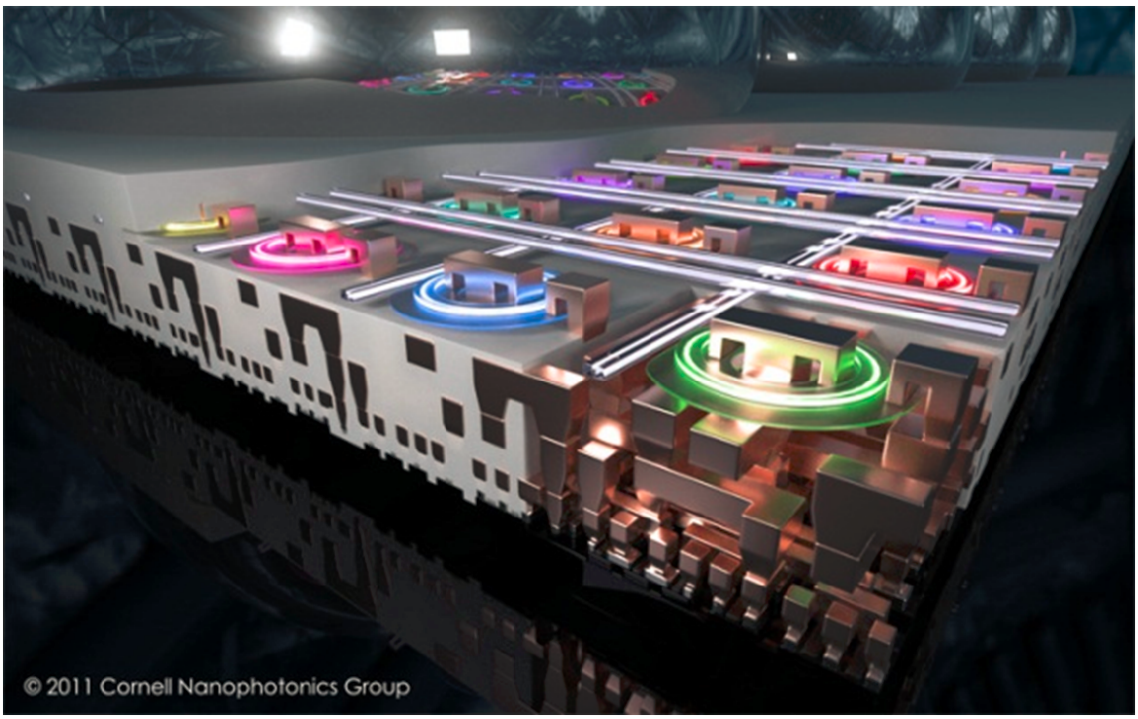

Figure 1.1: Vision of Silicon Photonics. Credit - Lucas Gabrielli.

tructure for manufacturing optics, making small distance optical interconnection not only cost effective but also possibility of co-integration of electronics and optics on one chip. Several optical devices have been demonstrated in Si like low loss waveguides [3, 4, 5], couplers [6], modulators [7, 8, 9], photo detectors [10, 11, 12], hybrid lasers [13] and prototype transmitter–receiver links [14, 15, 16]. Vision of SiP is shown in Fig. 1.1, where electronics and optics are co-integrated on one chip.

Many of these optical networks use resonators, where light can undergo multiple round trips to enhance light matter interaction. Most commonly used resonators in silicon are microdisks or microrings. A ring resonator based optical network is shown in Fig. 1.2. Resonators are versatile elements which can be used to design switches, filters, modulators, mux-demux etc. They are high-Q, compact, tunable and low power devices. The drawback of resonators is their

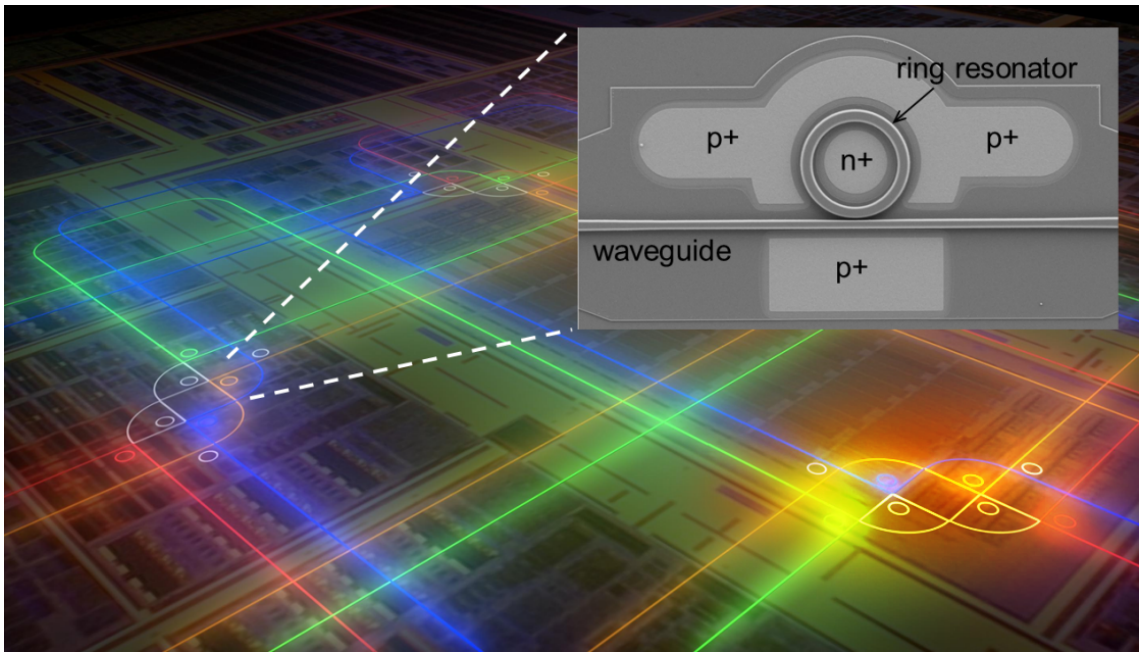

Figure 1.2: Ring resonator based optical network. Inset shows a fabricated ring resonator in Si. Credit - Nick Sherwood, Long Chen.

narrow bandwidth which leads to problems like post fabrication wavelength trimming and temperature sensitivity. The ability to make these compact high-Q resonators in Si has revolutionized not only optical interconnects, but other fields like sensing, metrology, biophotonics, non-linear optics and integrated quantum computing.

1.2 Thermal sensitivity of photonic devices

Sensitivity of any photonic structure to ambient temperature fluctuations stems from the fact that increase in temperature increases the refractive index of all commonly used materials like Si, SiO_2, Si_3N_4 etc. This is called thermo-optic effect, which is a fundamental material property. Thermo-optic coefficient (TO) of a material is a measure of temperature sensitivity of the refractive index

$\left(TO = \frac{1}{n}\frac{\partial n}{\partial T}\right)$. Thermo-optic coefficient of Si (1.86×10^{-4}) is almost an order of magnitude higher than oxides and nitrides. Temperature sensitivity of any photonic device can be quantified as

$$\frac{\partial \lambda_0}{\partial T} = \frac{\lambda_0}{n_g(\lambda)}\frac{\partial n_{eff}}{\partial T} \tag{1.1}$$

where λ_0 refers to resonance wavelength in case of a resonator or fringe minima wavelength in case of an interferometer, n_g is the group index. This leads to a resonance sensitivity of $\sim$0.1nm/K for an optical mode tightly confined in Si, irrespective of cavity design or dimension. This sensitivity is frequently exploited to tune the resonance wavelength. But this sensitivity also makes Si photonic devices extremely sensitive to ambient temperature fluctuations. This problem is especially compounded in resonator based systems due to enhanced light-matter interaction and narrowband optical responses. Fig. 1.3 compares the temperature sensitivity of Si based interferometer (order 50) and resonator (Q=10000). Even though wavelength change due to change in temperature is exactly same in both cases, transmission change is significantly higher for a resonator due to narrower transmission bandwidth. Typical temperature fluctuations in a commercial microprocessor can be 10s of degrees within a local hotspot [17]. Based on Fig. 1.3, one can see that such a resonator, which is typically used in modulators and filters, will go out of operation (resonance frequency will shift by half linewidth) with only 1 degree change in temperature. Such extreme temperature sensitivity cannot be tolerated in any realistic application. Hence this is one of the outstanding problems in the field, preventing practical integration of silicon photonic devices.

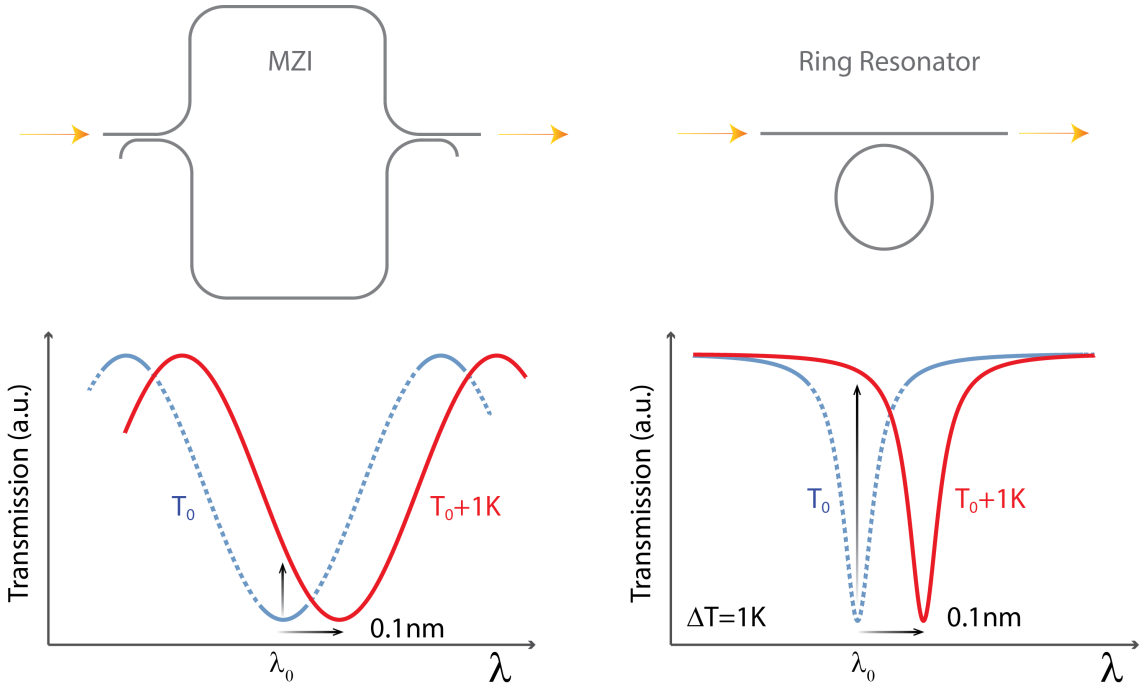

Figure 1.3: Temperature sensitivity of an interferometer and a resonator.

1.3 Prior art in thermal stabilization of photonic devices

Most of the solutions proposed to overcome this problem were either active or not compatible with CMOS processing. Certain polymers with negative thermo-optic coefficient have been explored as an overcladding for Si based devices [18, 19, 20, 21]. However these polymers are not compatible with front-end CMOS processing due to high temperature steps, and also have long term reliability issues. Furthermore since most of these polymers have low refractive indices, the optical mode is Si needs to be delocalized significantly to achieve athermal operation. This leads to large footprint and resonance tuning difficulties.

Active temperature compensation schemes appear to be most popular currently because of their ease of implementation [22, 23, 24]. They require a local

temperature sensor and wavelength tuning mechanism for every resonator on the chip. Typically a p-n junction diode or a resistor acts as temperature sensor [25]. Temperature information can also be obtained by tapping a part of the optical signal using a drop port in a resonator and sending the signal to a photodiode [22]. Thermo-optic or electro-optic effects are most commonly employed for resonance wavelength tuning [26, 27, 28, 29]. The former makes use of the relatively large thermo-optic coefficient of Si (same reason that makes Si devices especially susceptible to temperature variations). Resistive heaters are usually fabricated in close proximity to the resonator to change its local temperature. However to avoid metal induced optical losses, the heater cannot be placed too close to the optical elements. The most common implementation is placing the heater on top of an oxide cladding few microns thick [30]. This increased thermal resistance between the heater and the resonator lowers the tuning efficiency (nm/W or free spectral range (FSR)/W). Some recent works have tried to improve this efficiency by either thermal isolation of devices [31] or heater placement in dark zones of a resonator [27]. Despite low efficiency, thermo-optic tuning is lossless, modestly fast ($\sim$us) and hence very popular. Electro-optic tuning is achieved through carrier induced plasma dispersion effect [32]. This effect is most commonly used in making Si optical modulators because of its fast response times ($\sim$ns) [33]. However due to free carrier induced optical losses and carrier recombination, electro-optic tuning cannot be used to for large tuning range or large hold times. The biggest drawback of all these active tuning schemes is the extra power overhead to have the feedback loop and tuning element running all the time. In fact, many studies estimate this stabilization power consumption as the biggest component of the overall power budget [34, 35, 36], and one of the biggest roadblock in practical implementation

of Si photonic networks on-chip.

In the coming chapters we will describe multiple solutions that demonstrate passive, CMOS-compatible thermal stabilization of Si photonic devices. They cover a very wide design space – all Si devices, system based thermal stabilization, integration of novel materials and co design of optics and MEMS (micro electro mechanical systems). We will also describe other novel functionalities enabled by some of these schemes and how optics can be engineered to control temperature at nanoscale. We hope that this work will go a long way in mitigating the thermal problem in silicon photonics.

CHAPTER 2

"SMART" INTERFEROMETER BASED THERMAL COMPENSATION

2.1 Introduction

In this chapter, we present a scheme for thermal stabilization of Silicon photonic devices based on their system level design. We stick to conventionally used silicon-on-insulator (SOI) platform and high index contrast Si resonators. Thermal response is engineered by designing Mach-Zehnder interferometers (MZI) with tunable temperature sensitivity. We call them "Smart" MZI since their thermo-optic properties can be adjusted on-demand, and resonators can be coupled to them for athermal operation. This scheme is fully CMOS-compatible and the resonators are completely untouched, so tuning and modulation schemes can be integrated without any design changes.

2.2 "Smart" MZI design

We propose and demonstrate an approach to eliminate the temperature sensitivity of MZIs by adjusting the thermo-optic effects of their interfering arms through their waveguide width and length optimization. We demonstrate that the thermal spectral shift can be brought down to near–zero over a wide temperature range, which to our knowledge is being reported for the first time. Note that a balanced MZI (both arm lengths being equal) does not suffer from temperature sensitivity however it cannot be used in many practical applications like filters and modulators, where a finite spectral range is desired. The

method shown here is applicable for MZIs of any free spectral range, and hence provides a technique of passively compensating MZIs to enable scalability for massively parallel systems

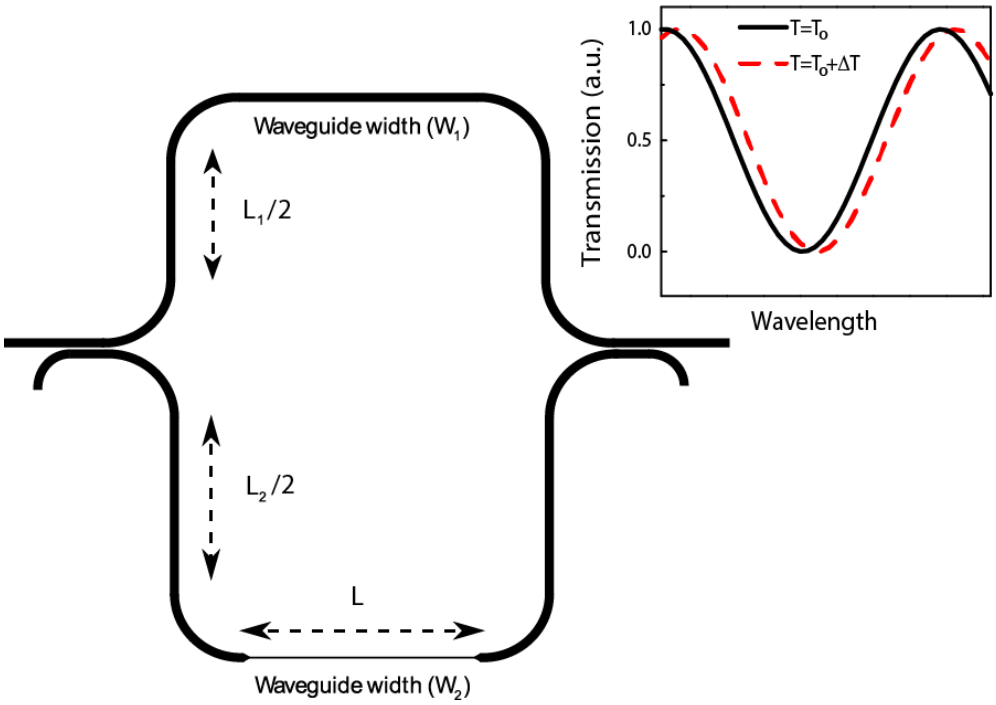

Figure 2.1: Schematic of the proposed device showing the various lengths and waveguide widths with the inset showing the effect of temperature on its transmission.

2.2.1 MZI Design

The proposed device works on the principle that the guided mode encounters different effective mode index changes with temperature $\left(\frac{\partial n_{eff}}{\partial T}\right)$ in the two arms of MZI, induced by different waveguide widths, and by choosing the arm lengths carefully the temperature sensitivity of one arm can be set to cancel that of the other, and overall temperature sensitivity can be brought down to zero. The key idea is to balance the thermo-optic effect between the two inter-

fering arms while still maintaining a certain phase difference between the two arms as required by the filter specification. Schematic of the device is shown in Figure 2.1. The device consists of two arms coupled using 3-dB directional couplers. While one of the arms propagates a length of L horizontally and L_1 vertically (as per schematic) with constant waveguide width of W_1, the other arm propagates a length L_2 with waveguide width of W_1 and tapers down to a width of W_2 ($W_2 < W_1$) for length L.

The overall temperature dependence of the device can be derived from the temperature dependence of the net optical path length, given by the difference in propagating lengths in the two arms (ΔL) with a given effective mode index (n_{eff}) and the difference in mode indices (Δn_{eff}) over a fixed length (L). It can be expressed as

$$m\lambda_0 = n_{eff}\Delta L + \Delta n_{eff} L \tag{2.1}$$

Here $\Delta L = L_2 - L_1$, $\Delta n_{eff} = n_{eff}(W_2) - n_{eff}(W_1)$ and m is the interference order at a given wavelength (λ_0). m can be chosen to be an integer to give constructive interference at that wavelength, or a half-integer to give destructive interference. We choose m to be a half integer and focus on the shift with temperature of a minima point of the spectrum. In practice m and λ_0 will be determined by the filter function requirements. Due to waveguide dispersion (the change in effective mode index versus wavelength), the interference order is modified as [37]

$$M = m - \Delta L\frac{\partial n_{eff}}{\partial \lambda} - L\frac{\partial(\Delta n_{eff})}{\partial \lambda} \tag{2.2}$$

The temperature sensitivity of any minima point of the spectrum can then

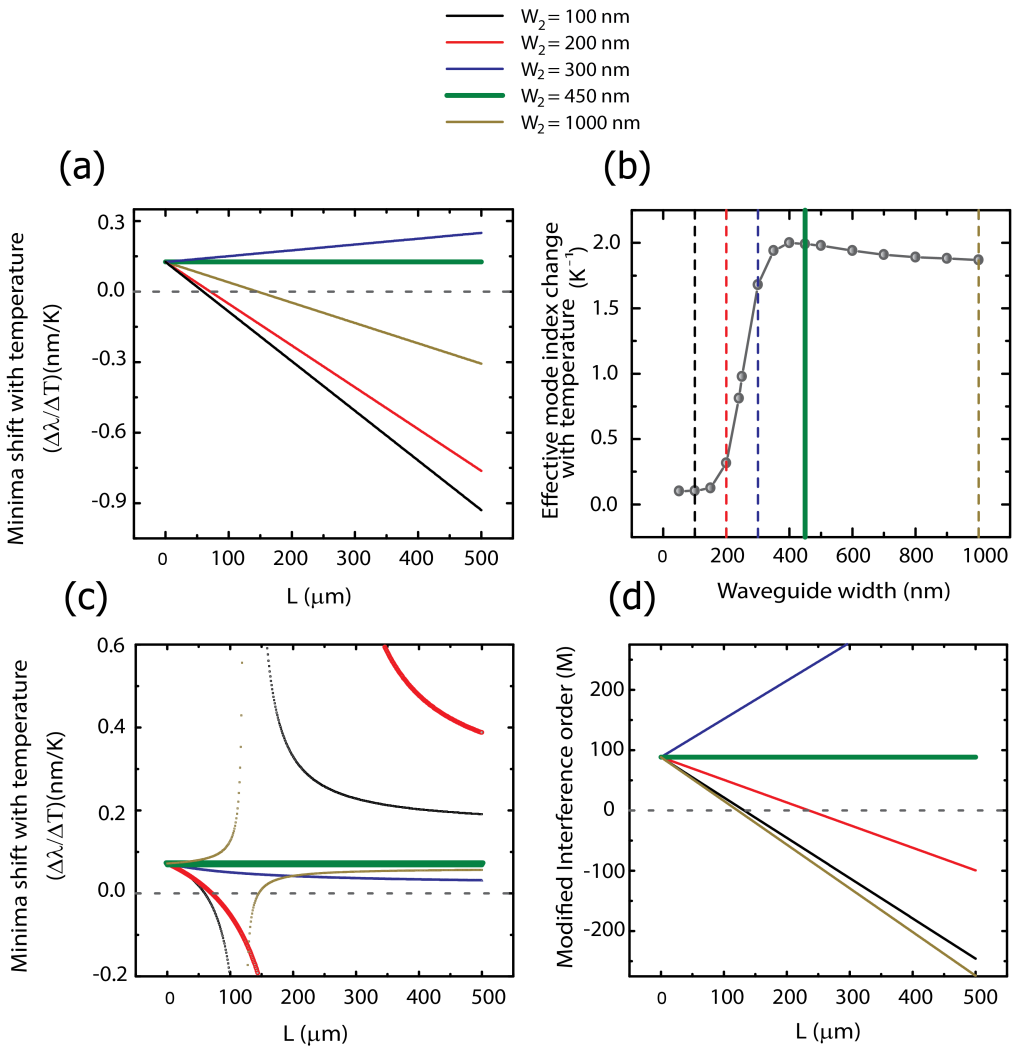

Figure 2.2: Controlling temperature sensitivity by varying waveguide width W_2 and length L given that W_1 is fixed at 450 nm and height of waveguides is 250nm (a). Spectral shift with temperature as a function of length for different waveguide widths (W_2) without including dispersion effect. (b) Effective mode index sensitivity to temperature for various waveguide widths, with values corresponding to those used in other plots being highlighted (c). Spectral shift with temperature as a function of length for different waveguide widths (W_2) taking dispersion into account. (d). Resulting interference order plotted against length of MZI.

be expressed as [37]

$$\frac{\Delta\lambda_0}{\Delta T} = \frac{\Delta L \frac{\partial n_{eff}}{\partial T} + L \frac{\partial(\Delta n_{eff})}{\partial T}}{M} \tag{2.3}$$

From Eqn.(2.3) it can be shown that if ΔL and Δn_{eff} are chosen appropriately with proper signs, the minima shift can be brought down to zero. The waveguides, in our case, have a fixed height of 250 nm. We calculate the effective indices n_{eff}, $\frac{\partial n_{eff}}{\partial T}$ and $\frac{\partial n_{eff}}{\partial \lambda}$ for TE modes of different waveguide widths using a full-vector finite element mode solver (COMSOL). For our calculations we take TO coefficient of Si as $1.86 \times 10^{-4} K^{-1}$ [38] and that of the oxide cladding as $1 \times 10^{-5} K^{-1}$. W_1 is fixed as 450 nm while W_2 is varied and the corresponding thermal spectral shifts are studied. Below are the results for a MZI designed for an interference order (m) of 50.5 at 1550 nm.

The dependence of on the MZI design length (L) is determined by dispersion and choice of differential $\frac{\partial n_{eff}}{\partial T}$. Figure 2.2(a) shows the temperature sensitivity without dispersion, while Figure 2.2(c) takes into account the effect of dispersion. As evident, dispersion not only changes the $\frac{\Delta \lambda}{\Delta T}$ profile from linear to hyperbolic, it also reverses sign after passing through zero dispersion point [37]. The effect of dispersion has to be taken into account to accurately model the temperature sensitivity.

Compactness and robustness of the device are determined by the choice of differential widths, which manifest in differential $\frac{\partial n_{eff}}{\partial T}$. Figure 2.2(b) shows the magnitude of $\frac{\partial n_{eff}}{\partial T}$ at 1550 nm for different waveguide widths whose height was fixed at 250 nm and Figure 2.2(c) shows the temperature sensitivity of the spectra vs. length of the device for different differential widths ($W_1 = 450nm$ and $W_2 = 100, 200, 300, 450, 1000nm$). Length of the device (L) required to achieve a given spectral shift decreases as the difference of $\frac{\partial n_{eff}}{\partial T}$ in the two arms increases. From Figure 2.2(c) it can be seen that very large difference in $\frac{\partial n_{eff}}{\partial T}$ can be achieved by choosing a width of around 450 nm in one arm, and 100 –

300 nm in the other arm. But if the difference in widths is too large, the spectral shift $\frac{\Delta\lambda}{\Delta T}$ becomes extremely sensitive to length and waveguide dimensions, so that even a small error due to fabrication imperfection can lead to significant drift of measured $\frac{\Delta\lambda}{\Delta T}$ from predicted value. Also thinner waveguides have a delocalized mode and higher propagation losses which leads to poor extinction. Hence we avoid extremely narrow waveguide width in our design.

In our design we choose $W_1 = 450nm$ and $W_2 = 200nm$ to give us close to an order of magnitude difference in $\frac{\partial n_{eff}}{\partial T}$ of each arm ($1.99 \times 10^{-4}K^{-1}$ for W_1 and 3.16×10^{-5} for W_2). Note that it is important to maintain the modified interference order (M) far from zero to increase fabrication tolerances. The dimensions chosen allows us to design very compact structures while keeping the interference order $M > 0$ at $\frac{\Delta\lambda}{\Delta T} = 0$. Such devices are broadband and functional over a wide spectral range. For example, a MZI designed using the above parameters for zero spectral shift with temperature at 1550 nm will have a temperature sensitivity change of $-1.5613 \times 10^{-4}nm/K$ over the entire C–band (1530 – 1561 nm).

2.2.2 Fabrication

The devices were fabricated on a silicon-on-insulator (SOI) wafer with 240nm Si thickness and $3\,\mu$m buried oxide thickness. 100nm of SiO_2 was deposited on the Si layer to act as hard mask. The pattern was transferred using ma-N 2403 negative resist and electron-beam lithography. Then the oxide was etched using reactive ion etching (RIE). After stripping the resist, a Cl_2 ICP (inductively coupled plasma) etcher was used to etch the Si. The devices were finally cladded

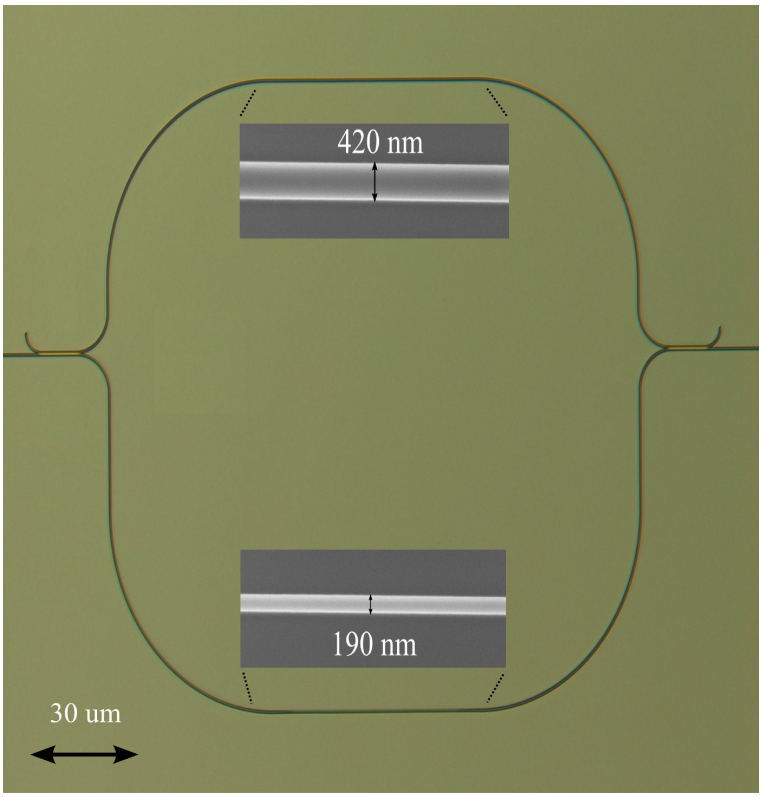

Figure 2.3: Microscope image of the MZI designed to give zero spectral shift with temperature (L=69 µm and ΔL=63 µm). SEM images of the wide and narrow waveguides are shown as insets, and their corresponding measured widths. The directional couplers have a gap of 200nm and couple over a length of 14.5 µm.

with 3 µm of plasma enhanced chemical vapor deposition (PECVD) oxide. Figure 2.3 shows a microscope image of the MZI designed to give zero spectral shift with temperature along with insets showing scanning electron microscope (SEM) of the wide and narrow waveguides. The waveguide widths were measured to be 420nm and 190nm for wide and narrow waveguides respectively. The waveguides taper over a length of 10 µm at the width transition regions. Several devices were designed for the same interference order of 50.5 at 1550 nm, but different lengths (L) inducing different spectral shifts with temperature. An uncompensated device with constant waveguide width of 450nm was also fabricated for reference.

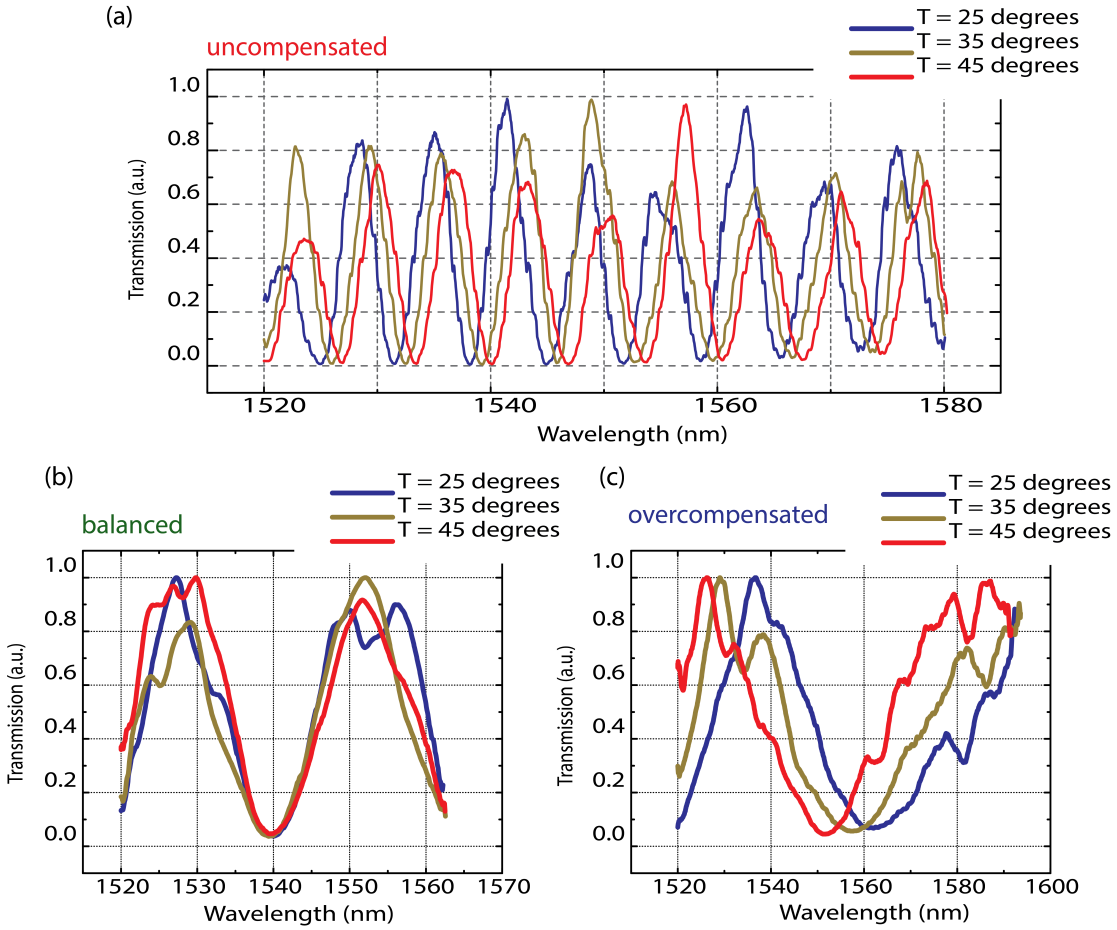

Figure 2.4: Transmission spectra of devices at different temperatures. (a) Uncompensated (0.09 nm/K) spectral shift with temperature (b) Fully compensated spectral shift with temperature with L=69 µm. (c) Overcompensated (-0.54 nm/K) spectral shift with temperature with L=150 µm.

2.2.3 Experiment

We show near-zero ($0.005nm/K$) temperature dependence of an MZI in Figure 2.4(b). For comparison Figure 2.4(a) shows uncompensated spectral shifts $(0.09nm/K)$ and Figure 2.4(c) shows overcompensated spectral shifts $(-0.54nm/K)$ with temperature. Transmission spectra of the devices in all cases correspond to TE polarization. The temperature insensitive MZI was found to operate over a very wide range of temperature (greater than 50 degrees) with

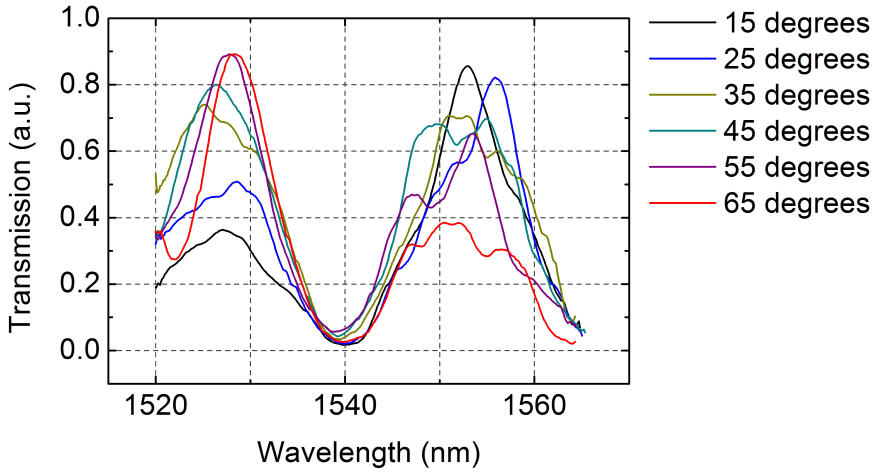

Figure 2.5: Operation of temperature insensitive MZI over 50 degrees. The change is extinction ratio with temperature is attributed to the variation of direction coupler efficiency with temperature.

no significant shift in the transmission minima, as shown in Figure 2.5. Fundamentally the device operates over a temperature range in which the dielectric refractive indices change linearly. Hence it provides an attractive platform for designing devices to work over a wide temperature range. The ringing effect seen in the transmission spectra is due to reflection at the directional coupler interface. Also extinction ratio changes slightly with temperature due to change of coupling ratio at the directional coupler ports. This can be eliminated by replacing the 3–dB directional couplers with Y–splitters or multimode interferometers (MMIs) which exhibit uniform power splitting regardless of the refractive index change.

As illustrated in Figure 2.6, the measured thermal spectral shifts agree well with the theoretically predicted values using Eqn.(2.3). In our calculations we take into account the measured waveguide widths ($W_1 = 420nm$ and $W_2 = 190nm$). The tapered regions were also taken into consideration while calculating the spectral behavior of the device. The dashed line corresponds

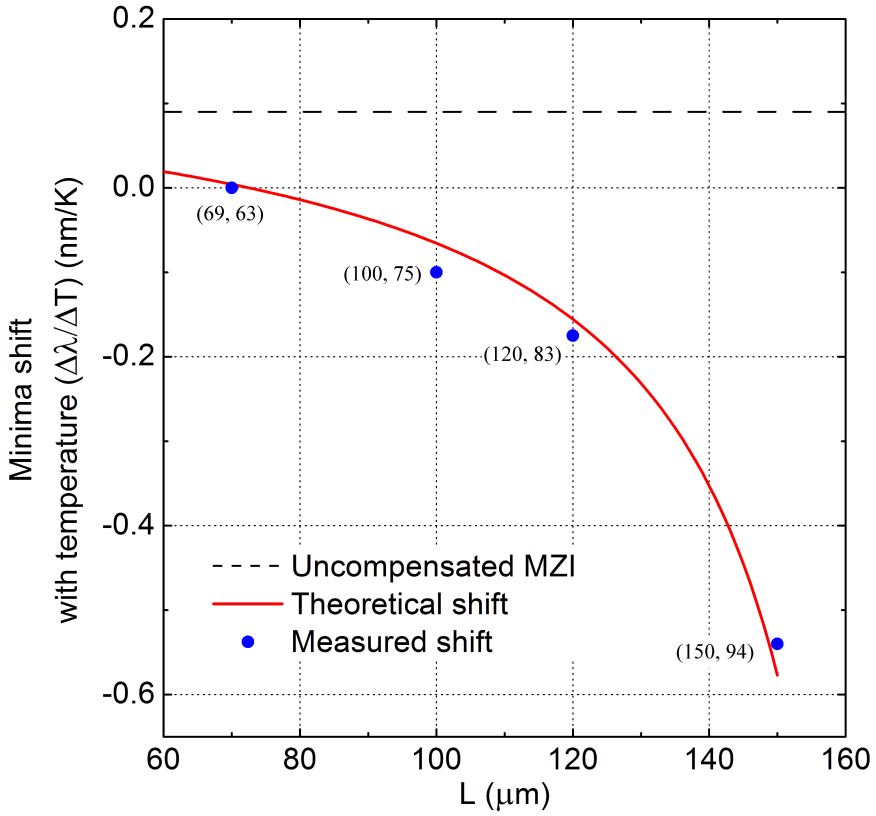

Figure 2.6: Measured spectral shift with temperature compared with theoretically calculated values. Spectral shift for uncompensated MZIs is added for reference (0.09 nm/K) for a constant waveguide width of 450nm. The numbers in parenthesis indicate (L, ΔL) in μm for the corresponding device. The devices were designed for an interference order of $m = 50.5$.

to the uncompensated MZIs whose sensitivity was measured to be 0.09 nm/K. In our devices, we were able to demonstrate spectral shifts as small as 0.005 nm/K and as large as -0.54 nm/K. The mismatch between measured and theoretical values becomes somewhat large at relatively large $\frac{\Delta\lambda}{\Delta T}$ values when the exact dispersion profile becomes relevant. It is important to keep in mind that $\frac{\Delta\lambda}{\Delta T}$ would have linear dependence on in absence of any dispersion. It is the dispersion modified interference order (M) that adds a hyperbolic dependence.

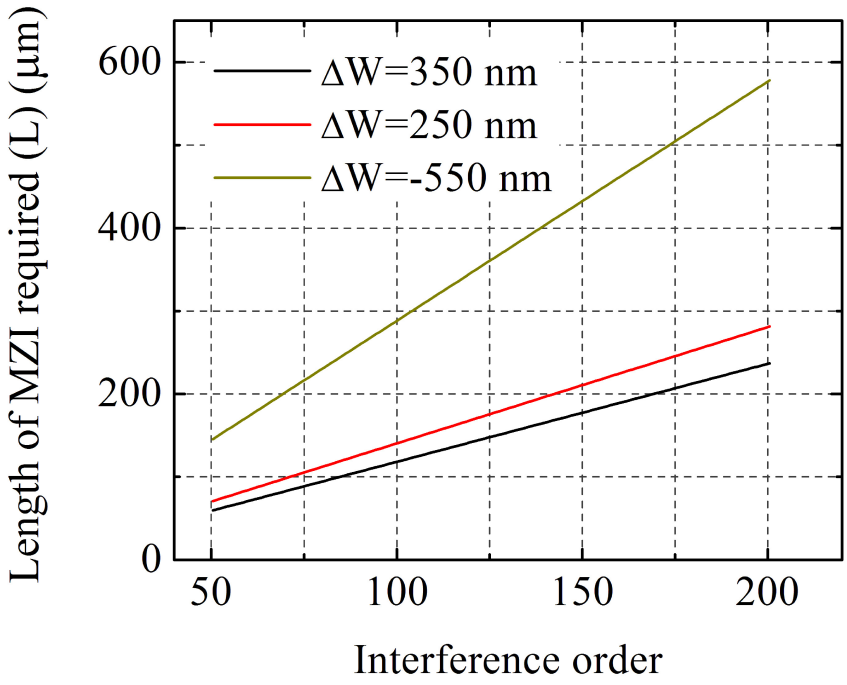

Figure 2.7: Design of temperature insensitive MZIs for any targeted Free Spectral Range (FSR). The interference order corresponds (M) to a minima at 1550nm.

2.2.4 Discussion

This design for temperature insensitive devices is fully scalable and applicable for a wide range of interference orders, i.e., free-spectral ranges of commonly used filters. This is illustrated in Figure 2.7, which shows the length of MZI (L) required to achieve temperature insensitivity for a wide range of interference orders. $(L, \Delta L)$ combination is chosen for a given m based on Eqn.(2.1) and Eqn.(2.3). Three cases are considered where the width of one of the arms is varied $(100, 200\&1000nm)$ keeping the other arm fixed at 450nm. The length of the device required increases linearly with interference order. Note however that the waveguides can be routed in a coiled manner in each arm to optimize area. The device size scales down with increasing difference in $\frac{\partial n_{eff}}{\partial T}$ between

the two arms (refer Figure 2.2(b)).

The proposed approach is applicable for any waveguide geometry strip, slot or rib waveguides. The application for rib waveguides is especially promising since it can be used to make temperature insensitive free carrier injection based modulators in silicon. For e.g., the MZI based modulator proposed by IBM [7] uses rib waveguides 550nm wide and 220nm tall, with a silicon slab of 35nm for electrical injection. $80\,\mu$m path length difference gives a V_π.L=0.36 V–mm. Simulations show that the same specifications can be achieved, along with temperature insensitivity, in a MZI with L = $591.93\,\mu$m and ΔL = $82\,\mu$m (with reference to Figure 2.1). The wide and narrow waveguide widths were taken as 550nm and 300nm with other rib parameters unchanged.

We have demonstrated that integrated Mach-Zehnder interferometers can be custom designed to give temperature insensitive operation over a wide temperature range by choosing right combination of wide and narrow waveguides. We have also shown how dispersion modifies the dependence of spectral shift with device length, and how proper choice of differential waveguide geometry can allow us to design robust devices whose measured thermal sensitivity agrees very well theoretically predicted values. The approach demonstrated here can lead to passive thermal compensation of CMOS–compatible optical filters, switches and modulators. These devices, when in the overcompensated mode, can also achieve large negative spectral shifts and therefore give rise to novel devices that, for example, compensate other devices with traditional positive temperature induced spectral shift.

2.3 Athermal Ring Resonators

We propose a new class of resonant silicon optical devices, consisting of a ring resonator coupled to a Mach-Zehnder interferometer, which is passively temperature compensated by tailoring the optical mode confinement in the waveguides. We demonstrate operation of the device over a wide temperature range of 80 degrees. The fundamental principle behind this work can be extended to other photonic devices based on resonators such as modulators, routers, switches and filters.

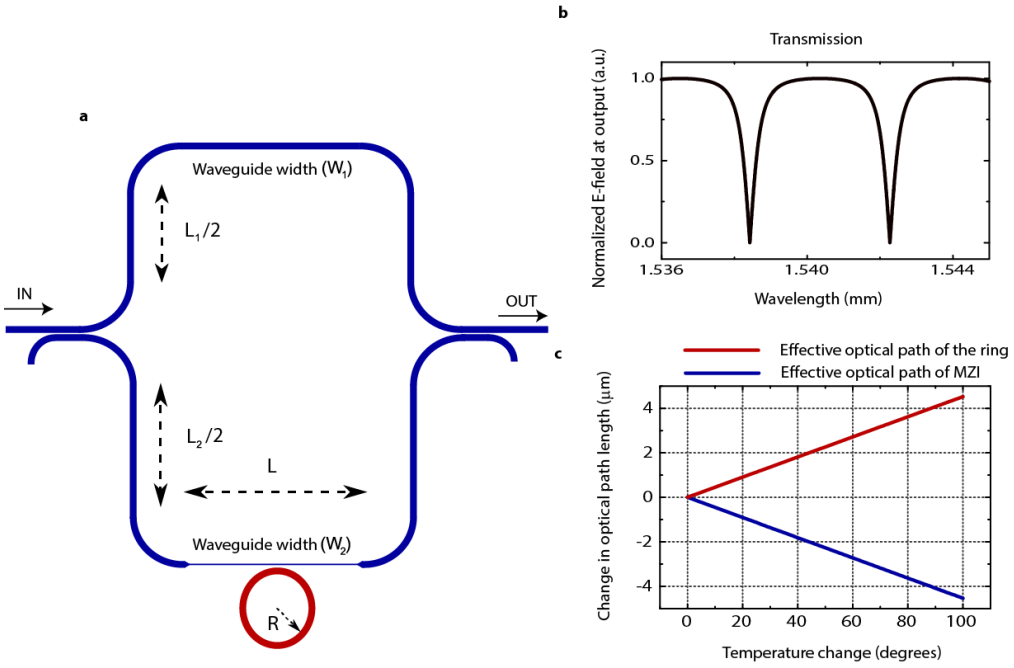

Figure 2.8: (a) Schematic of the device showing the various waveguide lengths and widths. The MZI is highlighted in blue and the ring in red. (b) Typical transmission spectrum for such a device with 40 μm ring radius and the MZI is balanced, i.e. the overall path lengths of the two arms are equal. (c) Change in optical path length with temperature for the ring and MZI. The devices are designed to have opposite and equal phase shifts with increase in temperature.

2.3.1 Athermal Design

We control the thermal drift of photonic structures by tailoring the degree of optical confinement in silicon waveguides. The basic photonic structure we propose consists of a ring resonator overcoupled to a balanced Mach-Zehnder interferometer (MZI) [39, 40]. The schematic of the device is shown in Fig 2.8(a). The additional degree of freedom in the choice of waveguide widths [37, 41], apart from just the lengths, enables one to set the thermal dependence of the MZI to counteract the thermal drift of the ring. The waveguide widths and lengths are chosen in the two arms of the MZI to give a balanced transmission (net optical path length difference in MZI ($\Delta\phi_{MZI}$) is zero) (see Fig 2.8(b)) while having a strong negative temperature sensitivity overall $\left(\frac{\partial}{\partial T}\Delta\phi_{MZI} < 0\right)$. The ring has a large enough waveguide width to enable highly confined single mode operation, and consequently strong positive temperature sensitivity $\left(\frac{\partial}{\partial T}\phi_{Ring} > 0\right)$. The relative temperature sensitivities of the ring and the MZI, compared in Fig 2.8(c), are designed to cancel each other out.

The device is made inherently robust to temperature changes - its resonance oscillates about a central wavelength with temperature instead of drifting away, as is the case in standard resonators, due to the periodic interplay of the ring and MZI phase change with temperature. These oscillations arise due to the difference in the linear phase induced by the MZI with temperature and the nonlinear phase induced by the ring. This phase difference, captured in Eqn.(2.4) [40], is converted into intensity modulation at the output of the structure.

$$\frac{\partial}{\partial T}\phi_{REMZI} = \frac{\partial}{\partial T}\left\{phase\left(\frac{t - \alpha e^{i\beta L_{Ring}(T)}}{1 - \alpha t e^{i\beta L_{Ring}(T)}}\right)\right\} + \frac{\partial}{\partial T}\left\{\beta L_{MZI}(T)\right\} \tag{2.4}$$

where $phase(X) = \tan^{-1}\left(\frac{Im(X)}{Re(X)}\right)$, X being a complex number, L_{Ring} and L_{MZI} are the net optical path lengths for the ring and the MZI respectively, t is the cross coupling coefficient of the ring to waveguide, $(1-\alpha)$ is the roundtrip loss in the ring and β is the propagation constant in air. The waveguide widths are used to tailor L_{Ring} and L_{MZI}. The first term in Eqn.(2.4) is the change of phase induced by the ring with temperature, which redshifts the resonance with increase in temperature; while the second term refers to the change in optical path lengths of the two arms of the MZI with temperature designed to have a strong negative value, which compensates for the phase change of the ring. The difference between these phases can be seen in Fig 2.9(a) where we plot, as an example, the phase change at a given wavelength of a $40\,\mu$m radius ring resonator as a function of temperature, and the phase added of the MZI at that wavelength. It can be see that the nonlinearity of the ring phase gives rise to two distinct regions - one where the MZI added phase is smaller than the compensating phase required, and one where the MZI added phase is larger than the compensating phase required. The corresponding resonance lineshapes at each of these temperature ranges is shown in Fig 2.9(b). For a temperature change of T_{per} the resonance lineshape exactly corresponds to the one at base temperature; hence T_{per} is defined as one temperature cycle within which the resonance undergoes a complete oscillation as shown in Fig 2.9(b). It is this periodic mismatch between the phase added by the MZI and the phase compensation required that gives rise to oscillation in the ring resonance with temperature.

For a ring of given radius, only a particular choice of compensating MZI can result in perfect oscillations in the ring resonance with temperature. If the compensation is too large or too small, the ring resonance drifts away with increase of temperature while still exhibiting the periodic behaviour. This is in sharp

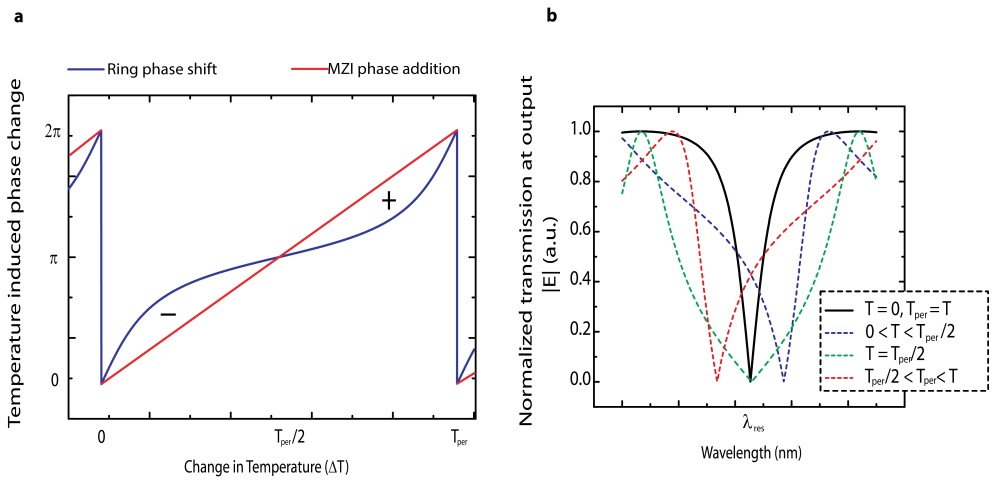

Figure 2.9: (a) Phase change induced by in ring and by the MZI with temperature. The inherent nonlinearity in the ring phase gives rise to distinct overcompensated and uncompensated regions. This behavior repeats itself after one temperature period T_{per}. (b) Corresponding resonance lineshapes at different temperatures within one temperature period. The resonance displays periodic oscillations centered at λ=λ_{res}.

contrast with normal ring resonator systems, where the resonance drifts monotonically with temperature. The locus of minima points of the spectra for such a system can be shown to vary with temperature as

$$\Delta\lambda_{min} = \left(\frac{\lambda_0}{L_{Ring} + \chi L_{MZI}}\right)\frac{\partial L_{Ring}}{\partial T}\left(T - \frac{2}{\beta\dfrac{\partial L_{Ring}}{\partial T}}\tan^{-1}\left\{\frac{1-t}{1+t}\tan\left(\frac{\gamma\beta\dfrac{\partial L_{Ring}}{\partial T}}{2}\right)\right\}\right) \tag{2.5}$$

where $\chi = \dfrac{1-t^2}{1+t^2+2t\cos(\beta L_{MZI})}$ and $\gamma = \dfrac{\left(\dfrac{\partial L_{MZI}}{\partial T}\right)}{\left(\dfrac{\partial L_{Ring}}{\partial T}\right)}$ is the compensation factor. Fig. 2.10(a) shows the behaviour of $\Delta\lambda_{min}$ for different cases of compensating factor (γ). Only when $\gamma = 1$, we get perfect oscillations in the resonance minima with temperature. If $\gamma > 1$, the ring is overcompensated and the resonance slowly blueshifts with temperature; while if $\gamma < 1$, the ring is un-

dercompensated and the resonance slowly redshifts. For reference, $\Delta\lambda_{min}$ shift with temperature for a normal uncompensated ring resonator is also shown in Fig. 2.10(a), which increases monotonically with temperature.

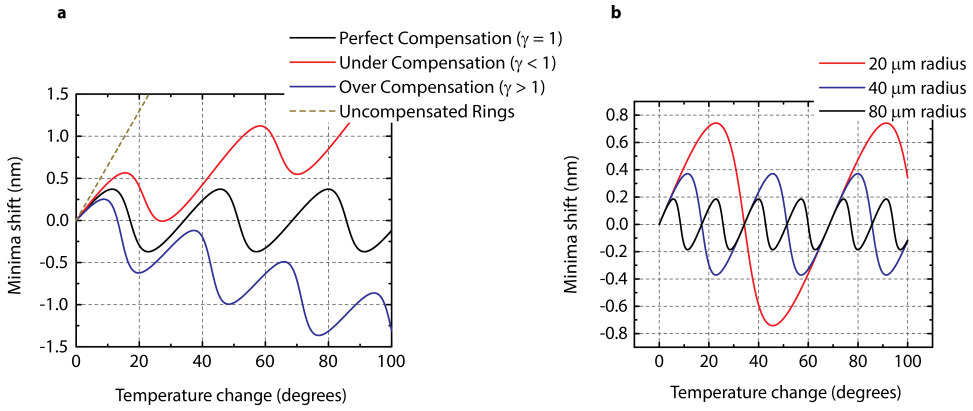

Figure 2.10: (a) Resonance minima shift for different cases of compensation for a ring resonator with $40\,\mu$m radius, showing the oscillatory behavior with temperature. The monotonic drift of an uncompensated ring is also added for reference. (b) Resonance minima shift with temperature for different ring resonator radii. The resonances oscillate less for larger rings, as compared to smaller rings.

Smaller oscillations with temperature can be achieved by using structures where the phase compensation mismatch is smaller. This can be achieved using a ring with a large radius (see Fig. 2.10(b)). Since the resonances of a larger ring are closely spaced, the phase compensation mismatch width (shown in Fig 2.9(a)) is smaller. Smaller oscillations can also be achieved by cascading multiple rings on a single MZI (for WDM (wavelength division multiplexing) systems [20]). From Eqn.(2.5), it can be deduced that N smaller rings with radii $R \pm \delta r$ coupled to one MZI behaves like a single ring with radius NR , and the resulting thermal oscillations ($\Delta\lambda_{min}$) are $\frac{1}{N}$ times smaller than single ring case.

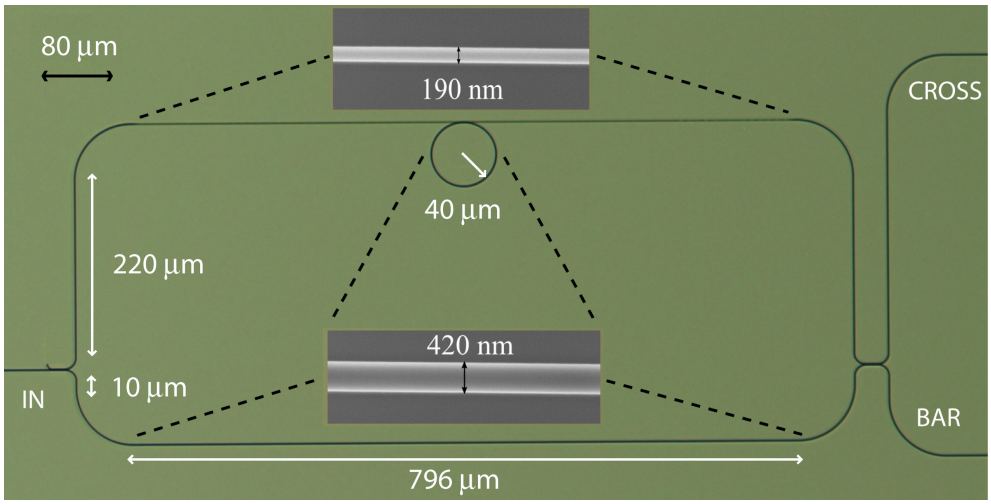

Figure 2.11: Optical microscope image of the device consisting of a 40 µm radius ring resonator coupled to a MZI whose lengths are shown. The coupling gap is 110nm. SEM insets show the actual waveguide widths at various parts of the device.

2.3.2 Fabrication

The devices were fabricated on a silicon-on-insulator (SOI) wafer with 240nm Si thickness and 3 µm buried oxide thickness. 100nm of SiO_2 was deposited on the Si layer to act as hard mask. The pattern was transferred using ma-N 2403 negative resist and electron-beam lithography. Then the oxide was etched using reactive ion etching (RIE). After stripping the resist, a Cl_2 ICP (inductively coupled plasma) etcher was used to etch the Si. The devices were finally cladded with 3 µm of plasma enhanced chemical vapor deposition (PECVD) oxide. Fig. 2.11 shows the optical microscope image of a 40 µm radius ring resonator coupled to a balanced MZI, with SEM insets showing the corresponding waveguide widths. The wide and narrow waveguide widths were measured to be 420nm and 190nm respectively. The waveguides taper over a length of 10 µm at the width transition regions. The ring-to-waveguide coupling gap was 110nm for this specific device. The lengths of the MZI arms are also shown

in Fig. 2.11. The measured quality factor of the ring was around 7000, a good value for switching and modulation applications for up to 40Gbps input data [42] (quality factor is defined for T=T_{per} (see Fig. 2.10(b))).

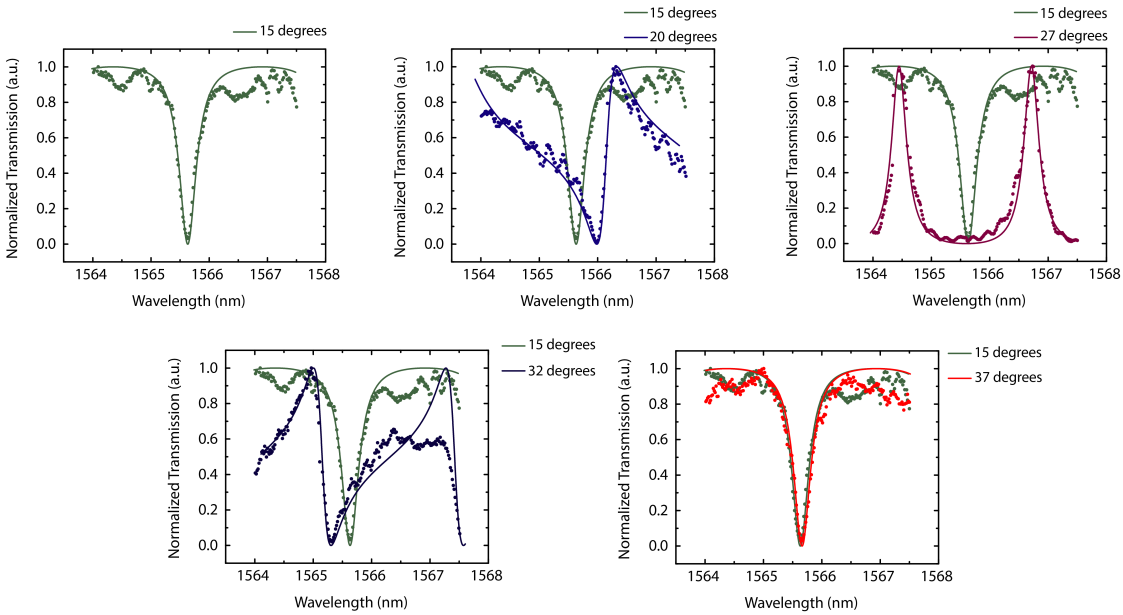

Figure 2.12: Bar port transmission spectrum of the device, centered around 1565.6nm, at different temperatures. The dots represent actual measured data, and the straight lines represent theoretical lineshapes at those temperatures.

2.3.3 Experiment

The fabricated devices show temperature stability over a large temperature range of over 80K. Transmission spectra of this device at the bar port were measured at different temperatures. The transmission around 1565.5nm for several different temperatures is shown in Fig. 2.12. For reference, the theoretical lineshapes at these temperatures are shown. The measured data agree very closely with the theoretical lineshapes. For a $40\,\mu$m radius silicon microring resonator, T_{per} is around 22 degrees (since the free spectral range is 2.2nm in the C–band).

In this particular case the oscillation in the wavelength at the transmission minima was less than 1nm. We measured less than 3 dB worst case degradation in the transmission minima.

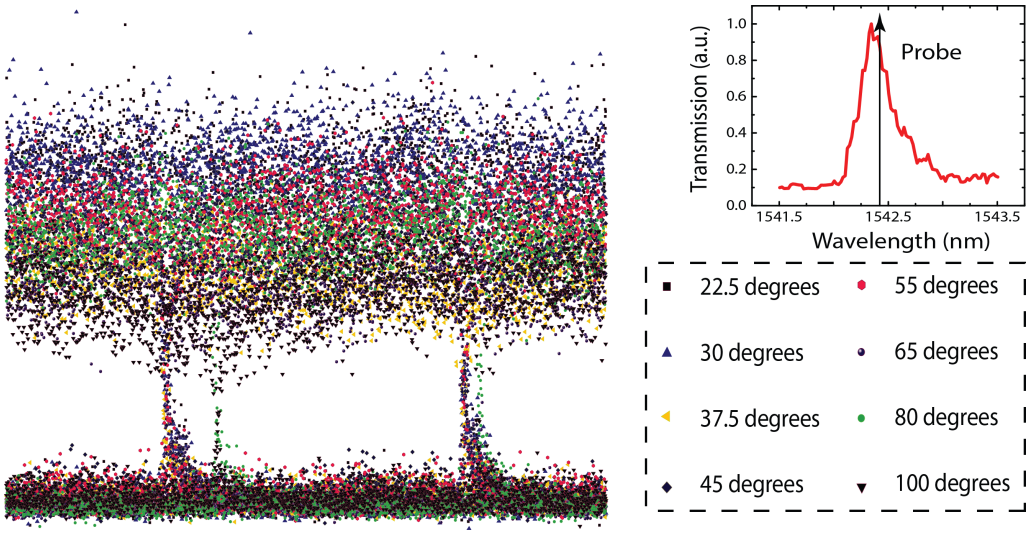

Figure 2.13: Eye patterns of 1Gbps input data at different temperatures overlaid. The probe wavelength was 1542.375nm, which corresponds to a bar port resonance at base temperature ($22.5\,^{\circ}$C). The eye-patterns show error free operation over around 80 degrees. Inset shows the laser position w.r.t resonance.

Continuous operation over 80 degrees was demonstrated by passing a 1Gbps, 2^7-1 pseudo-random data at a bar port resonance of 1542.375nm. The transmission wavelength was chosen slightly off-resonance at base temperature ($22.5\,^{\circ}$C) since the spectral lineshape was not perfectly lorenztian. Eye patterns were obtained at different temperatures. Fig. 2.13 shows the eye patterns at different temperatures overlaid together, which clearly shows that the eye never closes at any temperature. Note that the rise time is not clearly visible due to resolution limitation. In fact the quality factor of these eye patterns never goes below 10 with an error free operation (BER $< 10^{-12}$) [43, 44]. The eye opening decreases and increases with temperature as expected due to the oscillatory temperature dependence of the device.

2.3.4 Discussion

In summary, we have demonstrated for the first time a temperature insensitive resonator-based device on silicon, with no extra power required for thermal stabilization. The device is shown to operate over a wide temperature and spectral range. The device is expected to have high performance as long as the dielectric refractive indices change linearly with temperature. It is also assumed that both the ring and the MZI are located in the same thermal hotspot which is typically $500 \times 500 \mu m^2$ in commercial microprocessors [17]. The approach presented here can be used in a ring resonator modulator system by surrounding the ring with diodes. A reduction in footprint of the device could be achieved by using narrower waveguides in MZI arm, or routing the arms in a coiled manner. The performance of the device could be further enhanced by using splitters/ couplers which are refractive index independent (like Y–splitters, MMIs) instead of directional couplers. This approach is applicable for rib, slot or strip waveguides. This new generation of devices could lead to ultralow power on–chip optical interconnects capable of meeting the demands for the next generation of microprocessors.

2.4 Athermal Silicon microring modulator

We demonstrate a new class of passively temperature stabilized resonant silicon electro-optic modulators. The modulators consist of a ring resonator coupled to a Mach-Zehnder interferometer with tailored thermal properties. We demonstrate 2 GHz continuous modulation over a temperature range of $35\,^{\circ}\mathrm{C}$ and describe the scalability and design rules for such a device.

2.4.1 Modulator design for athermal operation

The modified MZI, that compensates the temperature dependence of the ring resonator, is designed by considering the optical paths of the ring and the MZI. The MZI has two sections: in one section each arm has waveguides of different widths (characterized by difference in their effective mode indices Δn_{eff}) but same length (L_{mzi}) while in another section, each arm has waveguides of same width (characterized by mode effective index n_{eff}) but different lengths (ΔL_{mzi}) (see Fig. 2.8). The ring resonator is overcoupled to the thinner arm of the MZI. The MZI is balanced, i.e. its interfering optical path lengths are equal to ensure that the overall spectrum is the one of the ring resonator, while its thermal sensitivity is equal and opposite to that of the resonator [45]. The shift in optical paths with temperature of the MZI and the ring are equal when the following is satisfied :

$$MZI(T) = \left[n_{eff} + \frac{\partial n_{eff}}{\partial T}T\right]\Delta L_{mzi} + \left[\Delta n_{eff} + \frac{\partial \Delta n_{eff}}{\partial T}T\right]L_{mzi} = -\left[\frac{\partial n_{eff}}{\partial T}T\right]2\pi R \quad (2.6)$$

where R is the ring radius. An athermal ring is then designed by equating

coefficients of T (T^0&T^1) and solving Eqn.(2.6) for L_{mzi} and ΔL_{mzi}.

2.4.2 Fabrication

We fabricate the athermal modulator by integrating a p-i-n diode around the ring resonator, which modulates the phase on one of the arms of the MZI. Thus the modulation scheme remains resonant (which preserves the low power of the modulator), while the MZI acts as a passive thermal stabilization device and translates any phase modulation at the ring into intensity modulation at the output. The devices were fabricated on 250nm silicon on insulator substrate using multiple e-beam lithography steps. The waveguides were etched using two step lithography leaving a 40nm slab only around the ring for the p-i-n diodes. Next, we performed the implantation steps for the p-region (BF_2) and n-region (Phosphorous). 1 µm SiO_2 was deposited as top cladding and multiple annealing steps were performed. Vias were then etched, followed by deposition of contacts and probe pads respectively. Fig. 2.14 shows a microscope image of the final fabricated device. The ring has a 80 µm radius while the MZI has a dimension of 418 µm by 1687 µm.The p-i-n diode had a forward resistance of 700 Ω.

2.4.3 Experiment & Performance

We show that the extinction ratio (ER) in our device varies only slightly with temperature and is consistently around 2dB. Fig 2.15(a-e) shows the normalized optical transmission change at the output, when a CW input laser with 1 µW

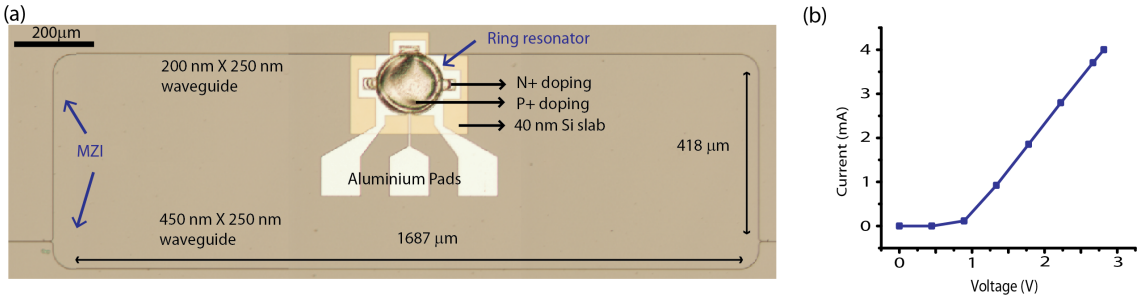

Figure 2.14: (a) Optical microscope image of the device, which consists of an $80\,\mu$m radius ring resonator coupled to a MZI. The ring has a p-i-n diode integrated around it. Waveguide cross sections at various parts of the device are shown. (b) I-V characteristics of the p-i-n diode.

power was set at the resonance wavelength of the ring (1555.3nm) and voltage across the diode was swept, for a temperature range of $20\,^{\circ}$C–$40\,^{\circ}$C. The optical power at the output undergoes a transition of around 2dB for all temperatures for a voltage swing of 1.5V indicating that at every temperature, for a fixed voltage swing, there is a finite modulation in optical transmission. The extinction ratio (shown by dotted lines) fluctuates with temperature but does not degrade severely. ER in our devices is mainly limited by the couplers at the input and output of the MZI. This can be easily improved by designing optimized 3dB couplers. Fig 2.15(f) shows the theoretical ER dependence with temperature spanning 40 degrees. ER decreases just as temperature starts increasing, increases around $10\,^{\circ}$C and decreases somewhat afterwards. For an $80\,\mu$m radius ring, the temperature period (T_{per}) was 20 degrees. This behavior keeps repeating for higher temperatures. This oscillation of the ER with temperature is due to the fact that even though the optical path change with temperature of both the MZI and ring can be designed to be equal and opposite, their phases cannot since the ring phase changes nonlinearly with temperature while the MZI phase changes linearly [45]. We show here that despite the limitation in the compensation approach, a finite ER is always maintained between the optical ON and

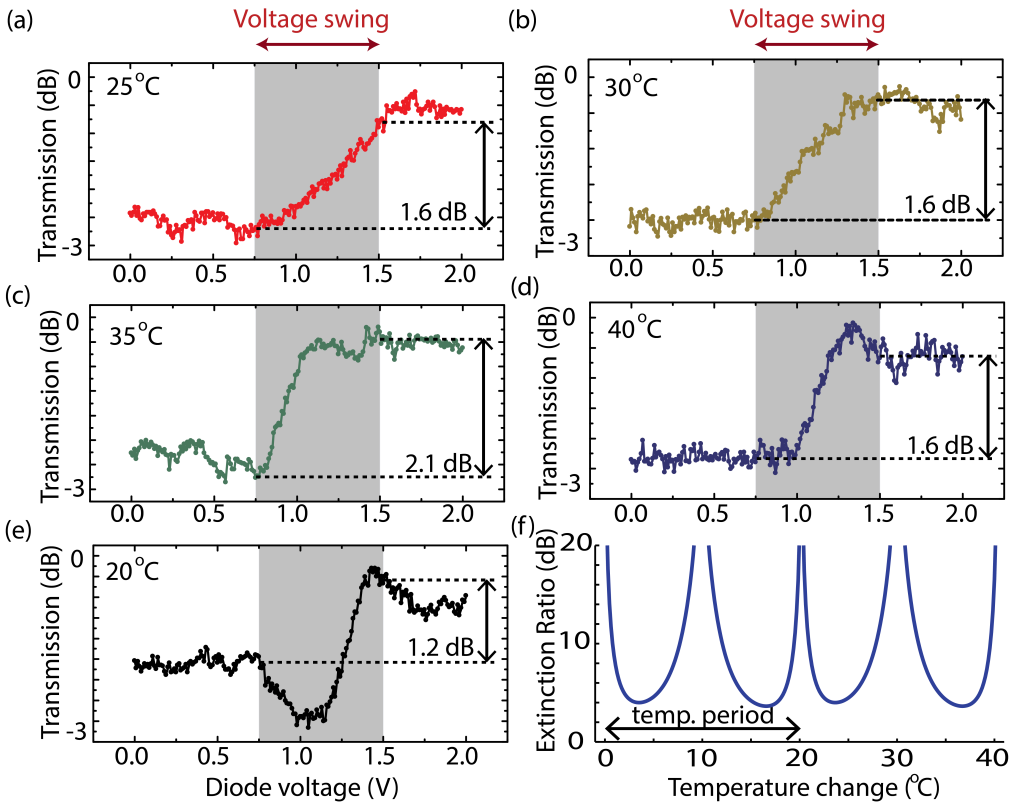

Figure 2.15: (a-e) DC measurement of optical power transition as diode voltage is changed for different temperatures. (f) Change in predicted optical extinction ratio with temperature over two temperature periods.

OFF states for all temperatures during modulation. In our calculations we considered a ring with 80 µm radius, n_g (group index) = 4.3, $\Delta n_{eff}/\Delta T = 1.8 \times 10^{-4}$, 2 dB/cm propagation loss and a coupling constant of 0.8 to the waveguide. A fixed electron-hole concentration $\Delta N = \Delta P = 1 \times 10^{18} cm^{-3}$ is added to the device, resulting in an effective index shift $\Delta n_{eff} = -0.003$ and absorption $\Delta\alpha = 14.5 cm^{-1}$ [32]. The modulation is assumed to be sufficient to shift the resonance by half of its linewidth. The resonator quality factor is 8000. Note that higher Q-factor would cause more assymetric lineshapes, which causes greater degradation of ER with change of temperature, and constraints adjacent channel spacing.

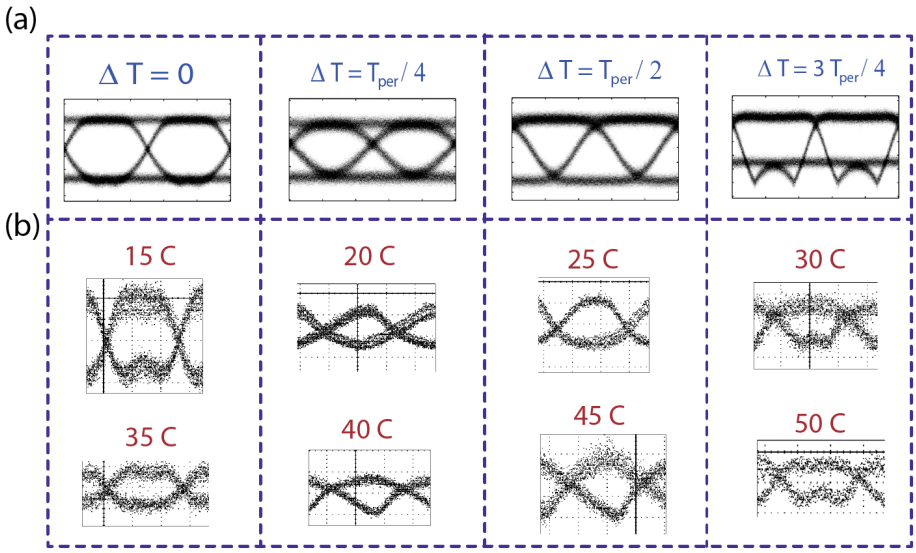

Figure 2.16: (a) simulated eye diagrams showing the periodic change in eye diagram shape with temperature over one temperature period. (b) 2 Gbps square wave modulation eye diagrams for different temperatures. Measurements span over two temperature periods. Corresponding predicted eye is shown in the top row.

We modulated the applied voltage to the device at 2 Gbps and demonstrated open eye diagrams, over a 35 degree temperature range (shown in Fig. 2.16(b)) which corresponds to two temperature periods. The modulation speed in our devices was limited by the contact resistance. In principle, with optimized p-i-n or p-n diode design, it should be possible to achieve much higher modulation speeds up to tens of GHz[33]. Fig. 2.16(a) shows simulated eye diagrams for previously mentioned modulation parameters with a Gaussian noise distribution. One can see that while there is a periodic change in the shape of the eye with change of temperature, as expected from Fig. 2.15 due to asymmetric lineshapes [45], they remain open. The measured eye diagrams also follow the same pattern (Fig. 2.16(b)) over a large temperature range.

2.4.4 Design trade-off

There is a trade-off between the device area and temperature operating range for such devices. The fluctuations in ER with temperature increases as the ring radius is reduced due to the corresponding increase in free spectral range (FSR) and therefore stronger nonlinear dependence of the ring resonator transmission with temperature. This trade-off can be optimized by limiting the working range and using the MZI to overcompensate the thermal redshift of a small ring resonator. In the overcompensated regime the blueshift of the MZI is stronger than redshift of the ring resonator limiting the detuning in ring resonance which in turn leads to improved ER over a given temperature range. Fig. 2.17(a-c) shows the theoretical modulation in optical transmission as a function of index perturbation (negative sign in Δn is due to carrier injection based modulation) for different temperatures for a ring with $10\,\mu$m radius and $\frac{\partial MZI(T)}{\partial T} = -5\left(2\pi R\frac{\partial n_{eff}}{\partial T}\right)$ (see Eqn.(2.6)). All other simulation parameters same as mentioned before. One can see that for three different temperatures, degradation in extinction ratio is minimal. Fig. 2.17(d) shows that extinction ratio is greater than 3dB over $-10\,^{\circ}$C to $15\,^{\circ}$C and falls off on either side of these two temperatures. This device has a working range of 25 degrees, which is sufficient for most practical applications, and an area approximately 10 times smaller than the device shown in Fig. 2.14. Note that device area can be also reduced by coiling the MZI arms, limited by the bending radius of the thinner arm.

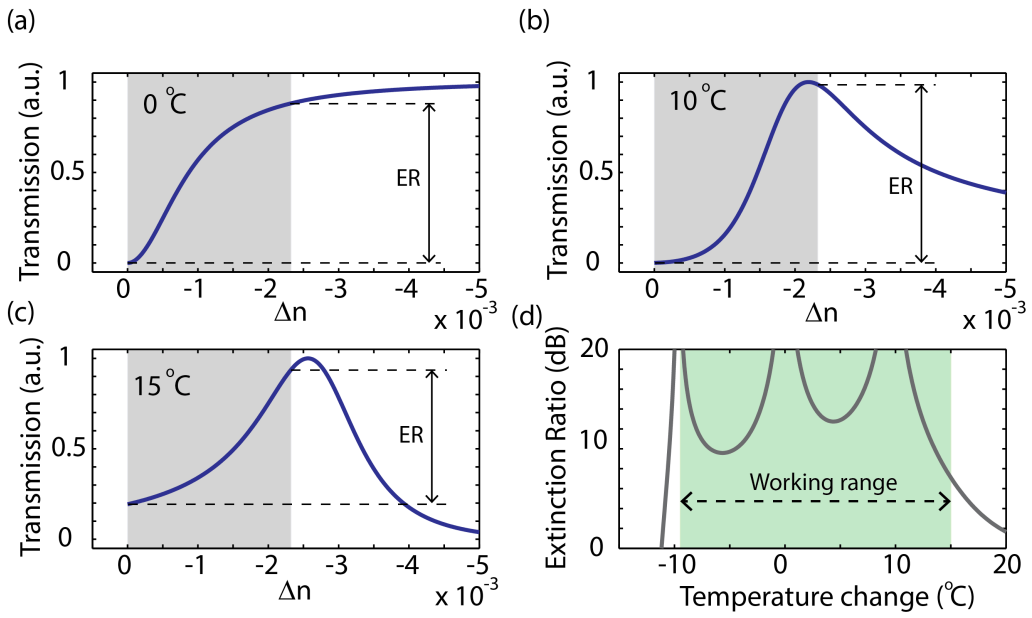

Figure 2.17: (a-c) Optical transmission change as a function of index perturbation of an overcompensated $10\mu m$ radius resonator at different temperatures. ER for a modulation of strength $\Delta n = -2.2 \times 10^{-3}$ is shown. Negative sign indicates resonance blueshift with carrier injection. (d) Change in optical extinction ratio with temperature.

2.4.5 Discussion

We showed the first demonstration of a silicon microring modulator working over a 35 degree temperature range with no extra power required for thermal stabilization. We presented design procedure and performance analysis of these devices and discussed how to reduce the device footprint. These devices can be custom designed based on the application specifications, and various parameters such as ring radius, compensation factor, coupling ratio, mode confinement etc. can be adjusted to achieve the desired performance. These MZI assisted resonant athermal devices are naturally suited for wavelength division multiplexing (WDM) applications since multiple rings can be coupled to the same arm of the MZI, to achieve thermal stabilization. Application of these compact and robust devices can be extended to switching, filtering and other on-chip

resonator based functionalities.

CHAPTER 3

ATHERMAL DESIGN USING A NEGATIVE THERMO–OPTIC CLADDING

3.1 Introduction

In this chapter we describe a novel approach for passive and CMOS-compatible temperature insensitive integrated optical devices using a metal-oxide cladding having negative thermo-optic effect. Metals oxides like TiO_2 and $SrTiO_3$ have been investigated in semiconductor industry as a gate dielectric [46]. These metal oxides also have negative thermo-optic coefficient due to presence of a soft electronic band [47] ($TO_{TiO_2} \sim -1 \times 10^{-4}K^{-1}, TO_{SrTiO_3} \sim -1 \times 10^{-5}K^{-1}$). This is in contrast to commonly available dielectrics and semiconductors which have positive thermo-optic coefficients ($TO_{Si} = 1.8 \times 10^{-4}K^{-1}, TO_{SiN} \sim 2 \times 10^{-5}K^{-1}, TO_{SiO_2} \sim 1 \times 10^{-5}K^{-1}$). There has been some limited effort in reducing temperature sensitivity of optical devices using TiO_2 overcladding [48, 49, 50]. Ref [49] has done a thorough analysis of TiO_2 deposition and showed close to athermal performance. Here we show that completely athermal optical devices can be realized by engineering the mode-overlap between Si based materials (Si / SiN/ SiO_2) and TiO_2. This scheme of temperature compensation is CMOS-compatible, lossless, does not require any extra footprint and can lead to very large temperature operating range.

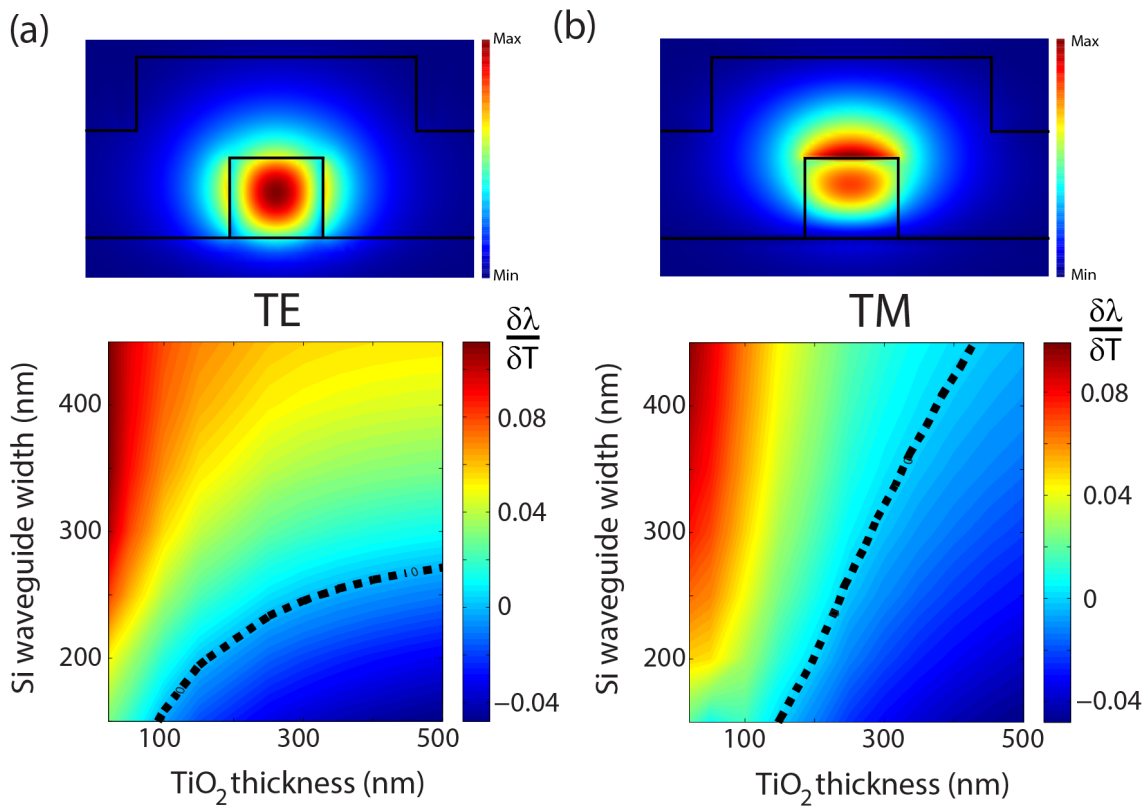

Figure 3.1: Resonance wavelength sensitivity to temperature ($\frac{\partial \lambda_0}{\partial T}$ in nm/K) for (a) TE and (b) TM polarizations. Si guiding layer is 220nm thick. Black dashed line represents the optimum waveguide width and cladding thickness for athermal operation. Energy flux density of optical modes in a 250nm wide waveguide is shown at the top. TiO_2 cladding thickness is 300nm.

3.2 Athermal design with TiO_2 cladding

3.2.1 Optical design

In order to ensure that the positive TO effect of the Si core is exactly cancelled out by negative TO effect of the cladding, we engineer the optical mode confinement in TiO_2 cladding layer by tailoring the waveguide dimension and the cladding thickness. We consider both transverse electric (TE) and transverse magnetic (TM) like optical modes in a 220nm thick Si guiding layer with varying

waveguide widths and TiO_2 cladding thicknesses. Fig. 3.1(a) shows the Poynting vector of the TE mode of a 250nm wide hybrid TiO_2 - Si waveguide and temperature sensitivity of the resonance wavelength, when the TE mode is in resonance. Fig. 3.1(b) shows the same for the TM mode. Optical modes are simulated using a Finite Element Method based solver (COMSOL), assuming the thermo-optic coefficients mentioned previously. The refractive indices of TiO_2 was assumed to be 2.35 (measured using ellipsometry). Temperature sensitivity is characterized in terms of resonance wavelength change with temperature ($\frac{\partial \lambda_0}{\partial T} = \frac{\lambda_0}{n_g}\frac{\partial n_{eff}}{\partial T}$). It is important to note that this sensitivity is independent of device structure (ring resonators or photonic crystal cavitites) and depends only on modal confinement in Si. For both TE and TM polarizations, the resonance wavelength sensitivity is $\sim$ 0.1nm/K for modes strongly confined in Si, and without any TiO_2 cladding. This sensitivity decreases as the mode is delocalized into the TiO_2 cladding and the thickness of the TiO_2 cladding is increased. For achieving true athermal operation, the exact geometry of the Si waveguide and TiO_2 cladding thickness needs to be chosen very carefully. For TM mode of a 220nm thick silicon waveguide, any waveguide width will have a corresponding TiO_2 cladding thickness that would allow athermal operation. On the other hand, for the TE mode, if the waveguide is too wide such that the optical mode is strongly confined in Si, athermal operation will not be possible irrespective of TiO_2 cladding thickness.

3.2.2 Fabrication

The athermal ring resonators were fabricated on a 220nm thick silicon-on-insulator (SOI) device layer. The waveguides were patterned using electron

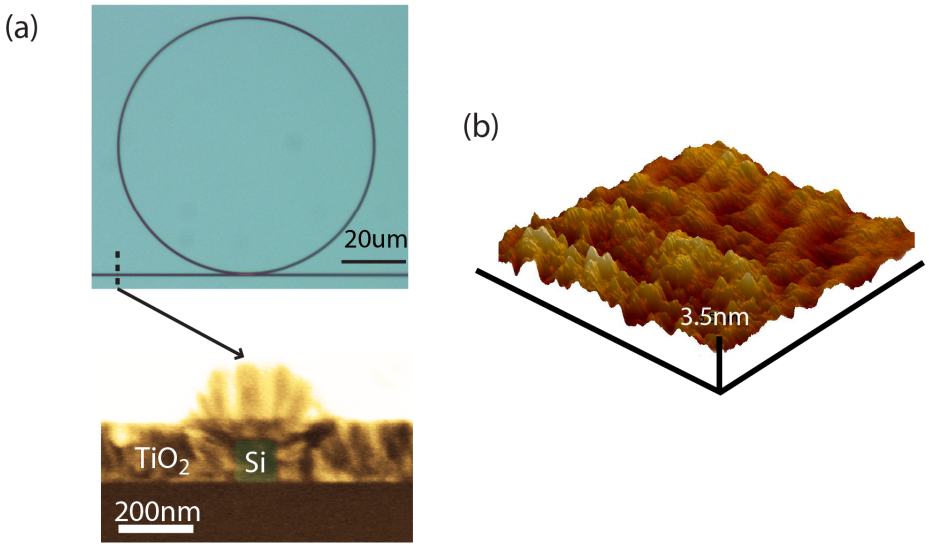

Figure 3.2: (a) TiO_2 cladded Si microring resonator. Inset shows a false colored SEM cross section of the waveguide. (b) AFM image of the TiO_2 surface.

beam lithography and etched in chlorine chemistry in an inductively coupled reactive ion etcher. Titanium oxide was deposited on top of the waveguides using reactive sputtering of a titanium target in O_2. The sputtering was performed at a pressure of 2×10^{-6} Torr and $2kW$ power. Sputtered TiO_2 films were characterized using a visible-near IR ellipsometer and Raman spectroscopy. Refractive index of ~ 2.35 was measured at near IR wavelengths. Raman spectrum of the sputtered sample shows no visible peaks, indicating the amorphous nature of the deposited TiO_2 film. AFM scan of the surface (Fig. 3.2(b)) indicates surfaces roughness below 2 nm RMS. Fig. 3.2(a) shows a microscope image of a fabricated Si ring resonators with TiO_2 cladding. Si waveguide width in the fabricated ring resonators was varied from 450nm to 150nm to observe the effect of mode delocalization on thermal sensitivity. Inset of Fig. 3.2(a) shows cross section of a waveguide with 150nm width and 200nm thick TiO_2 cladding.

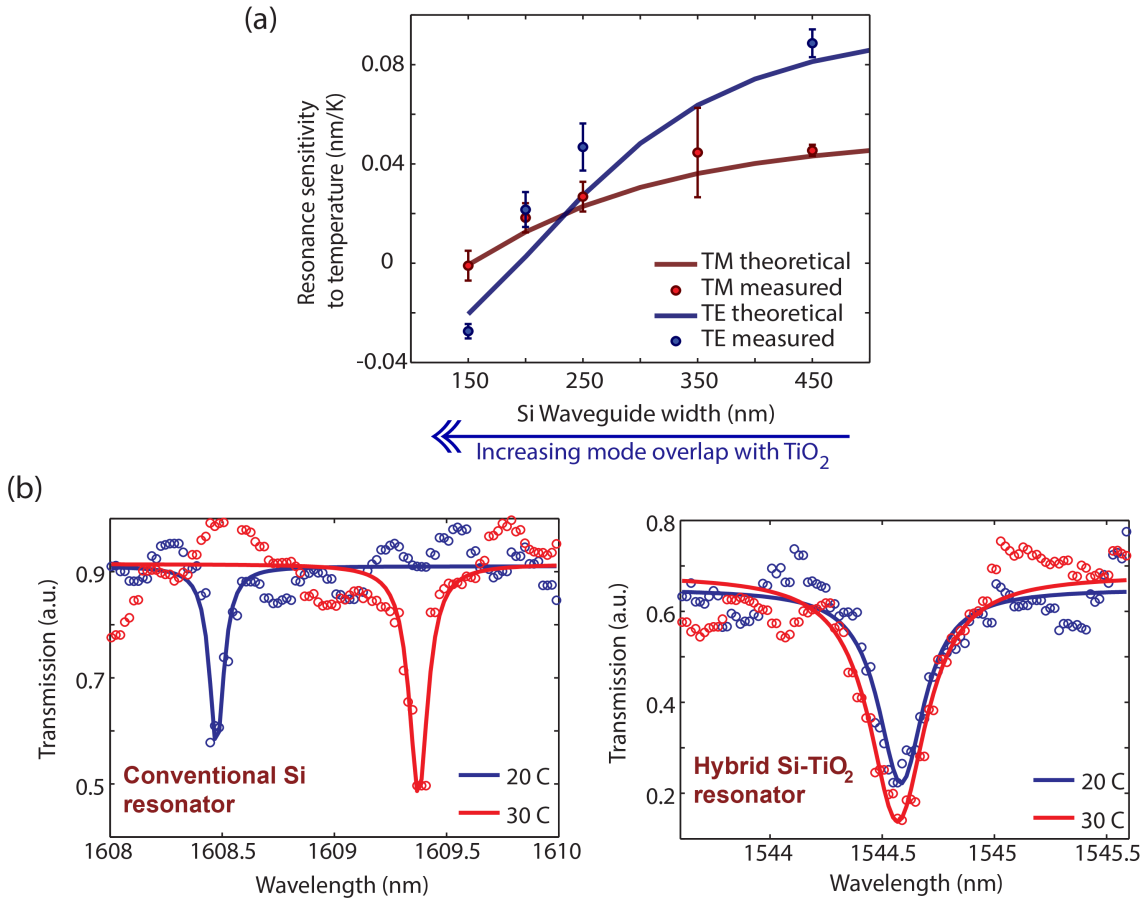

Figure 3.3: (a) Measured resonance sensitivity to temperature as a function of waveguide width, for TE and TM modes. Resonance sensitivity decreases significantly as mode is delocalized into TiO_2 cladding. Theoretical curves are obtained assuming 200nm thick TiO_2 layer. (b) Temperature dependence of the resonance for hybrid Si-TiO_2 resonator (athermal TM mode, right) compared to that of a conventional Si resonator (left).

3.2.3 Experiment

We demonstrate temperature insensitive operation of a Si microring resonator with TiO_2 overcladding. Fig. 3.3(a) shows the temperature sensitivity of resonance wavelength of the fabricated microring resonators, for different waveguide widths and polarizations. All of these resonators were fabricated on the same chip. The temperature sensitivity was measured by collecting spectra over 10 degrees, at intervals of 2 degrees, followed by a linear fit to resonance wave-

lenths. Error bar corresponds to uncertainty in the linear fit. Each waveguide width corresponds to a different confinement in the Si core. Measured data is compared against numerically calculated sensitivity assuming TiO_2 thickness of 200nm and $\lambda_0 = 1550nm$. For the case of TE polarization (Fig. 3.3(a) blue line), the temperature sensitivity is around $0.09nm/K$ when the mode is strongly confined in Si (450nm wide waveguide). However as the optical mode is delocalized more into TiO_2, temperature sensitivity decreases and becomes negative ($\sim -0.03nm/K$) for 150nm wide waveguide. For the case of TM polarization (Fig. 3.3(a) red line), the sensitivity is around $0.04nm/K$ for a strongly confined mode in Si and very close to zero for 150nm wide waveguide. Fig. 3.3(b) shows the corresponding athermal transmission spectrum compared to that of a resonator without any thermal compensation. Losses in the deposited TiO_2 was estimated to be around 16 dB/cm, by comparing change in quality factor of the resonances as a function of mode confinement in Si and TiO_2. This loss can be reduced significantly by improving the deposition and reducing scattering at Si – TiO_2 interface. Optical losses in similar material has been reported to be less than 3 dB/cm [51, 52].

We demonstrate error free operation of hybrid TiO_2 – Si microring resonator based optical filter over 35 degrees. The device used was similar to the one shown in Fig. 3.2(a) with an extra drop waveguide coupled to the ring. We transmitted $2^{31} - 1$ PRBS (pseudo random binary sequence) data at 5 Gbps through the device, centered at resonance wavelength, and varied the stage temperature (using a thermoelectric stage and temperature controller). The data was then sent to a commercial receiver (Picometrix PT15) and a bit error rate detector. Fig. 3.4(a) shows the bit error rate (BER) and corresponding eye diagrams for both the athermal ring resonator and a conventional Si resonator with similar

quality factor (where the temperature sensitivity is around 0.09 nm/K). For the conventional uncompensated device, BER becomes greater than 1E-9 after only 2 degrees (Fig. 3.4(a) blue line). For our athermal device, data transmission is close to error free over 35 degrees (Fig. 3.4(a) red line). This operating range should extend even further. Slight variations in BER is due to fluctuation in fiber to waveguide coupling with temperature. We also characterized the power penalty of the athermal optical filter for a $1\,^{\circ}$C fluctuation in temperature, and compared it to an uncompensated Si resonator based filter [22]. The $1\,^{\circ}$C temperature fluctuation was introduced by placing the sample on a temperature controlled stage and modulating the stage temperature at a rate of 1 Hz. This amount of temperature fluctuation is small enough such that the waveguide to fiber coupling is minimally perturbed, while modeling a realistic operating condition. The conventional resonator has a power penalty $> 1dB$, while the hybrid Si – TiO_2 resonator has power penalty $< 0.1dB$ (Fig. 3.4(b)).

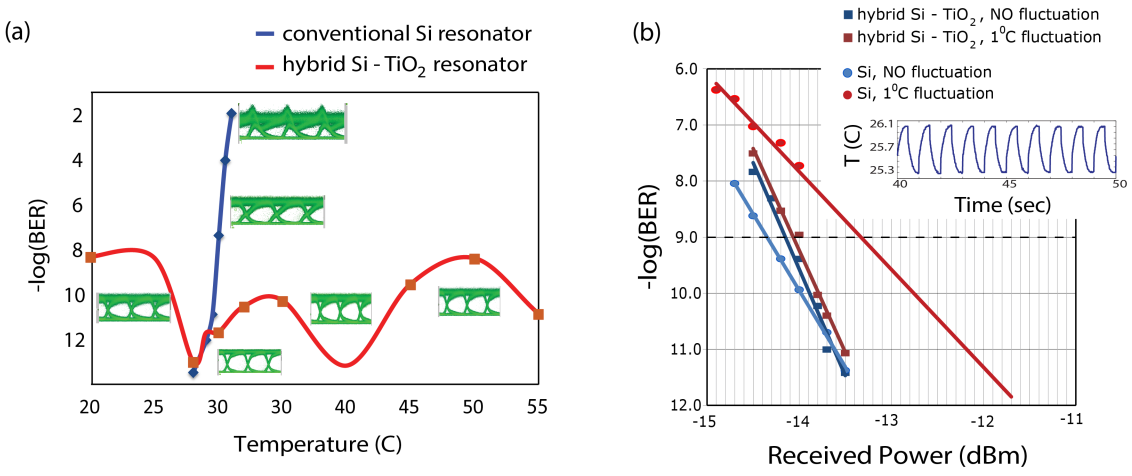

Figure 3.4: (a) BER vs. temperature for 5Gbps data transmission. (b) BER vs. received power for $1\,^{\circ}$C temperature fluctuation.

3.3 Discussion

We demonstrated a new technique for realizing athermal Si photonic devices using a TiO_2 over cladding. This approach is CMOS compatible, low loss and yields large temperature operating range. Simulations show that athermal operation is relatively insensitive to slight variations in TiO_2 thickness. Engineering the mode confinement is extremely critical for achieving athermal operation. It should be noted that this method is mainly applicable for resonators with radius $10\,\mu$m radius due to the need for a slightly delocalized mode. This method of passive athermalization can lead to practical monolithic integration of silicon photonic devices.

CHAPTER 4

CONTROLLING THERMO-OPTIC RESPONSE IN RESONATORS USING CANTILEVERS

In this chapter we demonstrate a novel method to control the thermo-optic sensitivity in nanophotonic devices by optically coupling them to bimaterial cantilevers. The cantilever can be designed to provide a negative thermal feedback to compensate for the positive thermo-optic shift the in waveguide core. The resultant devices are shown to athermal and can be designed to operate over a wide temperature range. Furthermore we discuss how this concept can be used to overcome the theoretical thermo-optic sensitivity limit of Si, and significantly increase the resolution of resonator based sensors and thermal imagers.

4.1 Introduction

Thermal sensitivity of optical microresonators can be a blessing or a curse depending on the application. Sensitivity of any photonic structure to ambient temperature fluctuations stems from the fact that increase in temperature increases the refractive index of all commonly used materials. This is called thermo-optic effect, which is a fundamental material property. Thermo-optic coefficient of Si (1.86×10^{-4}) [38] is almost an order of magnitude higher than that of most other commonly used photonic materials (SiO_2, Si_3N_4 etc.) [53]. This leads to a resonance sensitivity of ~ 0.1nm/K for an optical mode tightly confined in Si, irrespective of cavity design or dimension. This sensitivity is frequently exploited to tune the resonance wavelength or make sensitive detectors and thermal imagers. But this sensitivity makes Si photonic devices unstable in

a realistic platform, because of their extreme temperature sensitivity.

4.2 Lowering thermo-optic sensitivity

4.2.1 Motivation

Most of the approaches proposed to overcome the problem of temperature sensitivity in Si photonics are either power hungry, CMOS-incompatible or lead to delocalized optical modes. Temperature stabilization scheme using negative thermo-optic coefficient based polymers [18, 19] are not compatible with front-end CMOS processing and lead to delocalized optical modes. Active stabilization involving sensors and heaters [25, 27, 26, 29, 54, 22, 23] can be extremely power hungry, esp. since heaters need to be placed far away from the optical mode to avoid metal induced losses. Recently there have been novel demonstrations of thermal stabilization of a resonator by coupling it to a larger interferometer [41, 45, 55] which counteracts the thermally induced phase change in the resonator. This scheme is CMOS-compatible and passive, but needs extra footprint to accommodate the interferometer. Finally few recent works have used TiO_2 as a cladding material, which has a negative TO effect to counter the positive TO effect of Si [50, 56, 49, 57]. The drawback of this scheme is that the optical mode is delocalized and any further tuning or modulation becomes extremely power hungry.

We present a scheme that controls the thermo-optic response of the cavity independent of the cavity design or material thermo-optic coefficient. We achieve this by evanescent coupling between a bimaterial cantilever and optical

resonator. The properties of the cantilever can be designed to provide a negative thermal feedback to the cavity, which helps in thermal stabilization, or a positive thermal feedback which helps in increasing the temperature sensitivity. Cantilevers have previously been coupled to microresonators for achieving ultralow power wavelength tuning [58] and for decoupling optical and mechanical resonators in optomechanics [59, 60, 61, 62, 63].

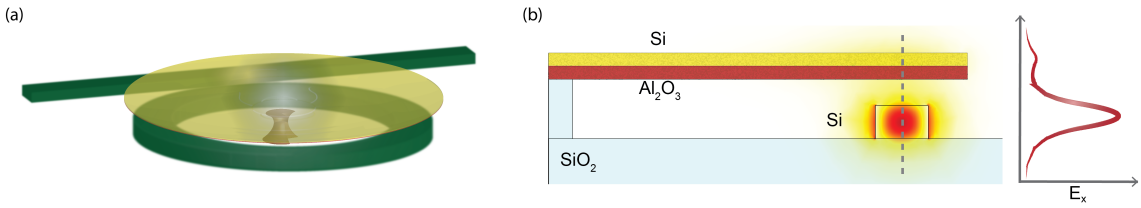

Figure 4.1: (a) Schematic of the proposed Smart Ring - a bimaterial cantilever is coupled to the waveguide. (b) Cross-section view of the proposed device and E-field along the dashed line.

4.2.2 Cantilever and Optical design

For a temperature stabilized Si resonator, temperature induced refractive index change in the waveguide core is counteracted by the optomechanical shift caused by temperature induced movement of the cantilever. The device should be compact, CMOS-compatible and has large modal confinement in Si. High confinement in Si is necessary for dense integration and low power tuning (thermo-optic or electro-optic). The proposed device and cross-section schematic is shown in Fig. 4.1.

Thermo-mechanical response of the cantilever and optomechanical coupling

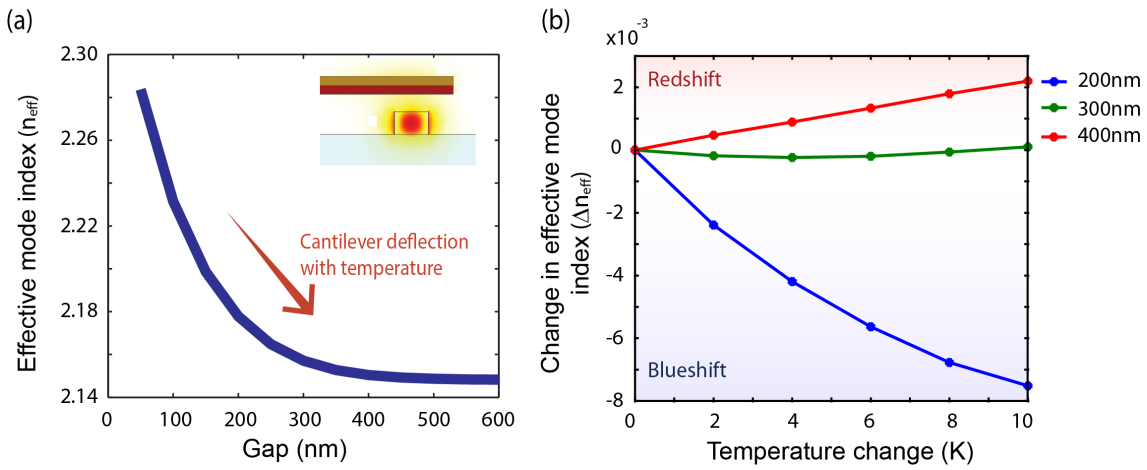

Figure 4.2: (a) Effective index of the coupled optical mode as a function of coupling gap. (b) Change in effective index of the optical mode as a function of temperature for different coupling gaps of the cantilever. When the cantilever is far away, change in effective index is positive and constant ($\sim 2 \times 10^{-4}$ K^{-1}). As the coupling gap is reduced, the cantilever interacts strongly with the optical mode and causes giant negative change. Somewhere in between, there is an optimum coupling gap which results in no change in mode n_{eff} with temperature.

is designed to exactly cancel out the thermo-optic drift of the ring. The bi-material cantilever is designed such that it bends upwards as temperature increases, thereby decreasing the effective index of the coupled mode and counteracting the thermo-optic effect. This is achieved by ensuring that the bottom layer of the cantilever has a higher thermal expansion coefficient (α) than the top layer. In our specific design we chose Al_2O_3 ($\alpha = 8 \times 10^{-6}$ K^{-1}) and Silicon ($\alpha = 3 \times 10^{-6}$ K^{-1}), each 100nm thick. As clear from the optical mode of this structure shown in Fig. 4.1(b), small fraction of the optical field is coupled to the cantilever on top. The strength of this coupling can be engineered by cantilever design – refractive indices of the layers, material thicknesses and the initial gap. When the cantilever is far away from the waveguide, the optical mode would be minimally perturbed by change in cantilever position. When the cantilever is close to the waveguide, small change in cantilever position would affect the optical mode significantly. Fig. 4.2(a) shows the strength of the optomechanical

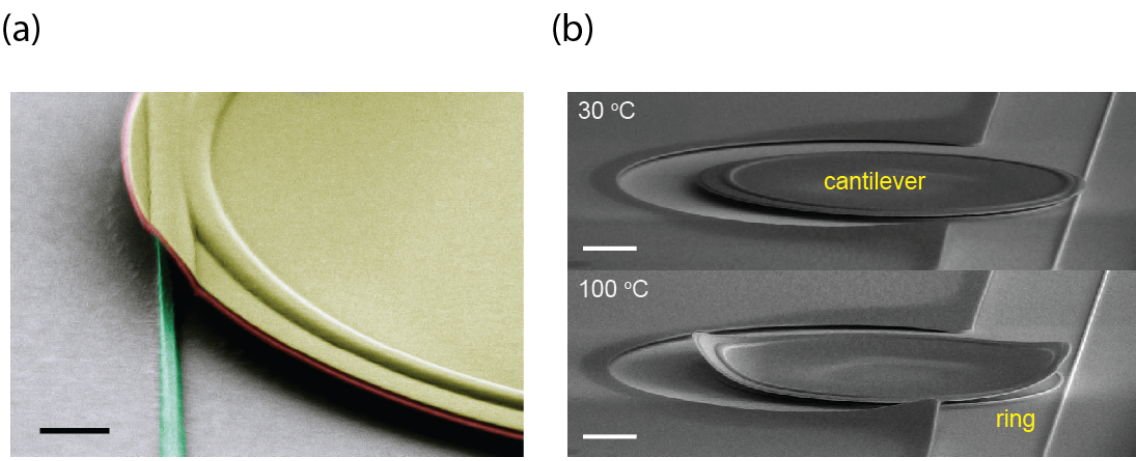

Figure 4.3: (a) False colored SEM image showing the coupling waveguide and the bimaterial cantilever. Scale bar is $2\,\mu$m. (b) Cantilever position at room temperature (above) and $100\,^{\circ}$C (below). Scale bar represents $20\,\mu$m.

coupling. Effective index (n_{eff}) of the coupled mode increases strongly as gap is reduced. For athermal operation we want to design the coupling so that it is just enough to cancel out the thermo-optic change of the optical mode. Fig. 4.2(b) shows the change in effective mode index of the TE mode ($n_{eff} \sim 2.27$) as a function of temperature for several different gaps. It is evident that when gap is large enough ($\geq 400nm$) n_{eff} increases with temperature at a rate of $\sim 2\times10^{-4}$ K^{-1}. At very small gaps ($\leq 250nm$), n_{eff} strongly decreases with temperature. At some intermediate gaps ($250-350nm$), change in n_{eff} is very minimal with change in temperature.

4.2.3 Fabrication

The devices were fabricated on a standard silicon–on–insulator (SOI) wafer with 240nm Si device layer and $3\,\mu$m buried oxide layer (BOX). Waveguides were defined using electron beam lithography and etched in a C_4F_8/ SF_6 / Ar/ O_2 chemistry. 10nm Si slab was left behind to isolate the buried oxide layer from

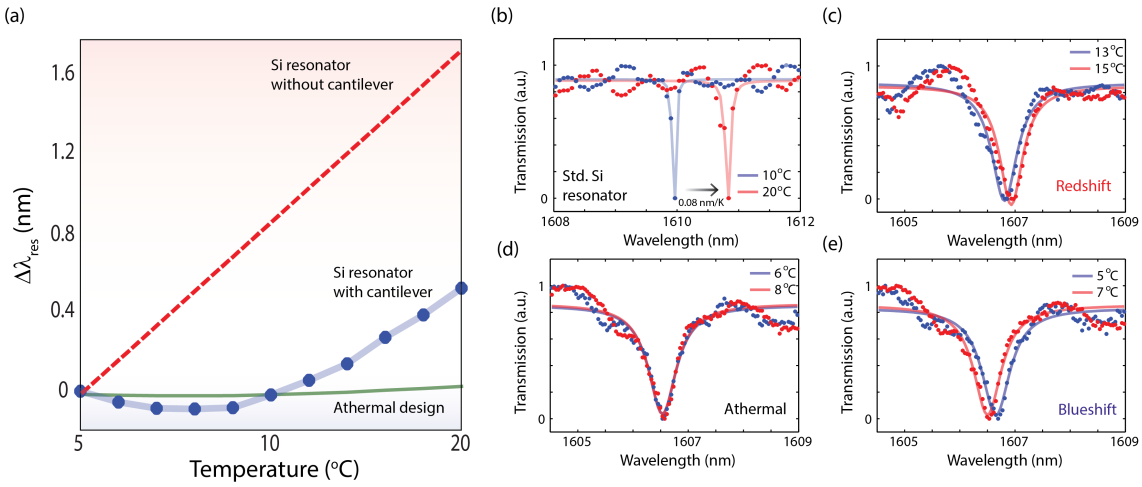

Figure 4.4: (a) Resonance sensitivity to temperature for Si resonator, with and without a cantilever (b) 0.08 nm/K redshift from standard Si resonator (c-e) Redshift, Athermal and Blueshift of resonances observed in resonator coupled to bimaterial cantilever.

subsequent release step. The device was cladded with 50nm Al_2O_3 deposited using Atomic Layer Deposition. This Al_2O_3 layer encapsulates the Si and further protects the BOX layer from the release step. 300nm SiO_2 was deposited using plasma enhanced chemical vapor deposition (PECVD) which will act as sacrificial layer during cantilever release step. Circular cantilevers made of 100nm thick Al_2O_3 and Si were deposited on top using electron beam evaporation and lift-off. Finally the cantilevers were released in HF–vapor based dry isotropic etch to obtain free standing bimaterial cantilevers on top of un-released Si ring resonators. The devices were placed on a thermo-electric module to control the temperature during testing.

4.2.4 Measurement

We show the capability of athermal operation over 14 degrees limited only by fabrication tolerance. Fig. 4.4(a) shows the change in resonance wavelength of

the TM mode of a $40\,\mu$m radius ring resonator as a function of temperature. For comparison measured resonance sensitivity of a similar resonator without the cantilever is shown in red. Temperature sensitivity in cantilever coupled devices is significantly lower. Athermal operating range is around 14 degrees, where change in resonance in less than half its linewidth. In our devices, the cantilever bent up slightly due to residual stress changing the designed coupling gap. Accurate control of the coupling gap can extend the athermal operation over a much wider temperature range (shown by green line Fig. 4.4(a)).

We demonstrate that resonance sensitivity changes from conventional redshift to strong blueshift with temperature, as the cantilever interaction with the optical mode increases when it is brought closer to the waveguide. At temperatures of $10\,^{\circ}$C and above (Fig. 4.4(c)), the gap between the cantilever and the waveguide is large enough such that thermo-optic effect dominates and resonance redshifts with increase in temperature. As temperature is reduced, the cantilever moves closer to the waveguide such that thermo-optic effect is compensated by index change caused due to the mechanical deflection of the cantilever. This is the athermal operating regime (Fig. 4.4(d)). Further reduction in temperature brings the cantilever even closer to the waveguide and leads to overall increase in n_{eff}, optomechanical shift dominates causing blueshift of resonance wavelength (Fig. 4.4(e)). For comparison, Fig. 4.4(b) shows the spectrum of a similar Si resonator without a cantilever, as a function of temperature. It shows a constant redshift of $\sim$0.08nm/K, typical of silicon ring resonators.

4.3 Enhancing thermo-optic sensitivity

4.3.1 Motivation

Si based microresonators hold great promise as temperature sensors [64, 65] and thermal/ IR detectors [66, 67] because of their small footprint and better noise performance; however they are limited in their sensitivity by the thermo-optic coefficient of Si, which is a fundamental material constant. Such high-Q resonators have been used as temperature sensors in various forms. Recent works have also investigated the use of these high-Q resonators for thermal imaging in mid-IR/ far-IR spectrum. Photonic elements are expected to have smaller response times and much better noise characteristics than current thermal detectors, since they do not suffer from Johnson noise. Reponsitivity of such detectors can be expressed as $\frac{\Delta S}{S \cdot P} = -\frac{\epsilon Q}{nG}\frac{\partial n}{\partial T}$ where ΔS is fractional change in signal S for incident power P, ϵ is emissivity at sensing wavelength, Q is the quality factor at detection wavelength and G is the background thermal conductance [67]. Thermo-optic coefficient of the constituent material $\left(\frac{\partial n}{\partial T}\right)$ is one the limiting factors of photonic thermal detectors. Also, for IR detection, the material needs to be simultaneously low-loss at detection wavelength (for high Q) and highly absorbing at sensing wavelength (for high ϵ), which limits the material choice.

4.3.2 Design

A slight modification of the same scheme allows us to enhance the thermo-optic response of photonic structures based on this novel waveguide geometry and break the material thermo-optic limit of Si based devices. Schematic of such a

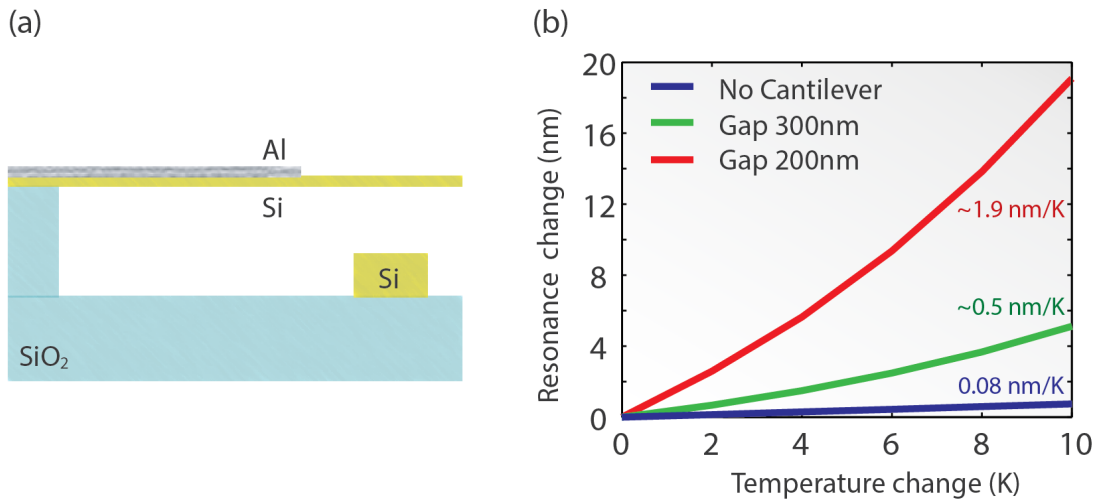

Figure 4.5: (a) Cantilever design for enhanced thermo-optic response. (b) Temperature sensitivity of cavity resonance wavelength for different coupling gaps. At a gap of 200nm, over two orders of magnitude enhancement in temperature sensitivity is expected.

device is shown in Fig. 4.5(a), where a Si microresonator is evanescently coupled to a bimaterial cantilever made of Si and Al. Unlike the athermal design, the cantilever in this embodiment is designed to bend down with increase in temperature. Al has much higher thermal expansion coefficients ($\alpha_{Al} = 23 \times 10^{-6}$ K^{-1}) than Si ($\alpha_{Si} = 3 \times 10^{-6}$ K^{-1}). As temperature increases, cantilever comes closer to the waveguide increasing the effective index of the coupled optical mode, same as thermo-optic effect. This positive feedback greatly enhances the overall temperature sensitivity. Fig. 4.5(b) shows the temperature sensitivity of the resonance wavelength for different coupling gaps. For a modest coupling gap of 200nm, the temperature sensitivity is ~1.9nm/K, which is an enhancement of over two orders of magnitude compared to the thermo-optic limit of Si (~0.1nm/K).

4.4 Discussion

In summary, we have presented a novel scheme to accurately control the thermo-optic sensitivity of optical resonators. We showed that this technique allows us to achieve athermal operation of any photonic structure (MZI, ring resonator, photonic crystal cavity) independent of cavity quality factor, cavity size or mode volume. Coupling gap and linearity of cantilever sensitivity to temperature can be optimized to yield a large athermal operating range. No extra footprint is required in the device layer to implement this scheme. With proper design, this scheme can significantly reduce the thermal budget in silicon photonic integration.

The same scheme can be slightly modified to increase the thermo-optic sensitivity, and break the material thermo-optic limit. This can boost the sensitivities of resonator based thermal sensors and IR detectors/ imagers. This is especially important for thermal/ IR imagers, where the sensitivity is limited by optical quality factor, thermo-optic sensitivity, material absorption and thermal isolation. The resonator can be independently optimized for quality factor, while the cantilever can be functionalized for high absorption and low thermal conductance. Coupled with small size and lower noise, these devices are expected to outperform the state-of-the-art bolometers.

CHAPTER 5

THERMAL RADIATION AT NANOSCALE

"God made the bulk; the surface was invented by the devil": Wolfgang Pauli

5.1 Introduction

Heat transfer at a distance through radiation, as opposed to through conduction, is usually thought of as a minuscule effect. It was recently demonstrated that heat transfer through radiation between two surfaces in the near field regime (i.e., at small enough length scales compared to the characteristic wavelength of thermal radiation which is $\sim 10\,\mu$m at 300K) can be extremely effective and can exceed the traditional heat transfer through radiation in the far field regime (i.e., blackbody radiation) by several orders of magnitude [68, 69, 70]. Near–field radiative heat transfer can be used to cool hotspots in thermally isolated nanostructures by coupling local thermal fields to evanescent surface electromagnetic modes of a nearby surface, and the rate of cooling would increase dramatically as the separation between the two surfaces reduces. We demonstrate radiative cooling of up to a few degrees and show that in principle this process can efficiently cool down localized hotspots by tens of degrees in sub-100 nm gaps.

Moreover heat transfer through radiative has some fundamental advantages over solid–state phonon based conduction. In solid–state bulk of the heat is carried by optical phonons with frequency grater than 1 THz or characteristic length scales less than 2nm [71]. Thermal radiation, on the other hand, has characteristic length scale of $\sim 10\,\mu$m, so that radiative spectrum can be shaped very easily using thin films or periodic structures. Hence radiative heat transfer can

offer an attractive platform to realize novel thermal thermal devices - like rectifiers, transistors, interferometers, cloaks etc. - and other electronic and photonic analogs. In the last section, I will describe experimental realization of one of these devices - a radiative thermal rectifier based on far–field radiation between SiO_2 and Au surfaces.

5.2 Near–field thermal radiation

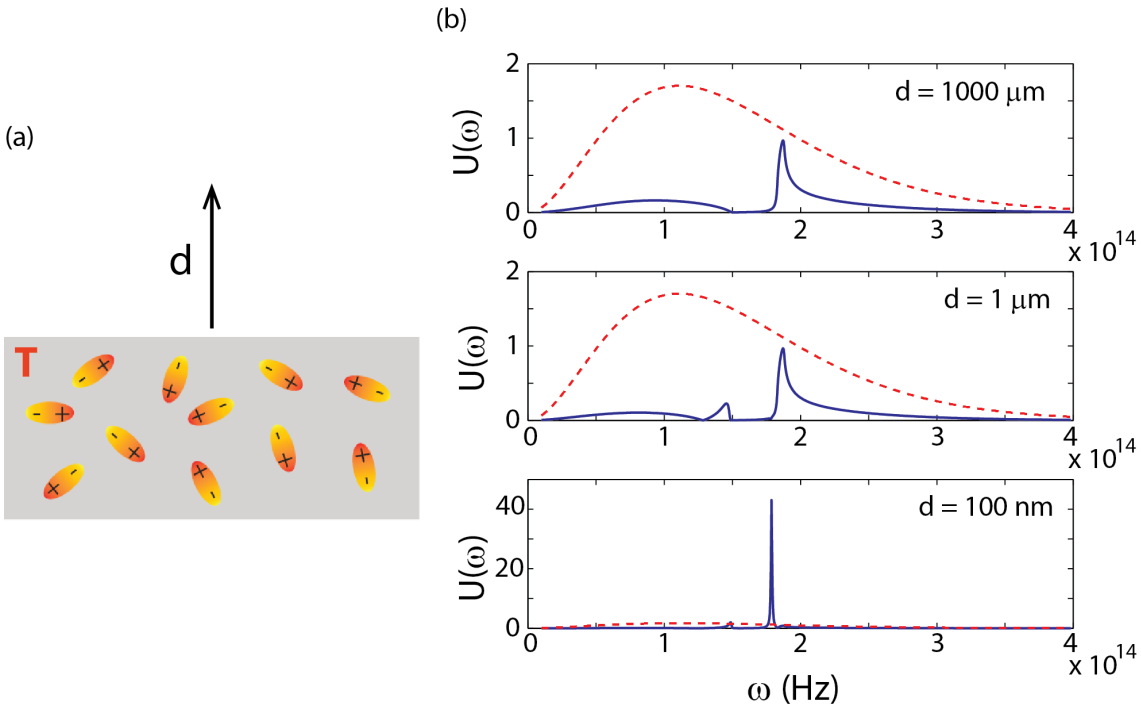

Figure 5.1: (a) Microscopic view of radiation. (b) EM DOS above a SiC surface at 300K. Red dotted shows the blackbody limit for a perfect absorber.

Macroscopically radiation is modeled using fluctuation electrodynamics, which is solving Maxwell's equations with a stochastic source [72]. Physically the picture is shown in Fig. 5.1(a), where fluctuations inside a material are modeled using microscopic dipoles. These dipoles refer to temperature induced charge fluctuations (polar optical phonons or free carriers) inside the material.

These microscopic fluctuations are correlated by dielectric constant of the material [72, 73, 74]. The dipoles emit radiation (as per fluctuation–dissipation theorem), and the surface permits some of this radiation to couple to the outside. So energy U at a distance d above a surface is proportional to the strength of these dipolar oscillations (which may have a resonance enhancement), temperature T and electromagnetic density of states (EM DOS) (DOS is usually limited by the surface). This is expressed in Eqn.(5.1)

$$U(\omega, d) = \Theta(\omega, T)\, DOS(\omega) \tag{5.1}$$

where $\Theta(\omega, T) = \dfrac{\hbar\omega}{exp\left(\dfrac{\hbar\omega}{kT}\right) - 1}$ is the energy per mode of a Planck oscillator. For a flat surface, EM DOS can be analytically calculated using Fresnel reflection and transmission coefficients, shown in Eqn.(5.2). It has two terms, one for modes that can escape out of the surface contributing to far–field radiation; and another term for reflected waves which have exponentially decaying energy density.

$$DOS(\omega, d) = \frac{\omega^2}{2\pi^2 c^3}\left(\int_0^{\frac{\omega}{c}} \frac{\beta d\beta}{k_0|\gamma|}\frac{(1-|r^s|^2)+(1-|r^p|^2)}{2} + \int_{\frac{\omega}{c}}^{\infty} \frac{4\beta^3 d\beta}{k_0^3|\gamma|}\frac{Im(r^s)+Im(r^p)}{2}e^{-2|\gamma|d}\right) \tag{5.2}$$

Here r^s and r^p refer to the Fresnel reflection coefficients for s and p polarized modes $\left(r^s = \dfrac{\gamma_0-\gamma}{\gamma_0+\gamma}, r^p = \dfrac{\epsilon\gamma_0-\gamma}{\epsilon\gamma_0+\gamma}\right)$, $\gamma^2 = \epsilon\left(\dfrac{\omega}{c}\right)^2 - \beta^2$ and $\gamma_0^2 = \left(\dfrac{\omega}{c}\right)^2 - \beta^2$ with β as in–plane wavevector. Note that in case of far–field radiation, only the first term in Eqn.(5.2) is present (since d is very large), while the second term can dominate very close to the surface.

Fig. 5.1(b) shows the energy density U (from Eqn.(5.1)) at different distances above a SiC surface at T=300K. For comparison the blackbody energy density (a

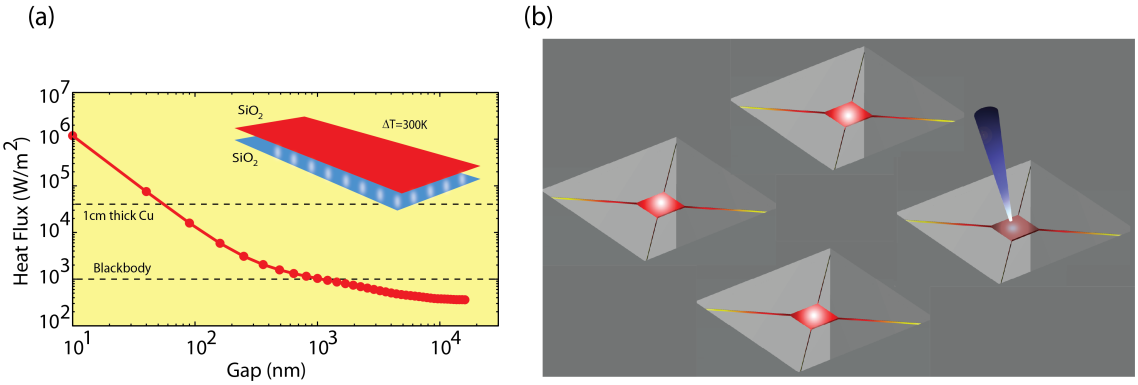

Figure 5.2: (a) Radiative heat flux between two SiO_2 surfaces (inset) held at temperatures of 300K (red surface) and 0K (blue surface), respectively. (b) Schematic of the experiment where one out of several isolated hotspots is cooled by radiative near-field coupling to a tip.

material which a is perfectly absorbing) is shown by the dotted red line. It can be seen that when d is large, the energy density of SiC is less than an ideal blackbody. This is the reason behind finite emissivity of real life materials. However, when d is very small there is a sharp peak in energy density of SiC which dwarfs the blackbody limit by orders of magnitude. The frequency of this absorption corresponds to optical phonon frequency where SiC has very strong absorption. Physically this resonant enhancement is due to evanescent waves which are bound to the surface. These waves originate due to resonant absorption in the material (optical phonons in case of SiC). Just like surface plasmons, they have large in-plane wavevectors (β) and exponentially decaying energy density outside the surface. These waves are called surface phonon polaritons (SPhP). SiC and SiO_2 exhibit strong excitation of these SPhP waves at room temperature. It is important to note that apart from these surface waves, "frustrated waves" can also lead to evanescent energy density outside a surface. which correspond to radiation that was generated in the bulk but reflected at the surface. These modes are present in all materials, however unlike SPhPs, there is no resonant enhancement.

Radiative heat transfer between two adjacent surfaces can be resonantly enhanced through the coupling of surface phonon polariton (SPhP) modes [75, 70, 73], hybrid surface modes that originate due to resonant coupling between the electromagnetic field and optical phonons of the material. Surface plasmons in doped Si [76, 77] or photonic crystal slabs [78] can lead to a similar effect. Here we choose to work with two SiO_2 surfaces since the SiO_2/air SPhP frequencies (3.5×10^{13} Hz & 1.5×10^{13} Hz) is close to the peak blackbody radiation frequency at room temperature (3.1×10^{13} Hz). Fig. 5.2(a) shows heat flux as a function of the gap between two such parallel SiO_2 surfaces. From Fig. 5.2(a), it can be seen that at gaps close to 10nm, the radiative heat flux is four orders of magnitude greater than blackbody radiation. In fact for plates of 1cm^2 surface area separated by a gap of 50nm, the radiative thermal conductance is the same as the solid-state conductance of 1cm^3 copper. Enhanced radiative heat transfer at nanoscale gaps has been measured recently in sphere-plane geometry by optical readout of a bi-material cantilever [79, 80, 81] and also in plane-plane geometry with gaps of up to a few microns [82].

5.3 Enhanced Radiative Cooling

Here we show cooling through radiation of a thermally isolated nanoscale structure by bringing it in proximity (but not in contact) with a probe connected to a thermal bath (see Fig. 5.2(b)). The nanostructure, acting as the hot spot, is a suspended SiO_2 membrane shown in Fig. 5.3. Thermal isolation is achieved by connecting the membrane to the substrate using thin spokes, resulting in low background conductance. The 100 µm by 50 µm membrane is made of SiO_2 that is 840nm thick, and is attached to the silicon substrate using thin spokes that are

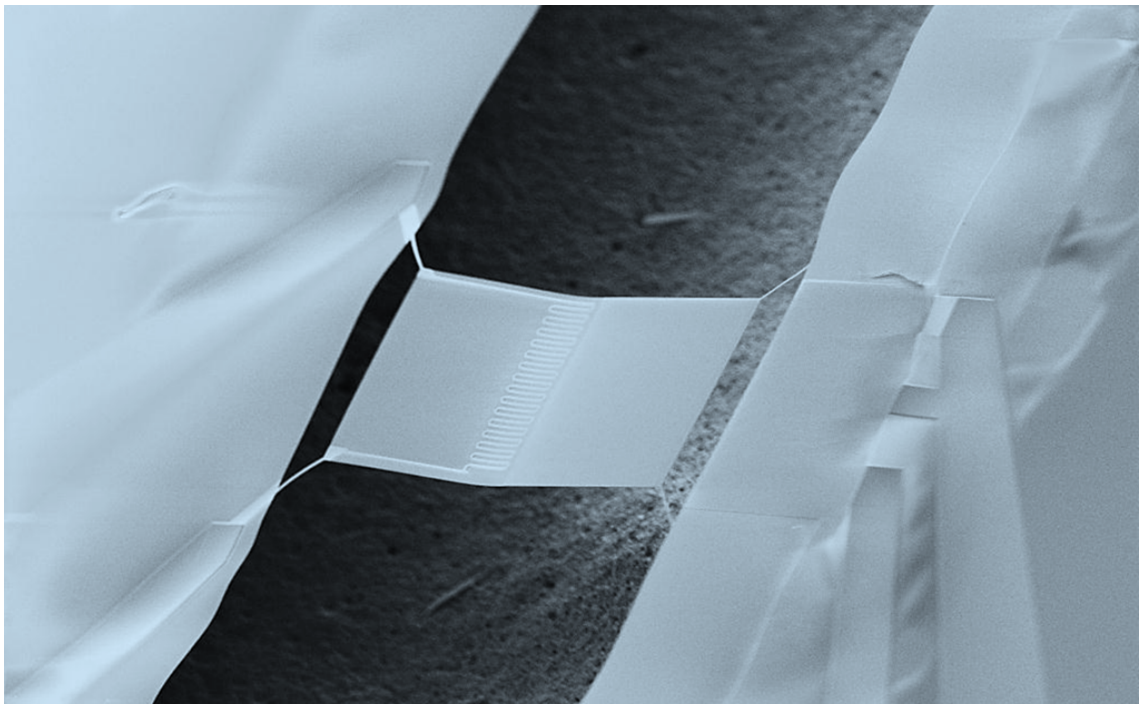

Figure 5.3: SEM image of the fabricated SiO_2 membrane, acting as local hotspot.

600nm wide and $30\,\mu$m long (Fig. 5.4(a)). XeF_2 based dry etch process was used to release the membrane over a $200\,\mu$m trench. The trench was deep enough to ensure that there is negligible spurious coupling of surface electromagnetic modes to the substrate. A 50nm thick Ni resistor is integrated on top of the membrane with connecting leads through two of the spokes. Al wires connect the resistor to pads which are then wire bonded to a package. A tungsten probe tip ($30\,\mu$m diameter), coated with $2\,\mu$m PECVD SiO_2, is connected to a heat sink and its background conductance is much higher than that of the membrane. Fig. 5.4(a) shows a top view SEM image of the suspended membrane with the probe tip in the inset. All experiments were performed under a vacuum of 10^{-5} torr, where thermal conduction through air is negligible.

To fabricate the suspended membranes, a Si wafer was oxidized to obtain 840nm SiO_2. The membrane structure was then patterned and etched in ICP

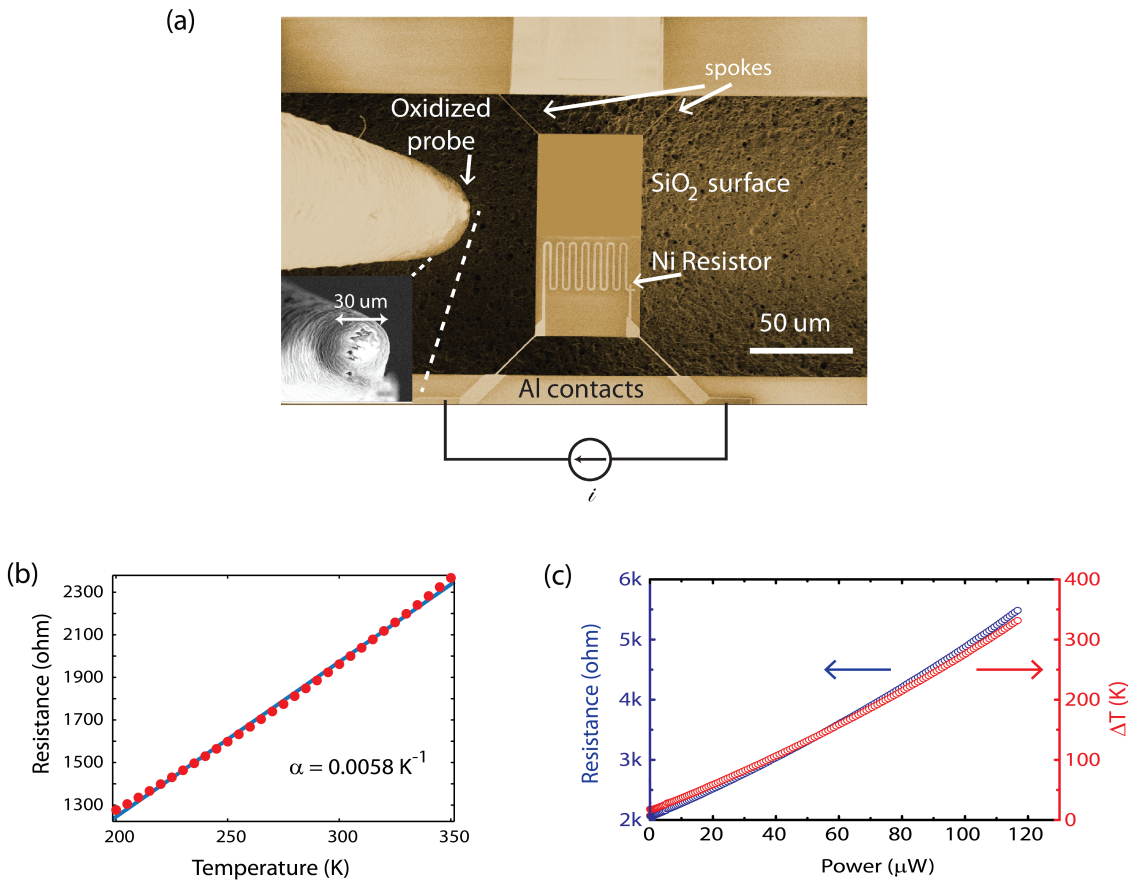

Figure 5.4: (a) Top view SEM image of the suspended SiO_2 membrane with integrated resistor and the probe close to it. Inset shows zoom-in of the SiO2 coated probe tip. (b) Resistance of the Ni resistor over a wide temperature range. The temperature coefficient of resistance was measured to be $0.0058K^{-1}$.(c) Change in resistance measured across the Ni resistor and corresponding temperature increase as power is dissipated in the resistor.

RIE. This was followed by deposition of 50nm of Ni and 500nm of Al using lift-off. Cr was used as an adhesive layer for both the metals. The wafer was then diced into pieces, and the membranes were released using a timed XeF_2 isotropic etch. Commercially available Signatone tungsten probes were uniformly coated with $2\,\mu m$ PECVD oxide deposited at $300\,^{\circ}C$. Probe resistance measurements confirmed a conformal oxide coating. The temperature coefficient of the Ni resistor on the membrane was measured over a wide temperature

range of 200-350K inside a Quantum Design PPMS (Physical Property Measurement System).

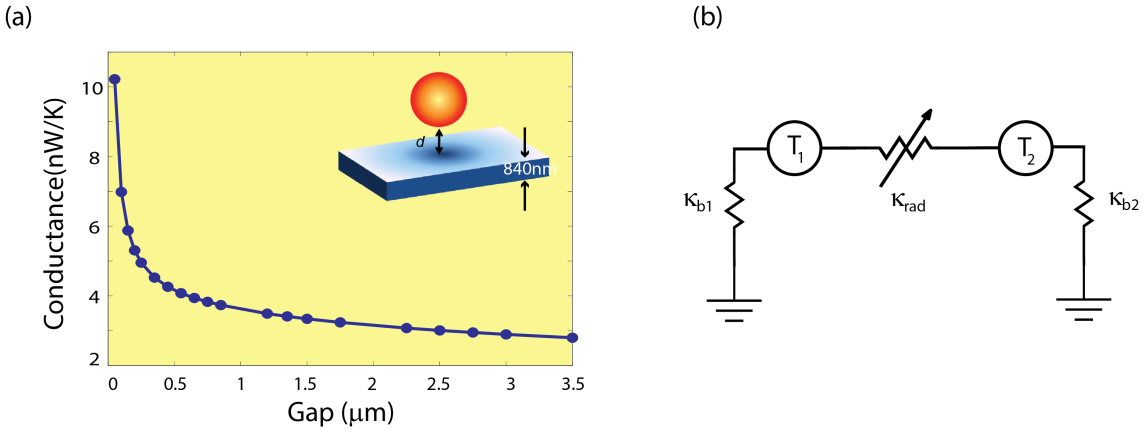

Figure 5.5: (a) Radiative thermal conductance between a $15\,\mu$m radius SiO_2 sphere and a 840nm thick SiO_2 surface (inset). (b) Equivalent heat circuit representation.

The probe tip is modelled as a sphere to simplify the analysis [83]. The radiative thermal conductance of the sphere-plane system can be defined as

$$\kappa_{rad}(d) = \frac{Q_{rad}(R,d)}{\Delta T} \tag{5.3}$$

where $Q_{rad}(R,d)$ is the radiative heat flux between a sphere of radius R and a semi-infinite plate separated by a vacuum gap d, and ΔT is the temperature difference between the two. We use a scattering matrix formalism to describe the sphere - plane system, following Otey and Fan [84]. The radiative thermal conductance between a sphere and a plane, both made of SiO_2, is shown in Fig. 5.5(a) for a sphere of $15\,\mu$m. The typical conductance for a gap of 100nm is less than 10nW/K and it increases as $1/d$ as gap reduces.

The other relevant thermal pathways are the background thermal conductance from the membrane to the surrounding through thin spokes and from the probe tip to its base. Both were calculated using the Finite Element Method and were estimated to be 100nW/K and 100μW/K for 600nm spoke width and

15 µm tip radius respectively. This also validates our assumption that background conductance of the probe tip is much higher than any other heat transfer channels, so the temperature of the probe tip can be assumed to be constant.

The equivalent heat circuit model is shown in Fig. 5.5(b). Here κ_{b1} is the thermal conductance between the suspended membrane and thermal bath (primarily dominated by the thin spokes) and κ_{b2} is the thermal conductance between the oxide coated probe surface and thermal bath (base of the probe). If power P_0 is dissipated in the membrane, the membrane temperature can be expressed as

$$T_0 = \frac{(\kappa_{rad} + \kappa_{b2})}{\kappa_{b1}\kappa_{b2} + \kappa_{rad}(\kappa_{b1} + \kappa_{b2})} P_0 + R.T. \tag{5.4}$$

where $R.T.$ is the room temperature. The radiative thermal conductance in our experiments is less than 10nW/K, while $\kappa_{b1} \sim 330nW/K$ and $\kappa_{b2} > 100\mu W/K$. Since$\kappa_{b2} >> \kappa_{b1}, rad$, the equation simplifies to

$$T_0 = \frac{P_0}{(\kappa_{rad} + \kappa_{b1})} + R.T. \tag{5.5}$$

Radiative cooling can then be quantified as

$$\Delta T = T_0(\kappa_{rad}) - T_0(\kappa_{rad} = 0) = \frac{\kappa_{rad}}{\kappa_{b1}(\kappa_{rad} + \kappa_{b1})} P_0 \tag{5.6}$$

This reduces to Eqn.(5.9) since $T_0 = \dfrac{P_0}{\kappa_{b1}}$. P_0 can be expressed as $I_0^2 R_0$ and the change in resistance as the temperature of the membrane changes due to radiative cooling can be expressed as

$$R(d) = \frac{R_0}{1 - \dfrac{\alpha I_0^2 R_0}{\kappa_{bck} + \kappa_{rad}}} \tag{5.7}$$

By using a constant current source and measuring $R(d)$, we get both the instantaneous temperature and power dissipated in the membrane.

Cooling was measured directly by small resistive thermometers integrated in the hotspots. Resistive thermometry can be extremely sensitive in detecting very small thermal fluxes, especially when used in platforms which are thermally isolated from the environment [85, 86, 87]. Thermal isolation also increases the near-field cooling sensitivity, so that radiative heat flux dominates over any other background thermalization pathway. Here Ni thermistors are used to heat the membrane relative to the tungsten tip to an initial temperature T_0 and then monitor the change in temperature of the membrane by monitoring the change in resistance. In order to relate resistance change to temperature change, the temperature sensitivity of the Ni resistor was calibrated beforehand by measuring the resistance over a range of 200-350 K, shown in Fig. 5.4(b). The temperature coefficient of resistance $\left(\alpha = \frac{1}{R_0}\frac{\partial R}{\partial T}\right)$ was measured to be $0.0058K^{-1}$. Since the thermal resistance of the suspended membrane is much lower than the spokes connecting it to its surrounding, it can be assumed that the temperature of the membrane is almost constant and follows that of the resistor. Very small electrical power is needed to heat up the membrane significantly because of its thermal isolation. Both the resistance and temperature increase of the resistor as a function of the applied DC power are shown in Fig. 5.4(c). From the plot one can see that a total power of $30\,\mu$W heats the resistor up by 80K, which corresponds to a background conductance of 360nW/K. As the probe is brought in proximity to the membrane, the resistance of the heater on the suspended membrane changes due to of the addition of an extra thermalization pathway.

The die containing the suspended membranes was wirebonded to a package and mounted on the stage on Zyvex S-100 nanomanipulator. The end of the oxide coated probe tip was scratched to remove oxide locally to provide good ther-

mal contact and attached to one of the arms of the nanomanipulator. The Zyvex system was placed inside a Zeiss Ultra SEM chamber, which was pumped down for an hour to reach vacuum level below 10^{-5} torr. The probe was accurately placed above the membrane by monitoring its motion through SEM, the electron beam was blanked during all the measurements to reduce noise. The cold resistance value was determined using a Keithley 4200 Semiconductor Characterization System using 10nA source current. The probe tip movement was automated using a closed loop Zyvex piezo controller. The probe tip was brought down in steps of 350nm with 1min interval between each step to let the system thermally stabilize.

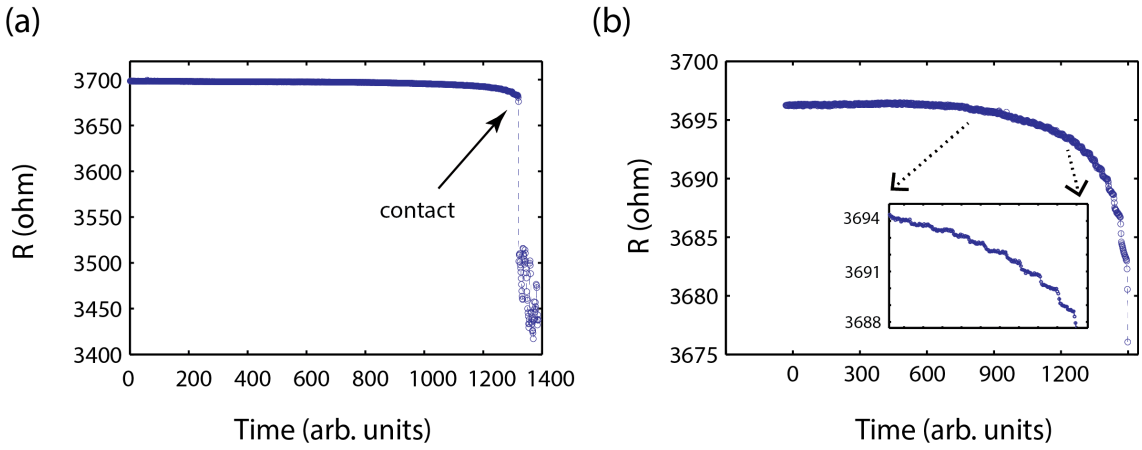

Figure 5.6: (a) Typical resistance curves measured with the contact point shown. (b) Zoom-in on the part just before contact showing gradual cooling due to radiative heat transfer. The inset shows a zoom in where the resistance steps are visible while the probe was held at constant gap.

As the piezo controller moves the probe closer to the membrane, a sudden drop in resistance signifies contact of the probe with the membrane. Since the rate at which the probe comes down vertically is known (measured in the SEM), the contact point is used to calibrate for the probe-membrane separation. Typical resistance vs time curves as are shown in Fig. 5.6(a) where the contact point is clearly visible. Fig. 5.6(b) shows the resistance change just before contact; the

gradual decrease is a signature of near-field radiative heat transfer. The probe is maintained at a fixed gap for 1 min to let the system thermally stabilize. The steps in the Fig. 5.6(b) inset correspond to a constant gap. These steps become more prominent at smaller gaps because of the large change in radiative heat flux for a small change in gap.

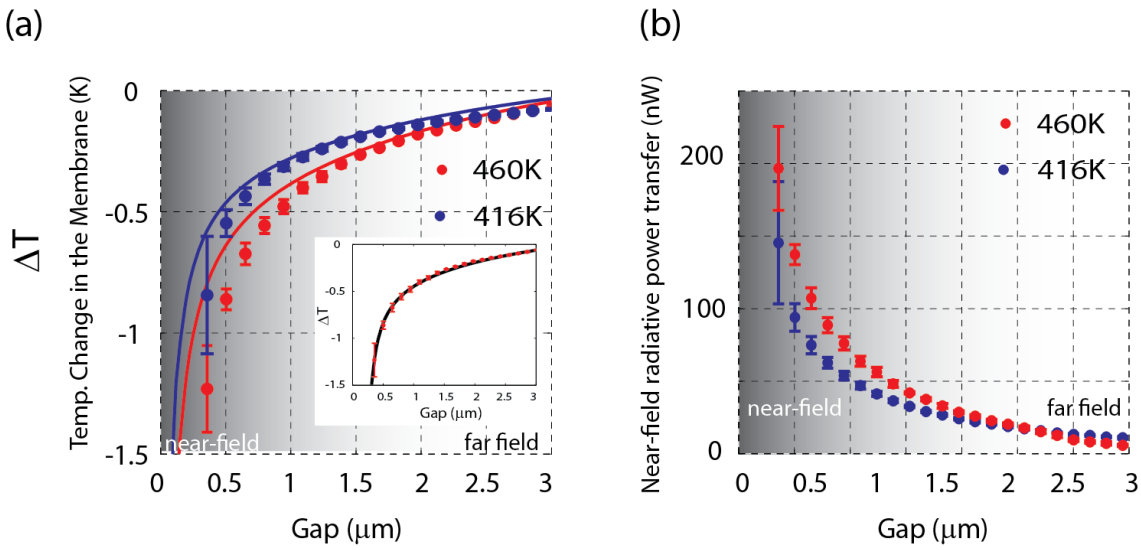

Figure 5.7: (a) Temperature drop due to radiative heat transfer as the probe is brought closer to the membrane, for two different initial membrane temperatures. Error bars represent the standard deviation of each measurement. Solid lines show theoretical prediction. Inset shows fitting of the measured data with model, yielding a gap uncertainty of 160nm. (b) Near-field power transfer between the membrane and probe as a function of separation.

We experimentally observe radiative cooling of up to 1.5K for a separation of 350nm between the SiO_2 surfaces. Radiative cooling is defined as the decrease in temperature of the membrane from its initial temperature due to radiative coupling.

$$\Delta T\left(d\right) = T\left(d\right) - T_0 \tag{5.8}$$

where T_0 is the membrane temperature when the probe is in the far-field and $T\left(d\right)$ is the membrane temperature when the probe is at a separation d. Power

transferred through near-field is given by $P_{rad}(d) = \kappa_{rad}(T(d) - R.T.)$, where $R.T.$ is room temperature. The measured temperature change of the membrane as a function of probe-membrane separation is shown in Fig. 5.7(a). It can be seen that when the probe is in the far-field region $(d > 2\mu m)$, the temperature of the membrane is relatively insensitive to small variations in the distance of the probe from the membrane. As the probe is brought closer to the membrane, the temperature drops due to the near-field coupling. From Fig. 5.7(a) it can be seen that when the membrane is heated to an initial temperature of 416K the temperature drop due to radiative cooling is around 0.8K. Increasing the temperature gradient leads to larger radiative heat transfer (Eqn.(5.9)), when the initial temperature is increased to 460K (up to 160 degrees above room temperature) the radiative temperature drop increases to 1.5K. The theoretically predicted trend of temperature decrease is shown in solid lines. It agrees well with the measured data, along with a constant offset. This offset is due to uncertainty in gap measurement, which is explained below. Following Eqn.(5.8), cooling of the membrane due to radiative coupling can be expressed as

$$\Delta T(d + \delta) = \frac{\kappa_{rad}(d)}{\kappa_{rad}(d) + \kappa_{bck}}(T_0 - R.T.) \tag{5.9}$$

where κ_{bck} is the background thermal conductance. Background conductance here refers to all other channels (except near-field radiation) through which the membrane can lose heat and includes heat dissipation through the thin supporting spokes and far-field radiation. δ is introduced as a fitting parameter which gives an indication of the uncertainty in gap measurement. κ_{rad} was modelled using a sphere - plane configuration, assuming a 840nm SiO_2 slab and temperature difference used in the experiment [simulation details in Supplementary Information]. The resulting electromagnetic heat transfer was calculated numerically using scattering matrix analysis [84]. The far-field component of ra-

diation increases by $\sim 7\%$ as gap is reduced from 350nm to 3500nm. We have estimated this view-factor effect by calculating the absorption by the finite area of the membrane of far-field emission from the sphere. Measured data was fitted to the model using δ and κ_{bck} as fitting parameters. Fig. 5.7(a) inset shows the resulting fit, with $\delta = 160nm$ and $\kappa_{bck} = 340nW/K$. This value of background conductance agrees well with the expected value of 360nW/K (see Fig. 5.4(c), slope of P vs ΔT). We estimate the gap uncertainty to be relatively small - of the order of 160nm - and it has several contributing factors like roughness of the probe tip and slight curvature of the release oxide membrane.Note that the gap uncertainty δ, estimated to be 160nm, is much smaller than the range of gaps measured ($0.3 - 3.5\mu m$). From the measurements one can extract the contribution of near-field radiative heat transfer [see Supplementary Information]. The increase in the power transfer from the membrane to the probe tip as a function of gap is shown in Fig. 5.7(b) for various temperature gradients. One can clearly see the signature of enhanced radiative effect for distances below 3 microns.

The usual sphere-plate heat transfer calculation assumes infinite lateral dimensions for the membrane. The actual finite size has negligible effect on near-field evanescent contributions to the heat transfer. However, the view-factor for field radiation will change as the gap between the sphere and membrane is varied. We take this into account as follows. First, we calculate the (isotropic, unpolarized) far-field power emitted from the sphere, using fluctuational electrodynamics and Mie theory [88]. We then approximate the power transmitted into the plate, integrated over all angles that the membrane sees,

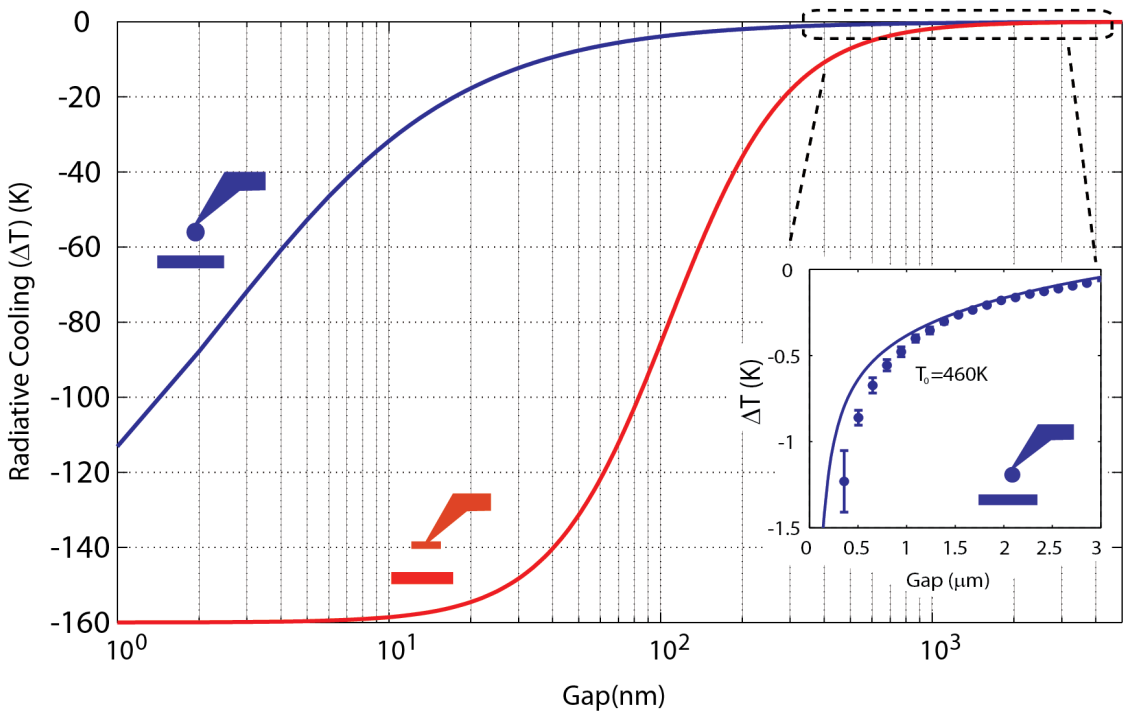

Figure 5.8: Estimated temperature reduction for a $100\,\mu\text{m} \times 50\,\mu\text{m}$ hotspot, using both spherical and planar probes.The spherical probe has a tip diameter of $30\,\mu\text{m}$. The hotspot has a background conductance of 350nW/K and is heated to an initial temperature of 160 degrees. All values are typical of the devices used in our experiments. Inset shows comparison of experimentally observed radiative cooling with the theoretical trend.

$$Q_{ff} = \int_0^{\infty} \mathrm{d}\omega \int_0^{\theta_{max}} \mathrm{d}\theta \sin(\theta)\, 2\pi a^2 \frac{1}{2} \left(1 - |r_{\perp}(\omega,\theta)|^2 + 1 - |r_{\parallel}(\omega,\theta)|^2\right) P(\omega) \tag{5.10}$$

where $r_{\perp}$ and $r_{\parallel}$ are the plane-wave reflection coefficients for the two polarizations of radiation, $\theta_{max} = \frac{\pi}{2} - arctan\left(\frac{a+d}{r_{membrane}}\right)$, a is the radius of the sphere, d is the gap between membrane and sphere, $r_{membrane} = 50\mu m$ is a suitably chosen effective radius of the membrane.

The measured trend of degree of radiative cooling efficiency agrees well with theoretical predictions and is limited mainly by the geometry of the probe used

here as well as the minimum separation that could be achieved in our setup. Fig. 5.8 shows the theoretical temperature decrease of the SiO_2 membrane due to radiative cooling when another surface is brought closer; assuming either a spherical probe with $30\,\mu$m tip diameter (similar to the one used in our experiments) [83] or another a parallel SiO_2 surface as a probe. The membrane dimension was assumed to be $100\,\mu$m by $50\,\mu$m, same as the one used in our experiments. The background conductance was assumed to be 350nW/K which is close to the measured background in our structures. In the simulations the membrane was heated to an initial temperature of 460K while the probe was at room temperature. The expected radiative power transfer is on the order of 5–$10\,\mu$W for a sphere-plane geometry with 160K temperature difference [see Supplementary Information, Fig. 5], which can be measured easily when it is of the same order as total electrical power dissipated in the resistor ($60\,\mu$W in our experiments). Our calculations are in good agreement with the experimental data (see Fig. 5.8 inset) and cooling by over 20 degrees should be achievable in the sub-50nm regime using our configuration. While the spherical probe can cool down the membrane by up to 30K at a gap of 10nm (blue curve), our calculations show that the near-field effect is even more pronounced when the probe is planar (red curve) and can reduce the temperature by over 100K at sub-100nm gaps.

5.3.1 Discussion

We demonstrated efficient cooling using near-field radiative heat transfer in a novel platform with temperature sensors integrated directly in thermally isolated hotspots. We measured a local temperature reduction of up to 1.5K, lim-

ited only by geometry and gap resolution, and showed theoretically that it should be possible to achieve very strong cooling in the near-field regime using a modified geometry. This method of thermal management using a non-contact approach could enable cooling when contact methods are not an option, such as in the case of micro-electro-mechanical devices and front-end of microelectronics. This novel platform can also pave the way towards exploring new aspects of radiative heat transfer such as the recently predicted thermal rectification [89, 90, 91] and negative thermal conductance [92].

5.4 Thermal Rectification based on Radiative heat transfer

5.4.1 Introduction

Thermal rectification is the property of directional heat flow – same transport channel acts as a conductor in one direction and insulator in the other direction. In other words the thermal conductivity of the channel has an inherent non–linearity, which introduces asymmetry based on direction of heat flow. This is schematically shown in Fig. 5.9.

This property is not present in most solid-state conduction based heat transfer mechanisms. This is mainly because thermal rectification, just like its electrical counterpart, requires an asymmetric junction or interface (analogous to p-n junction in electrical diode). Unfortunately solid state heat flow using phonons is extremely broadband, and hence impervious to junctions or interfaces. Theoretically rectification in solid–state has been explored extensively using non–linear lattice vibrations [93], non–linear electron gas dispersion in conductors

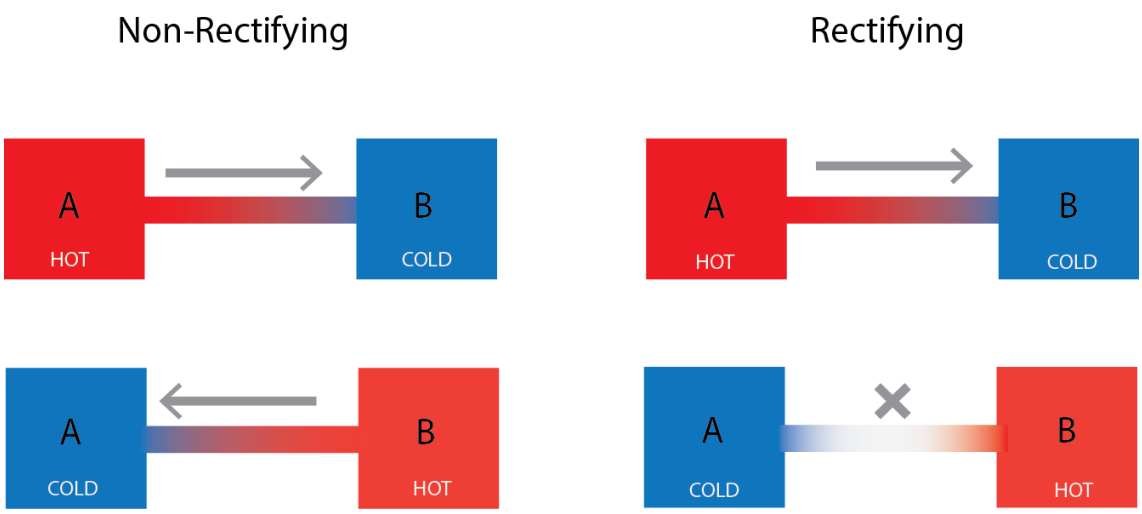

Figure 5.9: Concept of Thermal Rectification. The channel on the left is non-rectifying since amount of heat flow is independent of direction. The channel on right is rectifying since it allows heat flow in only one direction.

[94] and edge effects in graphene nano ribbons [95]. Experimental demonstrations of thermal rectification in solid state are limited to ∼7% in nanotubes [96] and ∼1% in graphene [97].

Thermal radiation between dissimilar surfaces can be used to design very efficient thermal rectifiers [89, 91, 98, 90]. This is because radiation spectrum can be engineered to be relatively narrowband (e.g. using thin films, periodic structures etc.) and material emissivities can be temperature dependent. Near–field thermal radiation, in certain material systems, can surpass blackbody limit by orders of magnitude and lead to thermal conductances close to solid-state systems. It also provides a very attractive platform for rectification because radiative density of states can be engineered to have extremely sharp temperature dependent resonances. This would help in designing rectifiers with large contrast ratio and high thermal conductivity.

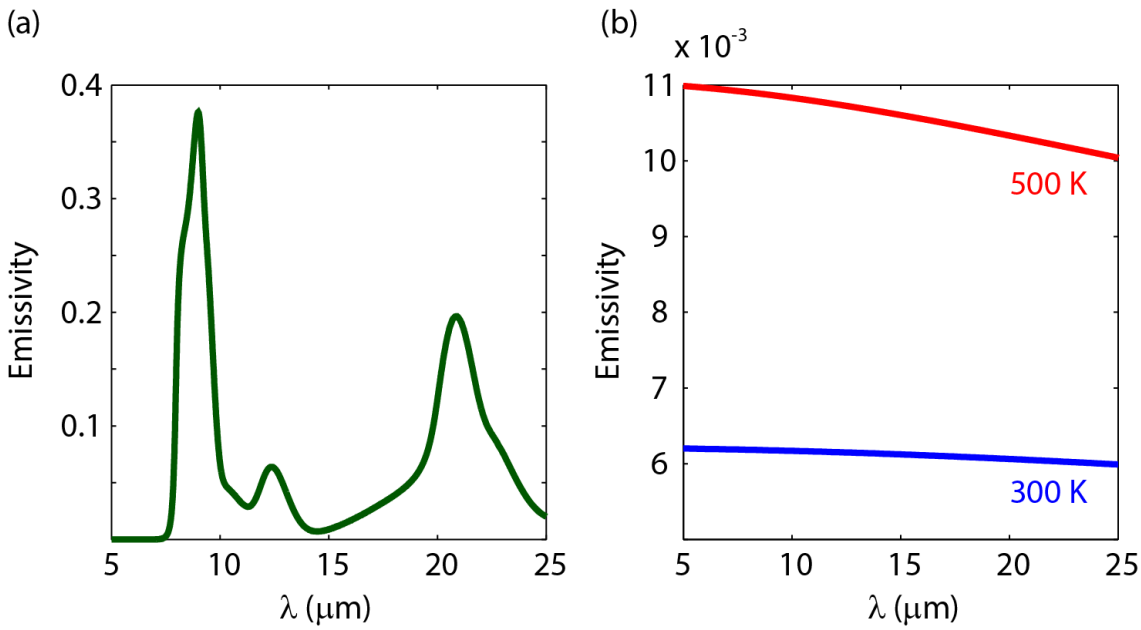

Figure 5.10: Emissivity of (a) 1 μm thick SiO_2 film and (b) 300nm thick Au film. Both are plotted for normal incidence.

5.4.2 Rectification using far–field radiation

Strong rectification can be observed in far–field thermal radiation using metals like gold (Au), whose emissivity has a strong dependence on temperature. The dielectric constant of Au can be modeled in Drude format as [53, 99, 91]

$$\epsilon_{Au}(\omega, T) = 1 - \frac{\omega_p^2}{\omega^2 + i\gamma(T)\omega} \tag{5.11}$$

where $\omega_p = 1.37 \times 10^{16}$ rad/s, $\gamma_0 = 7.31 \times 10^{13}$ rad/s and $\gamma(T) = \frac{\gamma_0 T}{300}$. Scattering rate in Au increases with temperature due to dominant electron-phonon scattering, which increases its emissivity [99, 100]. Fig. 5.10 shows the spectral emissivities of 1 μm thick SiO_2 film and 300nm Au film. Fig. 5.11(a) shows the simulated radiative heat transfer between Au and SiO_2 in forward and reverse biased scenarios. SiO_2 is chosen because of its high emissivity (∼0.8) and temperature independent optical properties [99]. It can be seen that net power transfer is much higher when Au is hotter, due to increase in absorption/ emis-

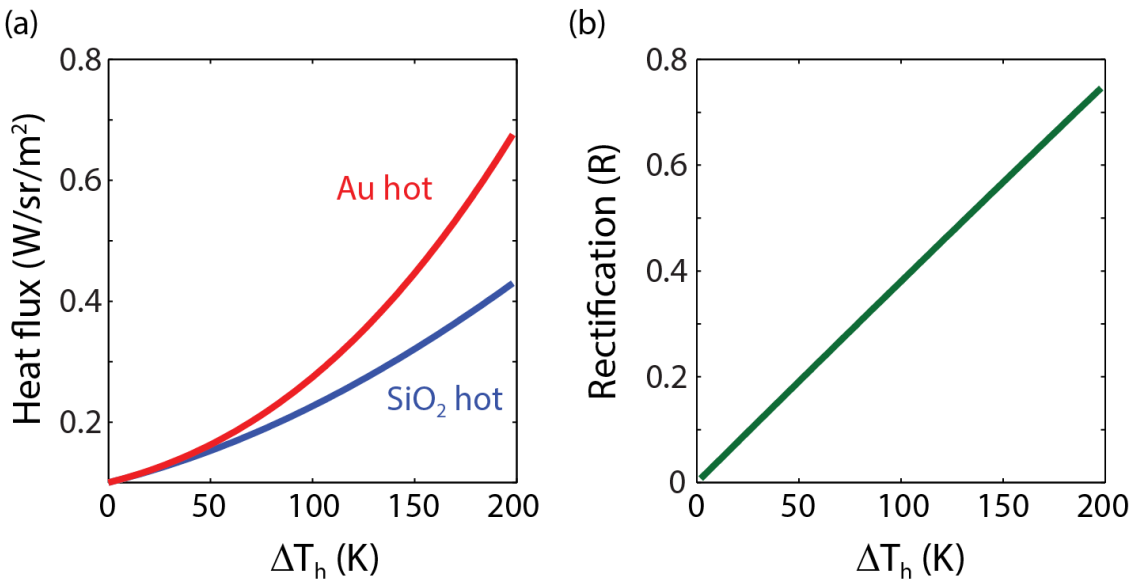

Figure 5.11: (a) Radiative heat fluxes as a function of temperature difference. (b) Rectification vs. temperature difference.

sion inside Au. Rectification is defined as $R = \frac{q_b - q_f}{q_f}$ where q_f is the net heat flux when SiO_2 is hot and q_b is the net heat flux when Au is hot. Fig. 5.11(b) shows the total rectification R, which approaches almost 80% for 200K temperature difference.

5.4.3 Probe Fabrication

We designed and fabricated custom probes, with large surface area and low background conductance (or high thermal sensitivity), for measurement of thermal rectification in SiO_2–Au surfaces. Radiative probes consist of a small membrane made of either SiO_2 or SiO_2 coated with Au, with integrated Ni resistors for heating/ sensing. Au leads are taken out through two narrow spokes, which connect the probes to the Si substrate. The probes were fabricated with different surface areas and shapes to help in optimizing measurement conditions. We

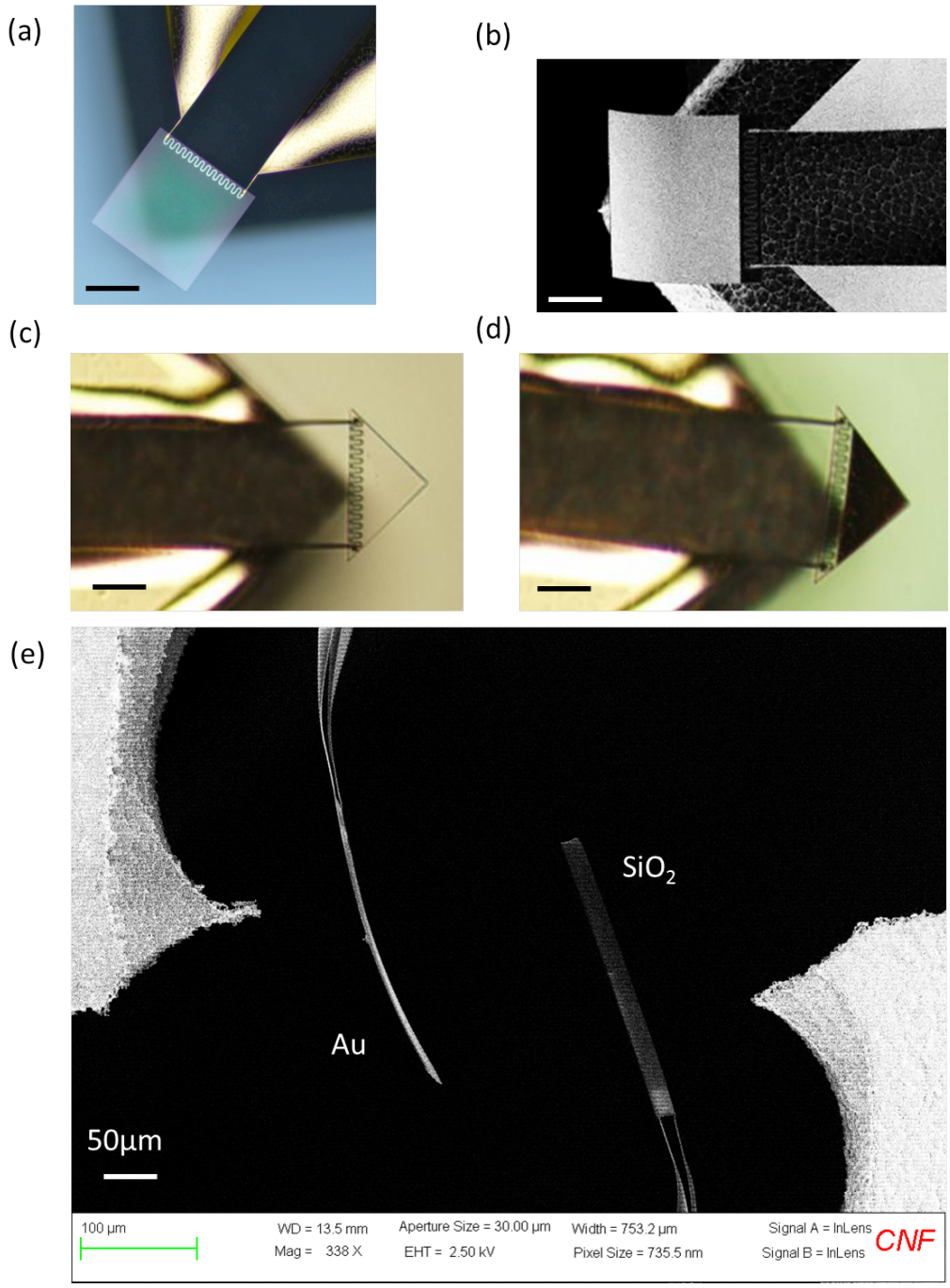

Figure 5.12: (a) Large SiO_2 probe. Scale bar is $50\,\mu m$. (b) Large Au probe. Scale bar is $50\,\mu m$. (c) Small SiO_2 probe. Scale bar is $20\,\mu m$. (d) Small Au probe. Scale bar is $20\,\mu m$. (e) Two large probes brought close to each other.

started with a Si wafer oxidized with $1\,\mu m$ SiO_2. Probe pattern was then defined using stepper lithography and SiO_2 was etched in a CHF_3/O_2 recipe. This was

followed by two lithography and metal lift–off steps to deposit 50nm Ni resistors and 300nm Au contact wires. Cr was used as adhesive layer in both cases. Au was also deposited on one of the probe surfaces, while the other probe surface was made of SiO_2. Each die in the wafer had one pair of SiO_2 and Au probe. The wafer was then coated with protective resist and diced to separate the probes into triangular shapes (Fig. 5.13(a)). Before the release step, resist was removed in an Acetone – IPA bath. The probes were then dehydrated at $250\,^{\circ}$C for $\sim$15min. This step is very important since any moisture left in the sample will cause Au to be attacked during the release step. The dehydrated probes were then released in XeF_2 based dry phase isotropic etch process with XeF_2 pressure of 3 Torr and N_2 pressure of 6 Torr. The released probes were then mounted on a custom probe holder and Cu wires were soldered for electrical measurements (Fig. 5.13(b)). Microscope images of the probes are shown in Fig. 5.12(a–d).

5.4.4 Experimental set–up

Zyvex S–100 nanomanipulator [101], operated inside a Zeiss Ultra Scanning Electron Microscope (SEM) chamber, was used for precise probe manipulation and placement. Fig. 5.13(c) shows the Zyvex probe holder and two radiative probes mounted on it along with electrical connections. The chamber is pumped to vacuum level of less than 10^{-5} Torr, so that conduction through air is negligible. Fig. 5.12(e) shows a typical experimental configuration, where two surfaces are brought in close proximity with their surfaces aligned.

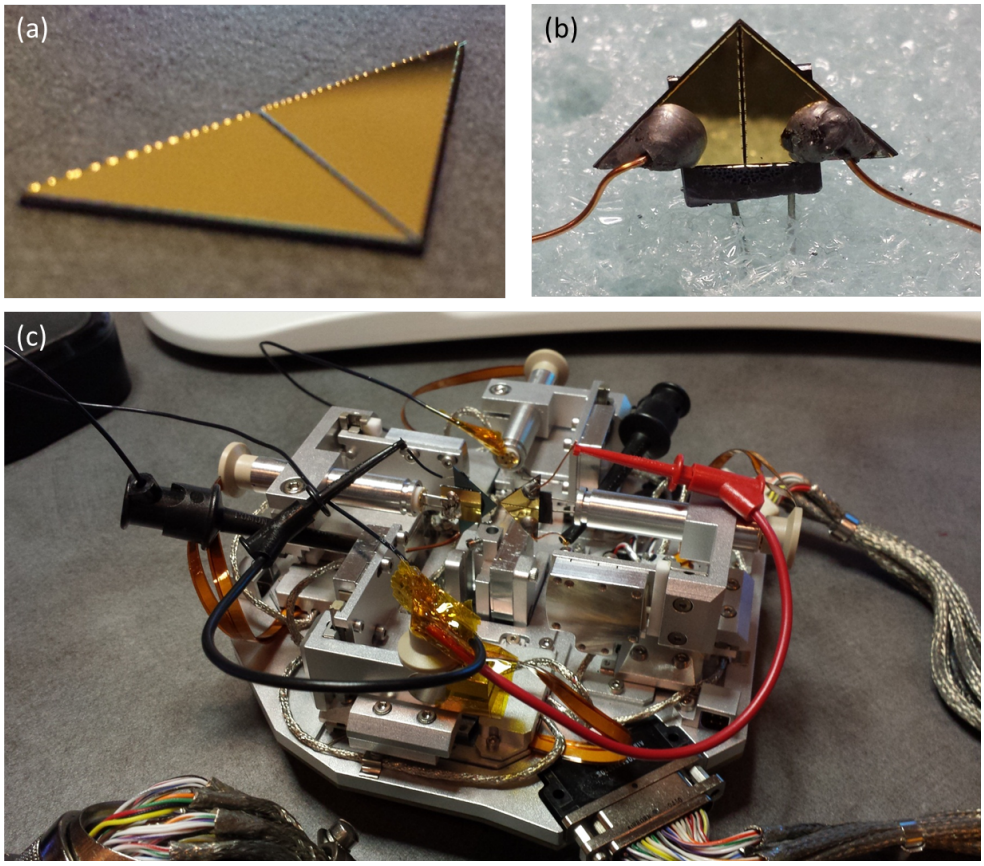

Figure 5.13: (a) Probe diced in triangular shape. (b) Probe with soldered wires and mounted on sample holder. (c) Both probes mounted on Zyvex probe holder, to be loaded into SEM chamber.

5.4.5 Measurement

To measure thermal rectification, one of the probes was heated and radiative heat flux was measured by sensing the temperature change in the other probe. This was followed by heating the other probe and measuring heat flux in the opposite direction. If P_h is the power dissipated in the heater, then temperature rise in the hot probe is $\Delta T_h = \frac{P_h}{\kappa_{bh}}$, where κ_{bh} is the background thermal conductance of the probe is being heated up. Temperature rise in the sensor probe is measured by passing a fixed sensing current I_s and measuring the change in voltage V_s. The relation between temperature changes in sensor and heater can

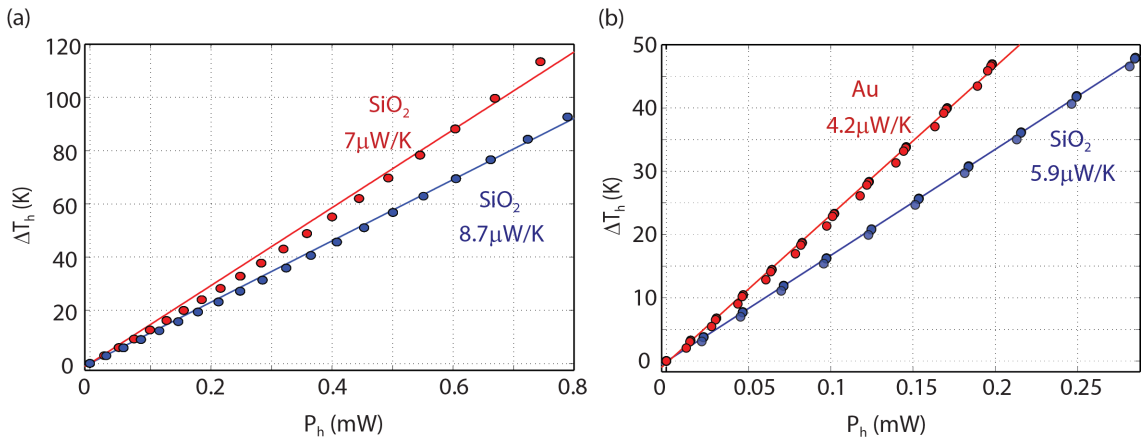

Figure 5.14: Background thermal conductance of the probes used in (a) SiO_2–SiO_2 baseline non-rectifying experiment. (b) SiO_2–Au rectification experiment.

be expressed as

$$\Delta T_s = \frac{\Delta V_s}{\alpha V_s} = \frac{\kappa_r^f}{\kappa_{bs}} \Delta T_h \tag{5.12}$$

where κ_r^f is the radiative conductance, κ_{bs} is the background thermal conductance of the sensor probe and α is the temperature coefficient of resistivity of Ni ($\alpha = 0.0058K^{-1}$). κ_r^b is similarly measured by reversing the heating and sensing probes. There is an assumption here that $\kappa_r^f, \kappa_r^b \ll \kappa_{bs}, \kappa_{bh}$, which is true because radiative heat flux is much smaller than heat lost through the spokes. Thermal rectification is defined as $R = \dfrac{\kappa_r^f - \kappa_r^b}{\kappa_r^b}$.

κ_r^f and κ_r^b are measured through slope of Q_s vs. ΔT_h curve in forward and backward direction respectively, where $Q_s = \kappa_{bs}\Delta T_s$ is the heat flux measured at the sensor. Hence it is important to characterize the background thermal conductance of the probes (κ_b) accurately (in principle, the ratio $\dfrac{\kappa_{bs}}{\kappa_{bh}}$ is important, not their exact numbers). Fig. 5.14(a,b) shows the background conductance of the probes used for both baseline and rectification measurements. κ_b is defined by the dimension of the connecting spokes and thickness of Au film on top of the spokes. It varies between 3–9 μW/K in our probes due to fabrication variations.

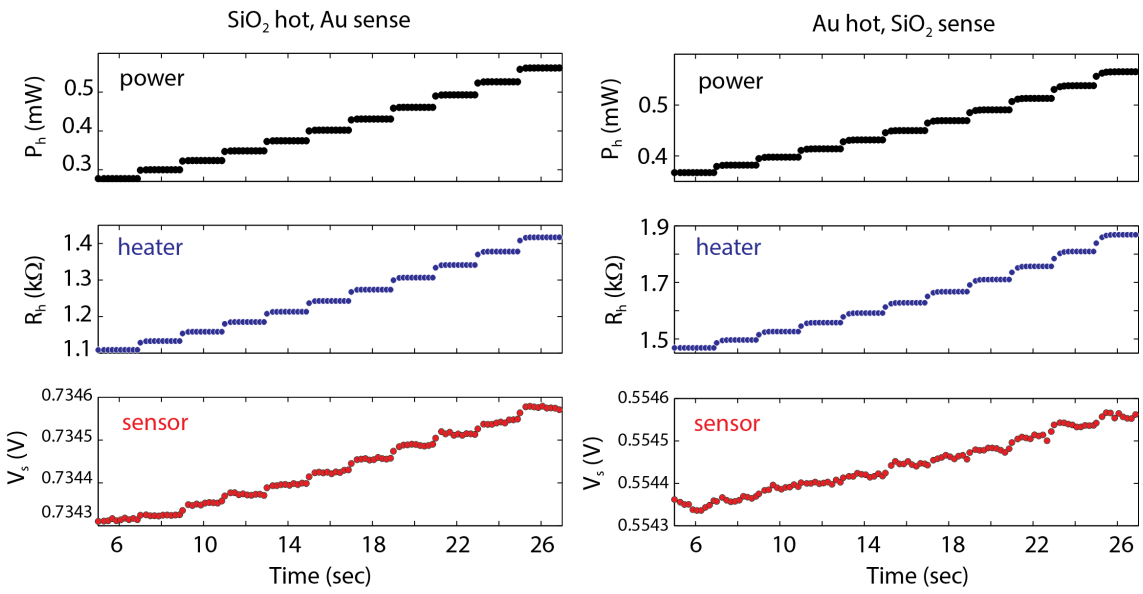

Figure 5.15: Typical experimental data when one probe is heated and temperature rise in other probe is sensed. I_s=0.5mA in both cases. (a) Forward case – SiO_2 probe is heated. (b) Backward case – Au probe is heated.

Fig. 5.15(a, b) show a typical measurement sequence where power applied to the heater is increased in small steps and corresponding voltage changes in the heater and sensor are recorded. For each measurement, the system is allowed to stabilize for a few seconds to reach thermal equilibrium. This data can then be analyzed to find κ_{bs}, κ_{bh}, ΔT_h from the heater response and ΔT_s from the sensor response.

We first do a baseline measurement where we prove non-rectifying behavior in SiO_2–SiO_2 coupled probes. Fig. 5.16(a) shows Q_s vs. ΔT_h measured in the non-rectifying case in forward and backward directions. They follow each over the entire temperature range. Similar non-rectifying behavior was also observed for different coupling gaps and when the probes were brought into contact. From these baseline experiments, we characterized our measurement protocol and sensitivity.

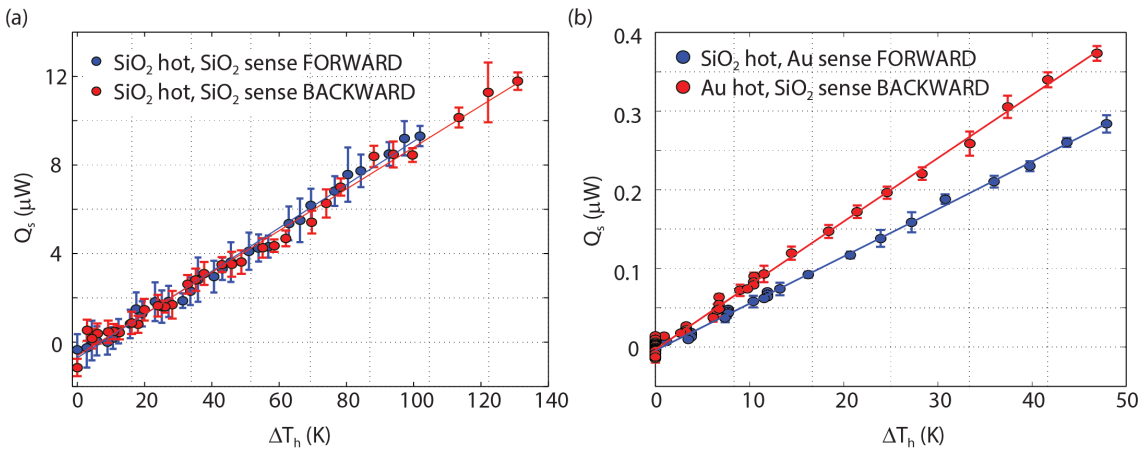

Figure 5.16: (a) Q_s vs. ΔT_h for SiO_2–SiO_2 probes. This was the baseline non-rectifying experiment.(b) Q_s vs. ΔT_h for SiO_2–Au probes. Rectification of $\sim$30% is observed.

We experimentally measure rectification of $\sim$30%$\pm$3% in SiO_2–Au coupled probe system. Fig. 5.16(b) shows Q_s vs. ΔT_h measured in forward and backward direction when SiO_2 and Au probes were brought in close proximity (Fig. 5.12(e)). Coupling gap is around $160\,\mu$m with three-quarter of the probe surfaces facing each other. There is a clear difference in radiative thermal conductance in forward and backward directions, with significantly more heat flux measured when Au probe is hotter. It is important to note that base temperature of both the probes was raised to 60K above room temperature for better measurement sensitivity. So temperature range in Fig. 5.16(b) corresponds to 360–410K. The measured rectification value of 30% is slightly lower than theoretical estimate of $\sim$40% at 410K. This deviation is attributed to deviation in properties of thermally evaporated Au from Drude model in Eq(5.11) and parasitic contribution of non-rectifying channels like base and tip of Au probe which are made of SiO_2.

Thermal rectification was further confirmed by a direct measurement of the temperature dependence of emissivities of Au and SiO_2. This was done by keep-

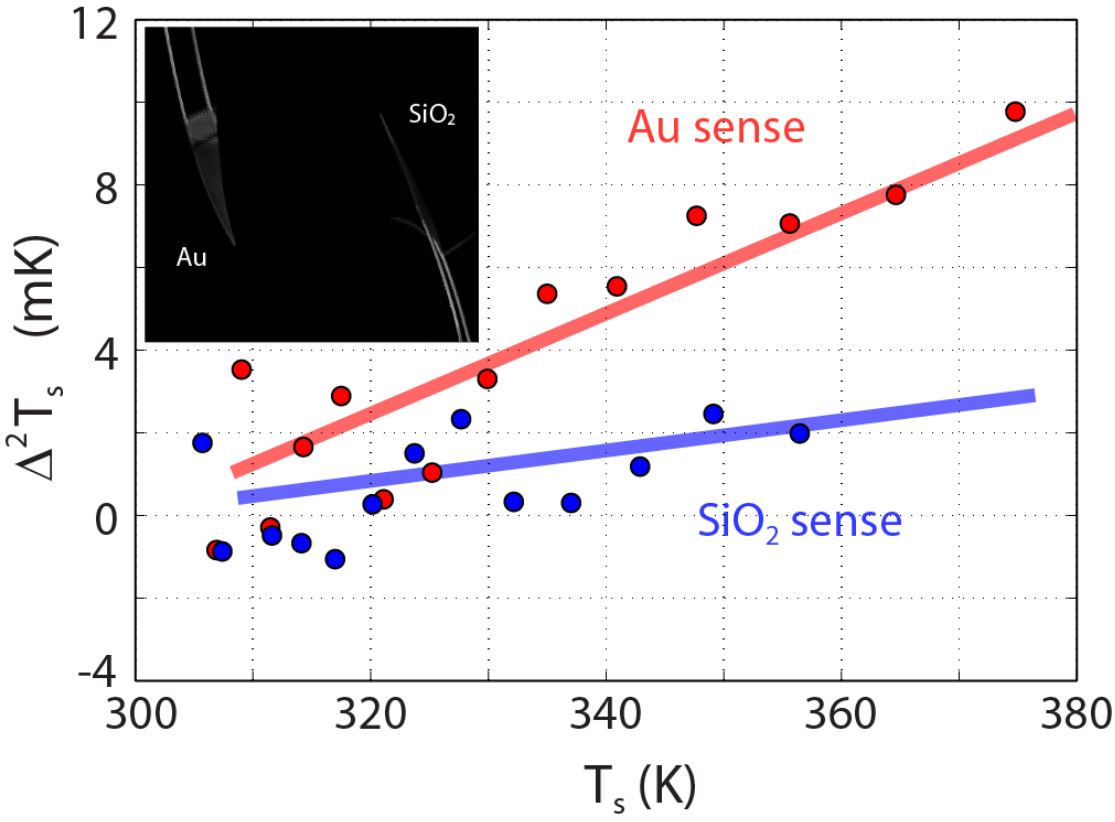

Figure 5.17: $\Delta^2 T_s$ vs. T_s for SiO_2 and Au probes measured by sweeping I_s. Change in emissivity of Au with temperature shows up as a linear change in $\Delta^2 T_s$ when Au probe is used as sensor. Inset shows the probe setup for the experiment.

ing the hot probe at a fixed temperature ($\Delta T_h = 100K$) and changing the temperature of the sensor probe (T_s) while recording change in sense temperature (ΔT_s). Temperature of the sensor probe was changed by sweeping the sensing current I_s. Relative change at the sensor $\Delta^2 T_s$ is defined as

$$\Delta^2 T_s = \Delta T_s - \Delta T_s\,(T_s = 300K) \propto \epsilon_h(T_h)\,(\epsilon_s(T_s) - \epsilon(T_s = 300K)) \qquad (5.13)$$

where ϵ_h and ϵ_s are emissivities of heater and sensor respectively. $\Delta^2 T_s$ should be zero if sensor emissivity is independent of temperature. As shown in Fig. 5.17, when Au is used as sensor, $\Delta^2 T_s$ increases linearly with T_s due to increase in emissivity of Au at higher temperature. SiO_2, on the other hand,

show almost no change in $\Delta^2 T_s$ with T_s since its emissivity is independent of temperature.

We compared our data with simulations and verified that measured rectification is due to change in radiative properties of Au and not due to small thermal deflection of the probes. Thermal deflection in SiO_2 probe with temperature is negligible, while deflection in Au probe, used in rectification measurement of Fig. 5.16(b), is around 10° over the temperature range. These deflections were measured through SEM and shown in Fig. 5.18(a,b). Deflection in Au probe is due to difference in thermal expansion coefficients of Au and SiO_2. First we verified that emissivities of thin-films of SiO_2 and Au do not change significantly over 15°. These simulations were performed using exact multilayer calculations and are shown in Fig. 5.20(a). Finally we verified that the small deflection of 10° contributes less than 3% change compared to ideal scenario of no deflection. This was done by simulating the structure in Fig. 5.18 in a finite element solver (COMSOL) for different deflections. Fig. 5.20(b) shows the change in ΔT_s (relative to no-deflection case) for different deflection angles. Deflection induced changes become relevant only for large angles greater than 30°. It is important to note that we chose to work at a large gap of $\sim 150\,\mu$m to minimize the effect of thermal deflection. Moreover, the data in Fig. 5.17 was obtained using small probes whose thermal deflections are negligible, as shown in Fig. 5.19.

5.4.6 Discussion

We reported the first ever experimental evidence of thermal rectification in a radiative channel. Observed rectification is significantly higher than other re-

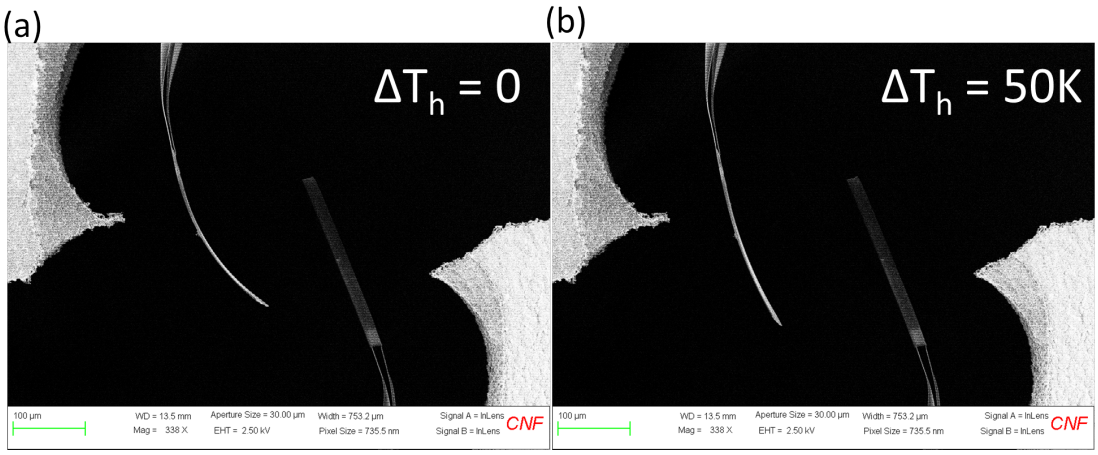

Figure 5.18: Thermal deflection of large Au probes. (a) Probe positions at beginning of the measurement. (b) Probes when heated up.

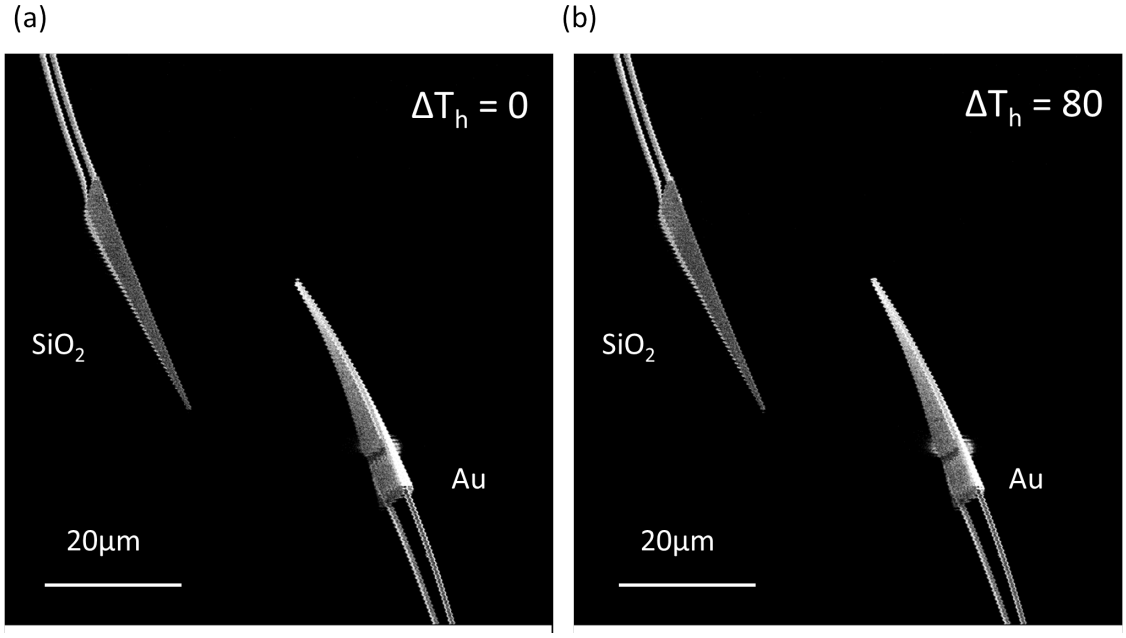

Figure 5.19: Thermal deflection of small Au probes. (a) Probe positions at beginning of the measurement. (b) Probes when heated up.

ported results in [96, 97]. In fact, radiative processes offer the potential to achieve very high contrast rectification, which is not possible in solid–state systems. Thermal spectrum and radiative modes can be engineered very easily using gratings and other periodic structures. Heat flux can be increased signifi-

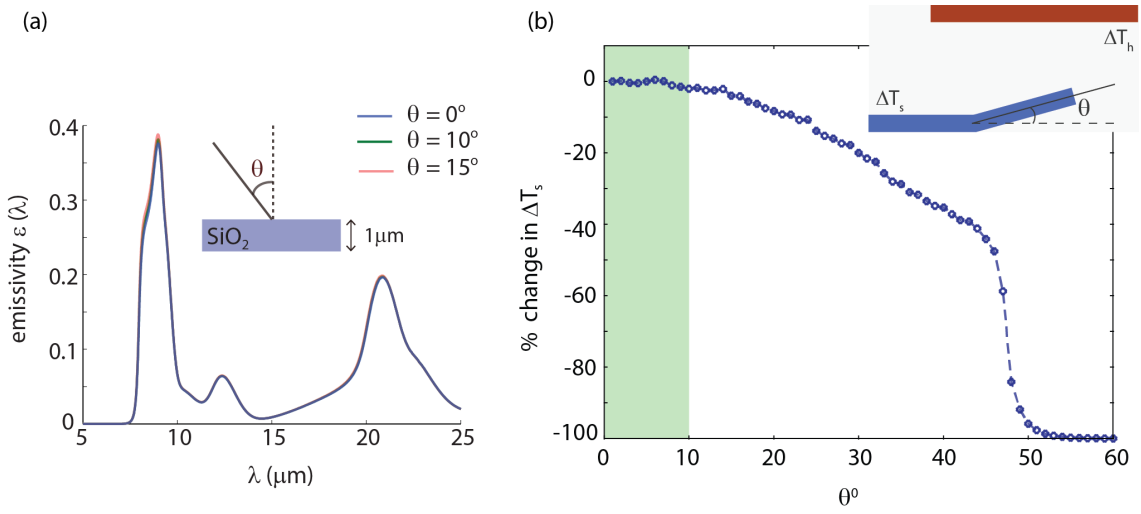

Figure 5.20: (a) Emissivity of SiO_2 for different angles upto 15^0. (b) Thermal deflection contribution to ΔT_s for different deflection angles. It is negligible for upto 15^0. Inset shows the geometry used for simulation.

cantly by using near-field thermal radiation. In the near–field, radiative modes can be further engineered using sub–wavelength structures which can lead to giant rectification without the need for different materials [98, 102]. This kind of flexibility makes nanophotonic control of thermal radiation very attractive for non–linear thermal transport devices like rectifiers and transistors.

CHAPTER 6

SUMMARY AND FUTURE WORK

In summary, we studied the interplay between temperature and optics in two different contexts. One hand we addressed the problem of temperature stabilization of optical devices, which is of paramount importance in scaling and chip scale integration of optical interconnect technology. All the athermal schemes proposed and demonstrated in this thesis are passive, CMOS-compatible and address a wide design space. On the other hand, we studied the role of photons in controlling heat transfer at nanoscale through radiation. We demonstrated enhanced cooling of nanostructures using near-field thermal radiation and measured thermal rectification in a radiative channel. These ideas might have significant importance in future thermal management and energy harvesting technologies like thermophotovoltaics.

Looking ahead, I think the athermal work will be adopted in some form to build larger scale integrated optical networks. The work on TiO_2 overcladding is especially promising because of its ease of implementation. However it remains to be seen how low power tuning and electro-optic modulation mechanisms can be incorporated along with TiO_2 cladding. Designing fabrication tolerant devices will go a long way in eliminating the need for post-fabrication wavelength tuning [103, 104, 105]. Making low power modulators would still be a challenge because of the mode delocalization. The all-Silicon interferometer based athermal scheme avoids these problems, as evident from the athermal electro-optic modulator demonstrated in this thesis. However those devices were relatively large and footprint scaling remains to be investigated. Integration of cantilever with optical devices opens up the possibility of simultane-

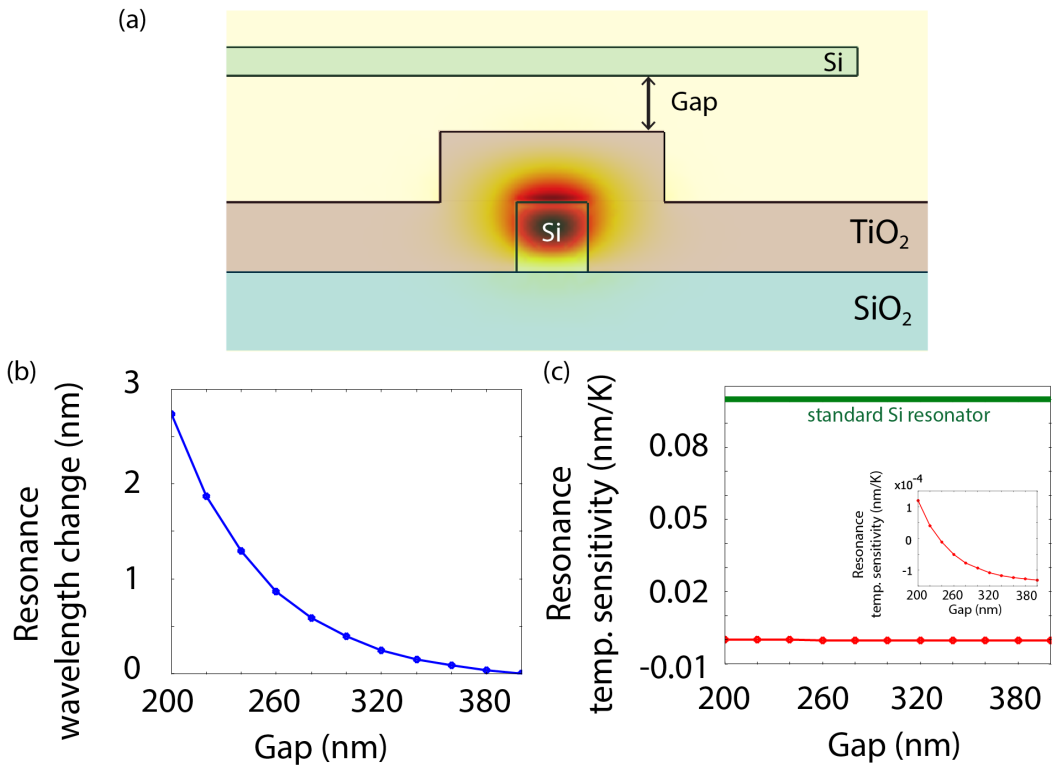

Figure 6.1: (a) Schematic of the waveguide with TiO_2 cladding and cantilever on top. Waveguide dimension is 233×250nm. TiO_2 is 250nm thick and the cantilever is 100nm thick. (b) Wavelength tuning of the resulting device. (c) Temperature sensitivity of the TM mode, compared to a standard Si resonator. Inset shows a zoomed in view.

ous ultralow power electrostatic tuning of the resonance wavelength and athermal operation using a separate bimaterial cantilever or thin TiO_2 overcladding. Fig. 6.1 demonstrates simulation results of this idea, where a tuning cantilever is coupled to a waveguide mode, which is inherently athermal due to TiO_2 cladding. However this fabrication is non-trivial and would need significant process development. The general idea is that combining the several different schemes described in this thesis, depending on the application, might help in mitigating some the major hurdles in silicon photonics.

The idea of coupling a bimaterial cantilever to a resonator might find application is designing ultra-sensitive uncooled thermal detectors. State-of-the

art detectors in mid/far IR include low bandgap semiconductors which are expensive and bolometers which suffer from Johnson noise and poor responsivity. Resonance enhanced optical detection and temperature sensitivity of a bimaterial cantilever can be combined to overcome the detectivity and cost limitations of detectors at longer wavelengths.

Tailoring radiative heat transfer using tools of nanophotonics has tremendous potential in revolutionizing the fields of thermal management and energy harvesting. The general belief is that heat is an unwanted byproduct which is hard to manipulate, because solid state heat transfer through phonons is extremely broadband. Radiative heat transfer through photons, on the other hand, can be designed to be narrowband by engineering the surface emissivity or surface density of states (e.g. surface waves, gratings, photonic crystals), and hence radiative heat transfer can be manipulated much more easily. Near–field radiative heat transfer increases the efficiency by several orders of magnitude, and can make radiation comparable to solid–state heat transfer mechanisms . Conversion efficiencies in Thermophotovoltaics can be significantly increased using near-field thermal radiation [73, 106, 107]. Moreover it can be used to demonstrate non-linear thermal transport processes like rectification [89, 90, 91], negative thermal conductance [92] etc., properties which are not present in conventional solid state heat transfer. The analogy of heat transport with electronic transport can be further extended [108]. Recent theoretical works are already talking about thermal switches [109] and transistors [110]. Experiments similar to [86, 111] can be performed to understand quantum of conductance in context of radiative heat transfer [108]. Extending these concepts to nanostructures is very important in chip-scale thermal management and energy conversion. Novel materials like vanadium dioxide (VO_2), aluminium zinc oxide (AZO) and

graphene can be studied for their radiative properties. VO_2 has very large thermal nonlinearity (insulator–metal phase transition) [112, 113] while graphene and AZO have low electronic densities which can lead to plasmonic control of IR radiation [114, 115, 116]. Furthermore hot cavities can be used to generate quasi-coherent light in mid-IR, where light sources are very rare. This can have significant impact on sensing and detection since many molecules have their vibrational modes in mid-IR frequency range. Nanophotonics provides an incredible toolset to manipulate heat and not let it go to waste.

BIBLIOGRAPHY

[1] D. A. B. Miller, "Rationale and challenges for optical interconnects to electronic chips," *Proceedings of the IEEE*, vol. 88, no. 6, pp. 728–749, 2000.

[2] A. Alduino and M. Paniccia, "Interconnects: Wiring electronics with light," *Nature Photonics*, vol. 1, no. 3, pp. 153–155, 2007.

[3] P. Dumon, W. Bogaerts, V. Wiaux, J. Wouters, S. Beckx, J. Van Campenhout, D. Taillaert, B. Luyssaert, P. Bienstman, D. Van Thourhout, *et al.*, "Low-loss soi photonic wires and ring resonators fabricated with deep uv lithography," *IEEE Photonics Technology Letters*, vol. 16, no. 5, pp. 1328–1330, 2004.

[4] U. Fischer, T. Zinke, J. Kropp, F. Arndt, and K. Petermann, "0.1 db/cm waveguide losses in single-mode soi rib waveguides," *Photonics Technology Letters, IEEE*, vol. 8, no. 5, pp. 647–648, 1996.

[5] J. Cardenas, C. B. Poitras, J. T. Robinson, K. Preston, L. Chen, and M. Lipson, "Low loss etchless silicon photonic waveguides," *Optics express*, vol. 17, no. 6, pp. 4752–4757, 2009.

[6] V. R. Almeida, R. R. Panepucci, and M. Lipson, "Nanotaper for compact mode conversion," *Optics Letters*, vol. 28, no. 15, pp. 1302–1304, 2003.

[7] W. M. Green, M. J. Rooks, L. Sekaric, and Y. A. Vlasov, "Ultra-compact, low rf power, 10 gb/s silicon mach-zehnder modulator," *Optics express*, vol. 15, no. 25, pp. 17106–17113, 2007.

[8] A. Liu, R. Jones, L. Liao, D. Samara-Rubio, D. Rubin, O. Cohen, R. Nicolaescu, and M. Paniccia, "A high-speed silicon optical modulator based on a metal–oxide–semiconductor capacitor," *Nature*, vol. 427, no. 6975, pp. 615–618, 2004.

[9] Q. Xu, B. Schmidt, S. Pradhan, and M. Lipson, "Micrometre-scale silicon electro-optic modulator," *Nature*, vol. 435, no. 7040, pp. 325–327, 2005.

[10] J. Michel, J. Liu, and L. C. Kimerling, "High-performance ge-on-si photodetectors," *Nature Photonics*, vol. 4, no. 8, pp. 527–534, 2010.

[11] S. Assefa, F. Xia, and Y. A. Vlasov, "Reinventing germanium avalanche

photodetector for nanophotonic on-chip optical interconnects," *Nature*, vol. 464, no. 7285, pp. 80–84, 2010.

[12] L. Chen and M. Lipson, "Ultra-low capacitance and high speed germanium photodetectors on silicon," *Optics Express*, vol. 17, no. 10, pp. 7901–7906, 2009.

[13] A. W. Fang, H. Park, O. Cohen, R. Jones, M. J. Paniccia, and J. E. Bowers, "Electrically pumped hybrid algainas-silicon evanescent laser," *Optics Express*, vol. 14, no. 20, pp. 9203–9210, 2006.

[14] A. Alduino, L. Liao, R. Jones, M. Morse, B. Kim, W.-Z. Lo, J. Basak, B. Koch, H.-F. Liu, H. Rong, *et al.*, "Demonstration of a high speed 4-channel integrated silicon photonics wdm link with hybrid silicon lasers," in *Integrated Photonics Research, Silicon and Nanophotonics*, p. PDIWI5, Optical Society of America, 2010.

[15] X. Zheng, F. Liu, J. Lexau, D. Patil, G. Li, Y. Luo, H. Thacker, I. Shubin, J. Yao, K. Raj, *et al.*, "Ultra-low power arrayed cmos silicon photonic transceivers for an 80 gbps wdm optical link," in *Optical Fiber Communication Conference*, p. PDPA1, Optical Society of America, 2011.

[16] L. Chen, K. Preston, S. Manipatruni, and M. Lipson, "Integrated ghz silicon photonic interconnect with micrometer-scale modulators and detectors," *Optics express*, vol. 17, no. 17, pp. 15248–15256, 2009.

[17] F. J. Mesa-Martinez, M. Brown, J. Nayfach-Battilana, and J. Renau, "Measuring power and temperature from real processors," in *Parallel and Distributed Processing, 2008. IPDPS 2008. IEEE International Symposium on*, pp. 1–5, IEEE, 2008.

[18] P. Alipour, E. S. Hosseini, A. A. Eftekhar, B. Momeni, and A. Adibi, "Temperature-insensitive silicon microdisk resonators using polymeric cladding layers," *in Conference on Lasers and Electro-Optics, (Optical Society of America)*, 2009.

[19] J. Teng, P. Dumon, W. Bogaerts, H. B. Zhang, X. G. Jian, X. Y. Han, M. S. Zhao, G. Morthier, and R. Baets, "Athermal silicon-on-insulator ring resonators by overlaying a polymer cladding on narrowed waveguides," *Optics Express*, vol. 17, pp. 14627–14633, 2009.

[20] M. Han and A. Wang, "Temperature compensation of optical microres-

onators using a surface layer with negative thermo-optic coefficient," *Optics Letters*, vol. 32, pp. 1800–1802, 2007.

[21] J.-M. Lee, D.-J. Kim, H. Ahn, S.-H. Park, and G. Kim, "Temperature dependence of silicon nanophotonic ring resonator with a polymeric overlayer," *Journal of lightwave technology*, vol. 25, no. 8, pp. 2236–2243, 2007.

[22] K. Padmaraju, J. Chan, L. Chen, M. Lipson, and K. Bergman, "Thermal stabilization of a microring modulator using feedback control," *Optics Express*, vol. 20, pp. 27999–28008, 2012.

[23] K. Padmaraju, D. F. Logan, X. Zhu, J. J. Ackert, A. P. Knights, and K. Bergman, "Integrated thermal stabilization of a microring modulator," *in Optical Fiber Communication Conference, (Optical Society of America)*, 2013.

[24] E. Timurdogan, A. Biberman, D. C. Trotter, C. Sun, M. Moresco, V. Stojanovic, and M. R. Watts, "Automated wavelength recovery for microring resonators," *in CLEO Science and Innovations, (Optical Society of America)*, 2012.

[25] C. T. DeRose, M. R. Watts, D. C. Trotter, D. L. Luck, G. N. Nielson, and R. W. Young, "Silicon microring modulator with integrated heater and temperature sensor for thermal control," *in Conference on Lasers and Electro-Optics, (Optical Society of America)*, 2010.

[26] P. Dong, W. Qian, H. Liang, R. Shafiiha, N.-N. Feng, D. Feng, X. Zheng, A. V. Krishnamoorthy, and M. Asghari, "Low power and compact reconfigurable multiplexing devices based on silicon microring resonators," *Optics Express*, vol. 18, pp. 9852–9858, 2010.

[27] M. R. Watts, W. A. Zortman, D. C. Trotter, G. N. Nielson, D. L. Luck, and R. W. Young, "Adiabatic resonant microrings (arms) with directly integrated thermal microphotonics," in *Conference on Lasers and Electro-Optics*, p. CPDB10, Optical Society of America, 2009.

[28] M. R. Watts, D. C. Trotter, R. W. Young, and A. L. Lentine, "Ultralow power silicon microdisk modulators and switches," in *Group IV Photonics, 2008 5th IEEE International Conference on*, pp. 4–6, IEEE, 2008.

[29] S. Manipatruni, R. K. Dokania, B. Schmidt, N. Sherwood-Droz, C. B. Poitras, A. B. Apsel, and M. Lipson, "Wide temperature range operation of micrometer-scale silicon electro-optic modulators," *Optics letters*, vol. 33, no. 19, pp. 2185–2187, 2008.

[30] N. Sherwood-Droz, H. Wang, L. Chen, B. G. Lee, A. Biberman, K. Bergman, and M. Lipson, "Optical 4x4 hitless slicon router for optical networks-on-chip (noc)," *Optics express*, vol. 16, no. 20, pp. 15915–15922, 2008.

[31] P. Dong, W. Qian, H. Liang, R. Shafiiha, D. Feng, G. Li, J. E. Cunningham, A. V. Krishnamoorthy, and M. Asghari, "Thermally tunable silicon racetrack resonators with ultralow tuning power," *Optics express*, vol. 18, no. 19, pp. 20298–20304, 2010.

[32] R. A. Soref and B. R. Bennett, "Electrooptical effects in silicon," *Quantum Electronics, IEEE Journal of*, vol. 23, no. 1, pp. 123–129, 1987.

[33] G. T. Reed, G. Mashanovich, F. Gardes, and D. Thomson, "Silicon optical modulators," *Nature photonics*, vol. 4, no. 8, pp. 518–526, 2010.

[34] D. A. Miller, "Device requirements for optical interconnects to silicon chips," *Proceedings of the IEEE*, vol. 97, no. 7, pp. 1166–1185, 2009.

[35] R. K. Dokania and A. B. Apsel, "Analysis of challenges for on-chip optical interconnects," in *Proceedings of the 19th ACM Great Lakes symposium on VLSI*, pp. 275–280, ACM, 2009.

[36] S. Manipatruni, M. Lipson, and I. A. Young, "Device scaling considerations for nanophotonic cmos global interconnects," *IEEE Journal of Selected Topics in Quantum Electronics*, vol. 19, no. 2, pp. 400–408, 2013.

[37] M. Uenuma and T. Motooka, "Temperature-independent silicon waveguide optical filter," *Optics letters*, vol. 34, no. 5, pp. 599–601, 2009.

[38] Y. Varshni, "Temperature dependence of the energy gap in semiconductors," *Physica*, vol. 34, pp. 149–154, 1967.

[39] P. Absil, J. Hryniewicz, B. Little, R. Wilson, L. Joneckis, and P.-T. Ho, "Compact microring notch filters," *Photonics Technology Letters, IEEE*, vol. 12, no. 4, pp. 398–400, 2000.

[40] M. Terrel, M. J. Digonnet, and S. Fan, "Ring-coupled mach-zehnder interferometer optimized for sensing," *Applied optics*, vol. 48, no. 26, pp. 4874–4879, 2009.

[41] B. Guha, A. Gondarenko, and M. Lipson, "Minimizing temperature sensitivity of silicon mach-zehnder interferometers," *Optics Express*, vol. 18, pp. 1879–1887, 2010.

[42] B. G. Lee, B. A. Small, K. Bergman, Q. Xu, and M. Lipson, "Transmission of high-data-rate optical signals through a micrometer-scale silicon ring resonator," *Optics letters*, vol. 31, no. 18, pp. 2701–2703, 2006.

[43] I. Shake, H. Takara, and S. Kawanishi, "Simple measurement of eye diagram and ber using high-speed asynchronous sampling," *Journal of lightwave technology*, vol. 22, no. 5, p. 1296, 2004.

[44] G. P. Agrawal, *Fiber-optic communication systems*, vol. 1. 1997.

[45] B. Guha, B. B. C. Kyotoku, and M. Lipson, "Cmos-compatible athermal silicon microring resonators," *Optics Express*, vol. 18, pp. 3487–3493, 2010.

[46] S. A. Campbell, H.-S. Kim, D. C. Gilmer, B. He, T. Ma, and W. L. Gladfelter, "Titanium dioxide (tio_2)-based gate insulators," *IBM journal of research and development*, vol. 43, pp. 383–392, 1999.

[47] V. Trepakov, A. Dejneka, P. Markovin, A. Lynnyk, and L. Jastrabik, "A 'soft electronic band' and the negative thermooptic effect in strontium titanate," *New Journal of Physics*, vol. 11, p. 083024, 2009.

[48] B. Guha and M. Lipson, "Athermal silicon ring resonator with bi-material cantilever for passive thermal feedback," *in CLEO Science and Innovations, (Optical Society of America)*, 2013.

[49] S. S. Djordjevic, K. Shang, B. Guan, S. T. Cheung, L. Liao, J. Basak, H.-F. Liu, and S. Yoo, "Cmos-compatible, athermal silicon ring modulators clad with titanium dioxide," *Optics Express*, vol. 21, pp. 13958–13968, 2013.

[50] F. Qiu, A. M. Spring, F. Yu, and S. Yokoyama, "Complementary metaloxidesemiconductor compatible athermal silicon nitride/ titanium dioxide hybrid micro-ring resonators," *Applied Physics Letters*, vol. 102, p. 051106, 2013.

[51] J. T. Choy, J. D. Bradley, P. B. Deotare, I. B. Burgess, C. C. Evans, E. Mazur, and M. Loncar, "Integrated tio_2 resonators for visible photonics," *Optics Letters*, vol. 37, pp. 539–541, 2012.

[52] J. D. Bradley, C. C. Evans, J. T. Choy, O. Reshef, P. B. Deotare, F. Parsy, K. C. Phillips, M. Loncar, and E. Mazur, "Submicrometer-wide amorphous and polycrystalline anatase tio$_2$ waveguides for microphotonic devices," *Optics Express*, vol. 20, pp. 23821–23831, 2012.

[53] E. D. Palik, *Handbook of optical constants of solids*, vol. 3. Academic press, 1998.

[54] C. Qiu and Q. Xu, "Wavelength tracking with thermally controlled silicon resonators," *in CLEO Science and Innovations, (Optical Society of America)*, 2011.

[55] B. Guha, K. Preston, and M. Lipson, "Athermal silicon microring electro-optic modulator," *Optics Letters*, vol. 37, pp. 2253–2255, 2012.

[56] B. Guha, J. Cardenas, and M. Lipson, "Athermal silicon microring resonators with titanium oxide cladding," *Optics express*, vol. 21, no. 22, pp. 26557–26563, 2013.

[57] J. Bovington, R. Wu, K.-T. Cheng, and J. E. Bowers, "Thermal stress implications in athermal tio¡ sub¿ 2¡/sub¿ waveguides on a silicon substrate," *Optics Express*, vol. 22, no. 1, pp. 661–666, 2014.

[58] S. Abdulla, L. Kauppinen, M. Dijkstra, M. De Boer, E. Berenschot, H. Jansen, R. De Ridder, and G. Krijnen, "Tuning a racetrack ring resonator by an integrated dielectric mems cantilever," *Optics express*, vol. 19, no. 17, pp. 15864–15878, 2011.

[59] E. Gavartin, P. Verlot, and T. Kippenberg, "A hybrid on-chip optomechanical transducer for ultrasensitive force measurements," *Nature nanotechnology*, vol. 7, no. 8, pp. 509–514, 2012.

[60] K. Srinivasan, H. Miao, M. T. Rakher, M. Davanco, and V. Aksyuk, "Optomechanical transduction of an integrated silicon cantilever probe using a microdisk resonator," *Nano letters*, vol. 11, no. 2, pp. 791–797, 2011.

[61] S. Sridaran and S. A. Bhave, "Electrostatic actuation of silicon optomechanical resonators," *Optics express*, vol. 19, no. 10, pp. 9020–9026, 2011.

[62] S. Tallur and S. A. Bhave, "A silicon electromechanical photodetector," *Nano letters*, vol. 13, no. 6, pp. 2760–2765, 2013.

[63] M. Li, W. H. Pernice, and H. X. Tang, "Reactive cavity optical force on microdisk-coupled nanomechanical beam waveguides," *Physical review letters*, vol. 103, no. 22, p. 223901, 2009.

[64] C. Jha, G. Bahl, R. Melamud, S. Chandorkar, M. Hopcroft, B. Kim, M. Agarwal, J. Salvia, H. Mehta, and T. Kenny, "High resolution microresonator-based digital temperature sensor," *Applied physics letters*, vol. 91, no. 7, p. 074101, 2007.

[65] B.-B. Li, Q.-Y. Wang, Y.-F. Xiao, X.-F. Jiang, Y. Li, L. Xiao, and Q. Gong, "On chip, high-sensitivity thermal sensor based on high-q polydimethylsiloxane-coated microresonator," *Applied Physics Letters*, vol. 96, no. 25, p. 251109, 2010.

[66] M. R. Watts, M. J. Shaw, and G. N. Nielson, "Optical resonators: Microphotonic thermal imaging," *Nature Photonics*, vol. 1, no. 11, pp. 632–634, 2007.

[67] M. R. Watts, M. J. Shaw, G. N. Nielson, J. B. Wright, K. Westlake, I. Brener, J. L. Rienstra, and F. B. McCormick, "Thermal microphotonic focal plane array (tm-fpa) for uncooled high sensitivity thermal imaging," in *Conference on Lasers and Electro-Optics*, p. CTuZ5, Optical Society of America, 2007.

[68] J. Pendry, "Radiative exchange of heat between nanostructures," *J. Phys.: Condens. Matter*, vol. 11, p. 6621, 1999.

[69] D. Polder and M. Vanhove, "Theory of radiative heat transfer between closely spaced bodies," *Physical Review B: Condensed Matter and Materials Physics*, vol. 4, pp. 3303–3314, 1971.

[70] A. Volokitin and B. Persson, "Near-field radiative heat transfer and noncontact friction," *Rev. Mod. Phys.*, vol. 79, pp. 1291–1329, 2007.

[71] M. Maldovan, "Narrow low-frequency spectrum and heat management by thermocrystals," *Physical review letters*, vol. 110, no. 2, p. 025902, 2013.

[72] K. Joulain, J.-P. Mulet, F. Marquier, R. Carminati, and J.-J. Greffet, "Surface electromagnetic waves thermally excited: Radiative heat transfer, coherence properties and casimir forces revisited in the near field," *Surface Science Reports*, vol. 57, no. 3, pp. 59–112, 2005.

[73] S. Basu, Z. Zhang, and C. Fu, "Review of near-field thermal radiation and its application to energy conversion," *International Journal of Energy Research*, vol. 33, pp. 1203–1232, 2009.

[74] A. V. Shchegrov, K. Joulain, R. Carminati, and J.-J. Greffet, "Near-field spectral effects due to electromagnetic surface excitations," *Physical review letters*, vol. 85, no. 7, pp. 1548–1551, 2000.

[75] J. P. Mulet, K. Joulain, R. Carminati, and J. J. Greffet, "Nanoscale radiative heat transfer between a small particle and a plane surface," *Applied Physics Letters*, vol. 78, p. 2931, 2001.

[76] C. J. Fu and Z. M. Zhang, "Nanoscale radiation heat transfer for silicon at different doping levels," *Int. J. Heat Mass Tran.*, vol. 49, pp. 1703–1718, 2006.

[77] E. Rousseau, M. Laroche, and J. J. Greffet, "Radiative heat transfer at nanoscale mediated by surface plasmons for highly doped silicon," *Applied Physics Letters*, vol. 95, p. 231913, 2009.

[78] P. Ben-Abdallah, K. Joulain, and A. Pryamikov, "Surface bloch waves mediated heat transfer between two photonic crystals," *Applied Physics Letters*, vol. 96, p. 143117, 2010.

[79] A. Narayanaswamy, S. Shen, and G. Chen, "Near-field radiative heat transfer between a sphere and a substrate," *Physical Review B: Condensed Matter and Materials Physics*, vol. 78, p. 115303, 2008.

[80] E. Rousseau, A. Siria, G. Jourdan, S. Volz, F. Comin, J. Chevrier, and J. J. Greffet, "Radiative heat transfer at the nanoscale," *Nature Photonics*, vol. 3, pp. 514–517, 2009.

[81] S. Shen, A. Narayanaswamy, and G. Chen, "Surface phonon polaritons mediated energy transfer between nanoscale gaps," *Nano Letters*, vol. 9, pp. 2909–2913, 2009.

[82] R. S. Ottens, V. Quetschke, S. Wise, A. A. Alemi, R. Lundock, G. Mueller, D. H. Reitze, D. B. Tanner, and B. F. Whiting, "Near-field radiative heat transfer between macroscopic planar surfaces," *Physical Review Letters*, vol. 107, p. 014301, 2011.

[83] A. Kittel, W. M. Hirsch, J. Parisi, S. Biehs, D. Reddig, and M. Holthaus,

"Near-field heat transfer in a scanning thermal microscope," *Physical Review Letters*, vol. 95, p. 224301, 2005.

[84] C. Otey and S. Fan, "Numerically exact calculation of electromagnetic heat transfer between a dielectric sphere and plate," *Physical Review B: Condensed Matter and Materials Physics*, vol. 84, p. 245431, 2011.

[85] P. Kim, L. Shi, A. Majumdar, and P. L. McEuen, "Thermal transport measurements of individual multiwalled nanotubes," *Physical Review Letters*, vol. 87, p. 215502, 2001.

[86] K. Schwab, E. A. Henriksen, J. M. Worlock, and M. L. Roukes, "Measurement of the quantum of thermal conductance," *Nature*, vol. 404, pp. 974–977, 2000.

[87] T. S. Tighe, J. M. Worlock, and M. L. Roukes, "Direct thermal conductance measurements on suspended monocrystalline nanostructures," *Applied Physics Letters*, vol. 70, p. 2687, 1997.

[88] A. Narayanaswamy and G. Chen, "Thermal near-field radiative transfer between two spheres," *Physical Review B*, vol. 77, no. 7, p. 075125, 2008.

[89] C. Otey, W. T. Lau, and S. Fan, "Thermal rectification through vacuum," *Physical Review Letters*, vol. 104, p. 154301, 2010.

[90] S. Basu and M. Francoeur, "Near-field radiative transfer based thermal rectification using doped silicon," *Applied Physics Letters*, vol. 98, p. 113106, 2011.

[91] L. Wang and Z. Zhang, "Thermal rectification enabled by near-field radiative heat transfer between intrinsic silicon and a dissimilar material," *Nanoscale and Microscale Thermophysical Engineering*, vol. 17, no. 4, pp. 337–348, 2013.

[92] L. Zhu, C. Otey, and S. Fan, "Negative differential thermal conductance through vacuum," *Applied Physics Letters*, vol. 98, p. 113106, 2012.

[93] M. Terraneo, M. Peyrard, and G. Casati, "Controlling the energy flow in nonlinear lattices: a model for a thermal rectifier," *Physical review letters*, vol. 88, no. 9, p. 094302, 2002.

[94] D. Segal, "Single mode heat rectifier: Controlling energy flow between

electronic conductors," *Physical review letters*, vol. 100, no. 10, p. 105901, 2008.

[95] J. Hu, X. Ruan, and Y. P. Chen, "Thermal conductivity and thermal rectification in graphene nanoribbons: a molecular dynamics study," *Nano Letters*, vol. 9, no. 7, pp. 2730–2735, 2009.

[96] C. Chang, D. Okawa, A. Majumdar, and A. Zettl, "Solid-state thermal rectifier," *Science*, vol. 314, no. 5802, pp. 1121–1124, 2006.

[97] H. Tian, D. Xie, Y. Yang, T.-L. Ren, G. Zhang, Y.-F. Wang, C.-J. Zhou, P.-G. Peng, L.-G. Wang, and L.-T. Liu, "A novel solid-state thermal rectifier based on reduced graphene oxide," *Scientific reports*, vol. 2, 2012.

[98] H. Iizuka and S. Fan, "Rectification of evanescent heat transfer between dielectric-coated and uncoated silicon carbide plates," *Journal of Applied Physics*, vol. 112, no. 2, p. 024304, 2012.

[99] L. Wang, S. Basu, and Z. Zhang, "Direct measurement of thermal emission from a fabry–perot cavity resonator," *Journal of Heat Transfer*, vol. 134, no. 7, p. 072701, 2012.

[100] A. Sievers, "Thermal radiation from metal surfaces," *JOSA*, vol. 68, no. 11, pp. 1505–1516, 1978.

[101] `http://www.zyvex.com/Products/S100_Features.html`.

[102] L. Zhu, C. R. Otey, and S. Fan, "Ultrahigh-contrast and large-bandwidth thermal rectification in near-field electromagnetic thermal transfer between nanoparticles," *Physical Review B*, vol. 88, no. 18, p. 184301, 2013.

[103] J. C. Mikkelsen, W. D. Sacher, and J. K. Poon, "Adiabatically widened silicon microrings for improved variation tolerance," *Optics Express*, vol. 22, no. 8, pp. 9659–9666, 2014.

[104] S. K. Selvaraja, W. Bogaerts, P. Dumon, D. Van Thourhout, and R. Baets, "Subnanometer linewidth uniformity in silicon nanophotonic waveguide devices using cmos fabrication technology," *Selected Topics in Quantum Electronics, IEEE Journal of*, vol. 16, no. 1, pp. 316–324, 2010.

[105] T. Baehr-Jones, T. Pinguet, P. L. Guo-Qiang, S. Danziger, D. Prather, and

M. Hochberg, "Myths and rumours of silicon photonics," *Nature Photonics*, vol. 6, no. 4, pp. 206–208, 2012.

[106] A. Lenert, D. M. Bierman, Y. Nam, W. R. Chan, I. Celanović, M. Soljačić, and E. N. Wang, "A nanophotonic solar thermophotovoltaic device," *Nature nanotechnology*, 2014.

[107] A. Narayanaswamy and G. Chen, "Surface modes for near field thermophotovoltaics," *Applied Physics Letters*, vol. 82, no. 20, pp. 3544–3546, 2003.

[108] S.-A. Biehs, E. Rousseau, J.-J. Greffet, *et al.*, "Mesoscopic description of radiative heat transfer at the nanoscale," *Phys. Rev. Lett*, vol. 105, no. 23, p. 234301, 2010.

[109] P. van Zwol, L. Ranno, and J. Chevrier, "Tuning near field radiative heat flux through surface excitations with a metal insulator transition," *Physical review letters*, vol. 108, no. 23, p. 234301, 2012.

[110] P. Ben-Abdallah and S.-A. Biehs, "Near-field thermal transistor," *Physical Review Letters*, vol. 112, no. 4, p. 044301, 2014.

[111] M. Meschke, W. Guichard, and J. P. Pekola, "Single-mode heat conduction by photons," *Nature*, vol. 444, no. 7116, pp. 187–190, 2006.

[112] N. F. Mott and L. Friedman, "Metal-insulator transitions in vo2, ti2o3 and ti2-x v x o3," *Philosophical Magazine*, vol. 30, no. 2, pp. 389–402, 1974.

[113] M. A. Kats, R. Blanchard, S. Zhang, P. Genevet, C. Ko, S. Ramanathan, and F. Capasso, "Vanadium dioxide as a natural disordered metamaterial: perfect thermal emission and large broadband negative differential thermal emittance," *Physical Review X*, vol. 3, no. 4, p. 041004, 2013.

[114] O. Ilic, M. Jablan, J. D. Joannopoulos, I. Celanovic, H. Buljan, and M. Soljačić, "Near-field thermal radiation transfer controlled by plasmons in graphene," *Physical Review B*, vol. 85, no. 15, p. 155422, 2012.

[115] Y. Guo, C. L. Cortes, S. Molesky, and Z. Jacob, "Broadband superplanckian thermal emission from hyperbolic metamaterials," *Applied Physics Letters*, vol. 101, no. 13, p. 131106, 2012.

[116] Y. Guo and Z. Jacob, "Thermal hyperbolic metamaterials," *Optics express*, vol. 21, no. 12, pp. 15014–15019, 2013.